

Battery State of Health Monitoring via Estimation of Health-Relevant Electrochemical Variables

by

Xin Zhou

A dissertation submitted in partial fulfillment
of the requirements for the degree of
Doctor of Philosophy
(Mechanical Engineering)
in the University of Michigan
2017

Doctoral Committee:

Professor Jeffrey L. Stein, Co-chair
Dr. Tulga Ersal, Co-chair
Professor Dennis S. Bernstein
Professor Anna G. Stefanopoulou

The right to search for truth implies also a duty; one must not conceal any part of what one has recognized to be true.

— Albert Einstein

If people do not believe that mathematics is simple, it is only because they do not realize how complicated life is.

— John von Neumann

夫夷以近，則遊者衆；險以遠，則至者少。而世之奇偉、瑰怪、非常之觀，常在於險遠，而人之所罕至焉，故非有志者不能至也。有志矣，不隨以止也，然力不足者，亦不能至也。有志與力，而又不隨以怠，至於幽暗昏惑，而無物以相之，亦不能至也。

— 王安石 《遊褒禪山記》

寄蜉蝣於天地，渺滄海之一粟。哀吾生之須臾，羨長江之無窮。挾飛仙以遨游，抱明月而長終。知不可乎驟得，托遺響于悲風。……客亦知夫水與月乎？逝者如斯，而未嘗往也。盈虛者如彼，而卒莫消長也。蓋將自其變者而觀之，而天地曾不能以一瞬；自其不變者而觀之，則物與我皆無盡也，而又何羨乎？且夫天地之間，物各有主，苟非吾之所有，雖一毫而莫取。惟江上之清風，與山間之明月，耳得之而為聲，目遇之而成色，取之無禁，用之不竭，是造物者之無盡藏也，而吾與子之所共適。

— 蘇軾 《赤壁賦》



Xin Zhou

zhouxin@umich.edu

ORCID iD: 0000-0002-1568-1510

©Xin Zhou 2017

To life, love, and light.

Acknowledgments

With this dissertation finished, I am concluding a five-year pursuit for not only a PhD degree, but, more importantly, a better self. I am sincerely grateful for all the people who have supported me in this pursuit and all the events that have shaped me into who I am today. All the sweet and bitter experiences in these five years have equipped me with skills, strength, and courage for any future quest that lies ahead in life.

First of all, I would like to thank my advisors, Professor Jeffrey Stein and Dr. Tulga Ersal, for their invaluable mentorship, guidance, and support. Professor Stein has always been a great resource to turn to whenever I am stuck in research or confused in life. His willingness to listen, understand, advise, and step in to support whenever needed has never failed me. Conversing with him has always felt like reading a book that is full of wisdom to me and encouraged me to rethink and reflect on my own thinking and behavior. I cannot thank Tulga enough for being both an indispensable mentor and a very dear friend. As a mentor, he has been closely following my research progress and my development as a student, and has taught me a great deal of technical and interpersonal skills using every possible opportunity. I am greatly thankful for his tremendous patience with my clumsiness, tolerance with my impetuousness, and never failing belief in me even during the moments when I am annoyed by my own incapability. As a friend, interactions with him are so magically comfortable and soothing due to his kind, caring, and sensitive personality. He has also been the first person that I turn to for help in all my big and little “crises” because he is such a person who would offer you support as much as he can give. Even during the time when he doesn’t know how to help you immediately, he would go to learn the required

knowledge and skills, and come back to help you.

I also want to extend my gratitude to the other members of my dissertation committee, Professor Dennis Bernstein and Professor Anna Stefanopoulou. Professor Bernstein has been involved with my doctoral work since day one, during which time he has offered a lot of guidance in both control theories and technical writing skills. The code for the retrospective-cost subsystem identification algorithm is also revised from the work done in his group. As an expert in battery modeling and management, Professor Anna Stefanopoulou has shared with me much advice and deep insight to help me improve my work. I would also like to thank US-China Clean Energy Research Center - Clean Vehicles Consortium (grant number DE-PI0000012) for providing the funding for this research.

There are many other faculty members either in the general community of battery management or at the University of Michigan whom I am grateful for. I would like to thank Professor Scott Moura at UC Berkley for his always helpful advice and resources. The code for the DFN model used in this dissertation is also revised from a code that he made publicly available for the battery management community [1]. I would also like to thank Professor Hosam Fathy at Penn State for being a strong advocate for me in the community. Professor Giorgio Rizzoni at the OSU has also given me great encouragement every time we meet in the conferences. At UM, Professor Jing Sun and Professor Demosthenis Teneketzis have generously shared their wisdom and advice in career development with me, for which I am very thankful.

I would like to thank all the members of Automated Modeling Lab, Jiechao, Xinyi, Huck, Yingshi, Alireza, Hossein, and John, for their friendship and helpful technical discussions. They have made contributions to this dissertation by giving me difficult questions and helpful comments in our group meetings. All these questions and comments have helped me think more and deeper about both my technical work and how to communicate more effectively. They are an essential part in my development as a researcher and a technical presenter.

Looking back to five years ago, I am grateful that I chose to become a control engineer, even though I didn't fully understand what being a control engineer entails

at that time. The time spent working on this dissertation as well as other control problems as a student or as a Graduate Student Instructor has been the most humbling. As a control engineer, everyday I am experiencing the contrast between the elegance of linear theories and the messiness of nonlinearity, the divergence between the simplicity of models and the complexity of true systems, and the deviation from the exciting theories to frustrating reality. Take the estimation problem of the side reaction current density presented in Chapter 3 and 4 of this dissertation for example: the estimates can be infinitely accurate in simulations under ideal conditions, but a small “imperfection” in the measurements or models can lead to huge estimation errors in real life. It is with this experience that I understood that knowledge is not an ultimate truth of the universe but simply “a mental grid that human beings have created and imposed over a more complex reality to try to understand and manipulate it” [2]. This understanding humbled me as a human being; I have realized the limits of human knowledge and learnt to be more respectful to the nature and life. Moreover, this understanding humbled me in front of all my human fellows. Even with all the limits posed on our understanding of the universe, the humanity has build such a beautiful and diverse civilization and is still striving to achieve more. I admire and am strongly inspired by all the people who have made this world possible, and all the people who had come to understand our limits but still kept going to search for new and better knowledge. This humbleness will become a source of strength for me in all my future journeys. The technical contents of this dissertation reflect only part of the knowledge that I have gained and generated in my doctoral work, but the changes that this experience has made to me as an individual is more profound than these intellectual gains. All the life lessons that I have learnt and all the new layers of my personality that have grown in me during these five years will probably follow me for much longer time than the equations that I laid out herein, and are what I am most thankful for.

My friends deserve special thanks. Over the years, I have been blessed with a group of amazing friends who have been with me for as long as more than two decades. I would like to thank all of them, Beibei, Peipei, Yifei, Xiaoting, Xiaoyun, Tiancheng,

and Shuo, for being with me through thick and thin. Their support during the most difficult time, their understanding even in the most controversial situation, and their unconditional love for me are one of my best treasures in life. I would also like to thank all the friends that I met in Michigan for keeping my life interesting during the stressful years in graduate school.

I would also like to thank my cousin, Haoran, for being a great bigger brother in my life. He is always there for me when I need someone to talk to. His advice for my life and career has always been very helpful and resonatory. His willingness to listen and his open mindedness make me feel understood, safe, and loved.

Finally and most importantly, I want to thank my parents for being the most visionary parents that I know. Through the whirlpool of life, they were able to help me look far beyond the pettiness in life to see a bigger world with much more beauty. They sent me to school but did not make grades their priority in education. They gave me books but also taught me to question what I read. They took me to travel but also told me that personal value is achieved only by focusing on work at hand. During my whole life, they have been both my strongest believers and my strictest critics. Whereas the goal of all the other kinds of love in the world is to bring people together, the goal of the parental love is to make the kids independent from the family. My parents are the best embodiment of this parental love. When they sent off their “pearl in the palm” to fly across half of the world to realize her own ambition, they didn’t tell her to come back early but told her to fly as high as she can. Every word in this dissertation is only possible with their wisdom and vision, which I greatly appreciate and admire.

Life is a lonely quest in the darkness; it is the people who accept, appreciate, and love you for who you are that light your way. I thank these people in my life. May I never lose my light.

Table of Contents

Dedication	ii
Acknowledgments	iii
List of Tables	xii
List of Figures	xviii
List of Appendices	xix
Nomenclature of Electrochemical Variables	xx
Abstract	xxiii
Chapter 1 Introduction	1
1.1 Background and Literature Review	1
1.1.1 Battery State of Health Monitoring	1
1.1.2 Battery Chemistries	2
1.1.3 Battery Degradation Effects and Mechanisms	3
1.1.4 SOH Indicators	4
1.2 Research Objective	5
1.3 Methodology	6
1.3.1 Selection of SOH Indicators	6
1.3.2 Estimation	7
1.4 Research Questions	8

1.5	Dissertation Organization	8
Chapter 2	Battery Models	10
2.1	Introduction	10
2.2	Battery SOC Models	11
2.2.1	Doyle-Fuller-Newman (DFN) Model	11
2.2.1.1	The Electrochemical Form	11
2.2.1.2	The Estimation Form	15
2.2.2	Single Particle Model (SPM)	17
2.2.2.1	The Electrochemical Form	18
2.2.2.2	The Estimation Form	19
2.3	Battery SOH Model	21
2.3.1	The Electrochemical Form	21
2.3.2	The Estimation Form	22
2.4	Combining SOC Model and SOH Model	26
2.5	Summary and Conclusions	26
Chapter 3	Estimation of Side Reaction Current Density	28
3.1	Introduction	28
3.2	Retrospective-Cost Subsystem Identification	30
3.2.1	Problem Setup	30
3.2.2	Algorithm Development	32
3.2.2.1	Retrospective-Cost-Based Signal Construction . . .	33
3.2.2.2	Kalman Filter Update of the Subsystem Parameter .	37
3.3	Simulation Results under Ideal Conditions	38
3.3.1	Constant Current Charge and Discharge Cycles	40
3.3.2	The Urban Dynamometer Driving Schedule Test Cycles . .	41
3.4	Robustness to Non-Ideal Conditions	42
3.4.1	The Relationship between the Estimation Accuracy and Voltage Errors	43
3.4.2	Robustness to Measurement Noise	45

3.4.3	Robustness to SOC Estimation Errors	47
3.4.4	Robustness to Modeling Error	49
3.4.4.1	Modeling Error in Main System Model	49
3.4.4.2	Form Discrepancy between Subsystem and Subsystem Model	53
3.4.5	Discussions and Extensions of the Simulation Results	56
3.5	A Framework to Obtain Lower Bound of Relative Estimation Errors for Voltage-Error-Based Algorithms	58
3.6	Simulation Results with LMO-Mixture Battery Parameters	61
3.7	Summary and Conclusions	65
Chapter 4 Two-Step Filter		68
4.1	Introduction	68
4.2	The Development of the Two-Step Filter	70
4.2.1	Problem Setup	70
4.2.2	The System	71
4.2.3	Estimation Setup	72
4.2.4	The Two-Step Filter	73
4.2.4.1	The First Step	74
4.2.4.2	The Second Step	75
4.2.5	Estimation of the Subsystem Output	77
4.3	Application to Estimation of Side Reaction Current Density	78
4.3.1	Modified Battery Model	78
4.3.2	Application on Time Varying Linearized Battery Model	80
4.3.3	Application on Nonlinear Battery Model	83
4.3.4	Evaluating the Sensitivity of the Voltage to the States	88
4.3.5	Discussion	91
4.4	Summary and Conclusions	93
Chapter 5 Estimation of the Number of Cyclable Li-ions		96
5.1	Introduction	96

5.2	Problem Setup	98
5.2.1	True System	99
5.2.2	System Model	100
5.2.3	Estimation Technique	100
5.2.4	Estimation Process	101
5.3	The Extended Kalman Filter	101
5.4	The Preparation Stage: Parameterization	103
5.4.1	Parameterization using Genetic Algorithm	103
5.4.2	Discussions about Parameterization	105
5.5	The Estimation Stage: Estimation under Ideal Conditions	111
5.6	The Estimation Stage: Robustness to Non-Ideal Conditions	113
5.6.1	Robustness to SOC Estimation Error	114
5.6.2	Robustness to Additional Modeling Error	115
5.6.3	Robustness to Measurement Noise	117
5.6.4	Combination of Non-Ideal Conditions	118
5.7	Lower Bounds on Relative Estimation Error and Covariance of Estimates	120
5.8	Summary and Conclusions	122
Chapter 6	Comparison of the Effectiveness of Estimating Side Reaction Current Density and the Number of Cyclable Li-ions as SOH Indicators	125
6.1	Comparison between Side Reaction Current Density and the Number of Cyclable Li-ions as SOH Indicators	126
6.2	Comparison to Effects-Based SOH Indicators	128
Chapter 7	Conclusions and Future Work	130
7.1	Dissertation Summary	130
7.2	Conclusions and Contributions	133
7.3	List of Publications	137
7.4	Future Extensions	138
7.4.1	Inclusion of Thermal Impact	138

7.4.2	Estimation of Current Densities in Other Battery Degradation and Safety Problems	139
7.4.3	Experimental Validation	139
7.4.3.1	Electrochemical Parts	140
7.4.3.2	Cycling Part	141
7.4.3.3	Validation	142
	Appendices	143
	Bibliography	161

List of Tables

5.1	The identified parameter sets from the genetic algorithm. The parameter set in the column labelled Original is from [3]. The parameter sets in the columns labelled $GA_{1+U,1}$ and $GA_{1+U,2}$ are obtained from two independent runs of genetic algorithm identification using current trajectories including a 1-C constant current charge (CCC) trajectory and a Urban Dynamometer Driving Schedule (UDDS) trajectory. The parameter set in the column labelled GA_{10+U} is obtained from genetic algorithm identification using current trajectories including a 10-C CCC trajectory and a UDDS trajectory.	106
5.2	The variables deduced from the parameter sets in [3] (Original), two independent runs of genetic algorithm identification using input current trajectories including a 1-C CCC trajectory and a UDDS trajectory ($GA_{1+U,1}$ and $GA_{1+U,2}$), and a run of genetic algorithm identification using input current trajectories including a 10-C charge trajectory and a UDDS trajectory (GA_{10+U}).	107
A.1	The numerical values of the parameters for the LiFePO ₄ battery used in Chapter 3 and the LMO-mixture battery used in Chapter 4 and 5.	144

List of Figures

2.1	The schematic of the DFN model of Li-ion batteries.	12
2.2	The schematic of the SPM of Li-ion batteries.	17
2.3	The architecture of the battery model.	26
3.1	The architecture of retrospective-cost subsystem identification for estimation of the side reaction current density. Note that the output of the SOH model is the side reaction current density J_{sd}	30
3.2	The estimates and relative estimation errors ϵ of the subsystem parameter θ and the side reaction current density J_{sd} under ideal conditions with three input currents: (a) a 1-C constant current charge and discharge (CCCD) cycle, (b) a 10-C CCCD cycle, and (c) a simulated current profile generated by an EV following an Urban Dynamometer Driving Schedule (UDDS).	40
3.3	The voltage difference ΔV of the DFN50 model caused by the current perturbation ΔI during the 1-C constant current charge mode.	47
3.4	The estimates and relative estimation errors ϵ of the subsystem parameter θ and the side reaction current density J_{sd} under the presence of (a) input and (b) output measurement noise. The bounds of the relative estimation errors are on the order of 10% as required.	48

3.5 (a) The relative estimation errors ϵ of the subsystem parameter θ and the side reaction current density J_{sd} and (b) the voltage difference under the presence of a 1% SOC error. The bound of the relative estimation errors in (a) is on the same order as expected from the voltage difference in (b).	49
3.6 The relative estimation errors ϵ of the subsystem parameter θ and the side reaction current density J_{sd} under the 1-C constant current charge mode with DFN50 as the true main system and (a) DFN30, (b) DFN10, and (c) SPM as the main system model. The differences in the voltage responses during 1-C constant current charge mode between DFN50 and (d) DFN30, (e) DFN10, and (f) SPM. The bounds of the relative estimation errors in (a), (b), and (c) are on the same orders as expected from the voltage differences in (d), (e), and (f), respectively.	50
3.7 The estimates of (a) the subsystem parameter θ and (b) the side reaction current density J_{sd} , and (c) relative estimation errors ϵ under parametric errors in R_{film} and $D_{s,n}$. (d) presents the voltage difference between the DFN50 model with values of R_{film} and $D_{s,n}$ in fresh and degraded batteries during 1-C constant current charge mode.	52
3.8 The relative estimation errors ϵ of the subsystem parameter θ and the side reaction current density J_{sd} under (a) the 1-C constant current charge (CCC) mode and (b) the urban dynamometer driving schedule (UDDS) cycle under the presence of form discrepancy between the subsystem and the subsystem model. (c) presents the relative estimation errors under the same UDDS cycle as in (b), but with the estimation algorithm shut down whenever discharge current is above 5 C. Note that shutting down the estimation algorithm during high-C-rate discharge reduces estimation errors.	55

3.9	The estimates and relative estimation errors ϵ of the subsystem parameter θ and the side reaction current density J_{sd} using a parameter set for an LMO-mixture battery under ideal conditions with two input currents: (a) a 1-C constant current charge (CCC) cycle and (b) a simulated current profile generated by an EV following an Urban Dynamometer Driving Schedule (UDDS).	62
3.10	The relative estimation errors ϵ of the subsystem parameter θ and the side reaction current density J_{sd} using a parameter set for an LMO-mixture battery under 1% SOC estimation error during 1-C constant current charge (CCC) cycle.	63
3.11	(a) The sensitivity of the voltage to the side reaction current density, $s(V J_{sd})$, and (b) the voltage difference under the presence of a 1% SOC error, $\delta V_{0\%SOC/1\%SOC}$ using the LMO-mixture parameter set. . .	64
4.1	The architecture for the two-step filter.	70
4.2	The estimates of the side reaction current density J_{sd} , the Main system state error d , and the subsystem parameter θ in the time-varying linearized battery model using the two-step filter.	82
4.3	The relative estimation errors of the side reaction current density J_{sd} , the Main system state error d , and the subsystem parameter θ in the time-varying linearized battery model using the two-step filter.	82
4.4	The relative estimation errors of the side reaction current density ($\epsilon_{J_{sd}}$), the subsystem parameter (ϵ_θ), and the Main system state error (ϵ_d) in the nonlinear battery model using the two-step filter.	84
4.5	The comparison between (a) $\Delta V_{NL}^d(k)$ and $\Delta V_L^d(k)$, (b) $\Delta V_{NL}^u(k)$ and $\Delta V_L^u(k)$, (c) $\Delta y_{NL}^d(k)$ and $\Delta y_L^d(k)$, and (d) $\Delta y_{NL}^u(k)$ and $\Delta y_L^u(k)$	85
4.6	The estimates of the side reaction current density J_{sd} , the Main system state error d , and the subsystem parameter θ in the time-varying linearized battery model using the two-step filter with $E_{1,non}(k)$ approximating E_1	89

4.7	(a) The comparison between the first entry of $E_{1,\text{non},d}$ obtained using d that correspond to 10%, 1%, 0.1%, and 0.01% SOC estimation errors. (b) The difference between the first entry of $E_{1,\text{non},d}$ corresponding to 1% SOC estimation error and i) 0.1% and ii) 0.01% SOC estimation errors.	90
4.8	The relative estimation errors of the side reaction current density ($\epsilon_{J_{\text{sd}}}$), the subsystem parameter (ϵ_θ), and the Main system state error (ϵ_d) when E_1 in the TSF is approximated using $E_{1,\text{non},d}$ for d corresponding to 0.1% SOC estimation error while the true d corresponds to 1% SOC estimation error.	92
5.1	The block diagram for estimation of the number of cyclable Li-ions using the extended Kalman filter (EKF). The true system is a battery in practice but is represented with a battery model, namely the Doyle-Fuller-Newman (DFN) model, in the simulation study presented herein. The system model is the single particle model (SPM), a simplification of the DFN model.	98
5.2	Comparison among the voltage responses of the SPM with the parameter sets from GA _{1+U,1} , GA _{1+U,2} , and Original, and the DFN model. .	106
5.3	The estimate \hat{n}_{Li} and relative estimation error $\epsilon_{n_{\text{Li}}}$ of the number of cyclable Li-ions n_{Li} under the ideal conditions for two current trajectories: (a) 1-C constant current charge (CCC) trajectory and (b) an EV current trajectory for the Urban Dynamometer Driving Schedule (UDDS).	112
5.4	(a) The estimate and (b) relative estimation error $\epsilon_{n_{\text{Li}}}$ of the number of cyclable Li-ions n_{Li} under the presence of SOC estimation error. . .	114
5.5	(a) The estimate and (b) relative estimation error $\epsilon_{n_{\text{Li}}}$ of the number of cyclable Li-ions n_{Li} under additional modeling error caused by loss of 4% anode active material and 8% cathode active material.	116

5.6 The relative estimation errors $\epsilon_{n_{\text{Li}}}$ under additional modeling error caused by loss of 4% anode active material and 8% cathode active material using the parameter set identified i) at the beginning of the service life (no re-parameterization), ii) when loss of active material is at half of the level of the modeling error (98% <i>n</i> , 96% <i>p</i>), and iii) when loss of active material is at the same level as the modeling error (96% <i>n</i> , 92% <i>p</i>).	117
5.7 The estimate \hat{n}_{Li} and relative estimation error $\epsilon_{n_{\text{Li}}}$ of the number of cyclable Li-ions n_{Li} under the presence of (a) input and (b) output measurement noise.	118
5.8 The relative estimation errors $\epsilon_{n_{\text{Li}}}$ under a combination of non-ideal conditions in Figure 5.4, 5.5, and 5.7 using the parameter set identified i) at the beginning of the service life (no re-parameterization), ii) when loss of active material is at half of the level of the modeling error (98% <i>n</i> , 96% <i>p</i>), and iii) when loss of active material is at the same level as the modeling error (96% <i>n</i> , 92% <i>p</i>).	119
5.9 The sensitivity of the voltage to the number of cyclable Li-ions, $s(V n_{\text{Li}})$	121
B.1 True film resistance and the film resistance estimated by RCSI. Shaded regions 1–4 indicate the constant current discharging mode, constant voltage discharging mode, constant current charging mode, and constant voltage charging mode, respectively.	149
B.2 A magnified view of Figure B.1.	149
B.3 Identified θ by RCSI.	150
B.4 Identified θ by RLS when $P(0) = 1 \times 10^{10}$	151
B.5 Voltage change vs. relative film resistance growth between successive cycles.	152
B.6 A magnified view of film resistance identification with output measurement noise when the standard deviation of the noise is 0.02 mV. . . .	153

B.7 A magnified view of film resistance identification with output measurement noise when the standard deviation of the noise is 0.2 mV.	153
B.8 The difference in output voltage for various differences in input current.	154
B.9 A magnified view of film resistance identification with input noise when the standard deviation of the noise is 0.5 mA.	155
B.10 A magnified view of film resistance identification with input noise when the standard deviation of the noise is 5 mA.	156
B.11 The output error under various initial conditions.	158
B.12 The identified film resistance under various initial conditions.	158
B.13 The true film resistance under various initial conditions.	159
B.14 The true output voltage under various initial conditions.	159

List of Appendices

A	The Values of the Electrochemical Parameters and Functions Used in the Simulations	143
B	Robustness of Estimation of SEI Film Resistance using RCSI	146

Nomenclature of Electrochemical Variables

This nomenclature contains only the electrochemical variables. The variables for the control and estimation purposes either follow the conventions in the control literature or are explained within the context.

0_r	the coordinate at the center of particles along r direction, m
$0_j/L_j$	the coordinate at the starting/ending point of an electrode along the x direction, m
A	total area of sections, m^2
$a_{s,j}$	specific surface area of porous electrodes, m^{-3}
$c_{h,j}$	Li-ion concentration, mol m^{-3}
$c_{s,\max,j}$	maximum concentration in the solid phase, mol m^{-3}
$c_{se,j}$	The Li-ion concentration in the solid phase at the surface of particles, mol m^{-3}
$D_{h,j}$	diffusion coefficient, $\text{m}^2 \text{ s}^{-1}$
F	Faraday constant, 96487 C mol^{-1}
f_j	activity coefficient
I	current, A
$i_{0,j/sd}$	intercalation/side reaction exchange-current density, A m^{-2}
$i_{h/\text{total}}$	phasic/total superficial current density, A m^{-2}
$J_{1/sd/\text{total},j}$	intercalation/side reaction/total current density, A m^{-3}
k_j	reaction rate, $\text{A m}^4 \text{ mol}^{-2}$
M_{SEI}	molecular weight, mol kg^{-1}

R	universal gas constant, 8.314 J mol ⁻¹
r	coordinate along the radius of particles, m
R_{film}	solid-electrolyte-interphase film resistance, Ω m ²
R_j	radius of electrode particles, m
R_{SEI}	initial film thickness, Ω m ²
T	temperature, K
t	time, s
t^+	transference number
$U_{\text{ref},j/\text{sd}}$	equilibrium potential for intercalation/side reaction, V
V	voltage, V
x	coordinate along the thickness of the anode-separator-cathode sandwich, m

Greek Symbols

$\alpha_{a/c,j}$	anodic/cathodic transfer coefficients of electrochemical reaction
$\bar{\theta}_{j,0\%}$	$\bar{\theta}_j$ corresponding to a depleted battery
$\bar{\theta}_{j,100\%}$	$\bar{\theta}_j$ corresponding to a fully charged battery
$\bar{\theta}_j$	the percentage of the average solid Li-ion concentration with respect to the theoretical maximal Li-ion concentration
δ_{film}	film thickness, m
$\eta_{j/\text{sd}}$	overpotential for intercalation/side reaction, V
$\kappa^{\text{eff}}/\sigma_j^{\text{eff}}$	conductivity of electrolyte/solid phase, S m ⁻¹
$\phi_{h,j}$	potential, V
ρ_{SEI}	film density, kg m ⁻³
θ_j	the percentage of the solid Li-ion concentration at the surface of particles with respect to the theoretical maximal Li-ion concentration
$\varepsilon_{h,j}$	volume fraction

Subscripts

h	Phase name, where s and e stand for solid phase and electrolyte phase, respectively.
-----	--

- j Section name, where p, n and sep stand for cathode, anode and separator, respectively.

Abstract

This dissertation explores and compares the effectiveness of estimating two health-relevant electrochemical variables, the side reaction current density and the number of cyclable Li-ions, as indicators of battery state of health (SOH) in battery management systems of electric vehicles (EV) and hybrid electric vehicles (HEV). The choice of these two electrochemical variables is based on the assumption that battery degradation is mainly caused by consumption of cyclable Li-ions. This assumption is valid for the two widely-used types of EV/HEV batteries considered herein, namely LiFePO₄ and LMO-based mixture batteries.

This dissertation provides formulations to estimate these two electrochemical variables from measurements of battery terminal voltage and current. Estimation is necessary here because the electrochemical variables cannot be measured on-board. Estimation of the side reaction current density is formulated as a subsystem identification problem and is solved using retrospective-cost subsystem identification. A new subsystem identification algorithm, the two-step filter, is also developed to improve the estimation accuracy of the side reaction current density under the presence of state of charge (SOC) estimation errors. On the contrary, the number of cyclable Li-ions is estimated as an unknown battery parameter using the extended Kalman filter.

This dissertation also analyzes the robustness of estimation of the two electrochemical variables by providing a framework to obtain the lower bound of relative estimation errors of each of the two variables under non-ideal conditions for algorithms that estimate the variable by minimizing the error between measured voltage and estimated voltage. This framework determines that the lower bound of the rela-

tive estimation error of a variable is proportional to the error in either measurement or estimate of battery terminal voltage caused by non-ideal conditions, and inversely proportional to the sensitivity of the voltage to the variable and the magnitude of the variable itself. This framework also yields the same lower bound for the covariance of unbiased estimates as given by the Fisher information.

The effectiveness of estimating the side reaction current density and the number of cyclable Li-ions as SOH indicators is also discussed through comparison. Compared to the number of cyclable Li-ions or other SOH indicators such as capacity and internal resistance, the side reaction current density is a more ideal SOH indicator when it can be estimated accurately, because it can instantaneously indicate battery degradation rate. However, estimation of the side reaction current density under practical non-ideal conditions is fundamentally difficult due to the fact that the sensitivity of the voltage to the side reaction current density and the magnitude of the side reaction current density are both low. On the other hand, the number of cyclable Li-ions is a promising SOH indicator for battery management systems in practice because it provides an indication of the remaining capacity from the first principles, can be estimated using a standard algorithm and simple models, and demonstrates high robustness to non-ideal conditions.

Future extensions of this work include i) studying the impact of temperature on estimation of health-relevant electrochemical variables by including thermal dynamics in the model, ii) validating experimentally estimation of the number of cyclable Li-ions, and iii) extending estimation of the side reaction current density to other side-reaction-based battery degradation and safety problems such as Lithium plating and dendrite formation.

Chapter 1

Introduction

1.1 Background and Literature Review

1.1.1 Battery State of Health Monitoring

The battery management system (BMS) is an essential component for development of a variety of battery-powered systems, such as electric vehicles (EV) and hybrid electric vehicles (HEV), underwater vehicles, aircrafts, portable electronic devices, medical implant devices, and power grid [4, 5, 6]. Among all the functionalities of the BMS, state of health (SOH) monitoring provides critical information for balancing the trade-off between maximizing system performance and minimizing battery degradation [7, 8]. The SOH refers to the ability in delivering energy and power of a used battery compared to a fresh battery [9]. A battery reaches the end of its service life when its health degrades to a pre-defined level. A short battery life is a significant limitation for the battery-powered systems because it greatly increases the cost and reduces the durability and reliability of the overall system. By monitoring battery health, controllers can better manage the use of the battery to minimize its degradation, thereby elongating its service life.

This dissertation focuses on the SOH monitoring of EV/HEV batteries. The cost of EV/HEV batteries can take up to 20% of the price of the vehicle itself [10] and thus elongating the battery life is essential to reducing the cost of the EV and HEV,

and further facilitates the market penetration of the EV and HEV. Furthermore, a battery in good health is also a necessary component for the safety, reliability, and comfort of the EV and HEV [4]. Hence, the SOH monitoring is a major focus for the development of the EV and HEV.

1.1.2 Battery Chemistries

The EV/HEV batteries are always Li-ion batteries with certain cathode materials. This dissertation focuses on two types of cathode materials that are popular in the EV/HEV industry.

The first type of the cathode materials is LiFePO_4 . LiFePO_4 is one of the primary materials for EV/HEV batteries for its flat voltage profile, low material cost, abundant material supply and better environmental compatibility compared with other cathode materials [11, 12, 13, 14, 15]. Some example EVs that uses LiFePO_4 batteries on the market include BYD F3DM, F6DM, and E6 [16], and EV-Fleet electric pickup trucks. LiFePO_4 is also a very popular battery chemistry for electric motorcycles and scooters.

The second type of the cathode material is LiMn_2O_4 (LMO) mixed with other Li-compounds. This group of materials is referred to as LMO-mixture materials herein. LMO battery material is favored by the HEV/EV industry because of its high specific energy and power, low cost, and high thermal stability [12, 17]. However, a battery with LMO alone as the cathode material is not suitable for HEV/EV applications because of its short life span [17], which is mainly a result of dissolution of Mn [18, 19]. Adding other Li-ion compounds, such as LiCoO_2 (LCO), LiNiO_2 (LNO), and LiNiMnCoO_2 (NMC), to LMO-cathode can increase the battery life by reducing Mn dissolution [20]. Some examples of LMO-mixture materials in the HEV/EV industry include the Nissan Leaf and the Renault Kangoo that use LMO mixed with LNO as the cathode material, as well as the Chevrolet Volt that uses LMO mixed with NMC as the cathode material.

These two types of cathode materials cover most of the EV/HEV batteries available in the market. Other materials that are not as widely used, such as LiNiCoAlO_2 (NCA) that is reported to be used by Tesla Motor Company, are not considered in

this dissertation.

1.1.3 Battery Degradation Effects and Mechanisms

The degradation of battery health is always reflected in effects such as i) capacity fade [21] and ii) internal impedance rise, which leads to power fade [22].

These effects are caused by a variety of degradation mechanisms, in the anode, separator, and cathode, as well as collectors. These degradation mechanisms can be classified as electrochemical, such as solid-electrolyte interface (SEI) film formation [23], binder decomposition, lithium plating [24, 25], dendrite formation [26], and electrolyte decomposition, and structural, such as crack formation, porosity change, contact loss, and current collector corrosion [27]. For both LiFePO₄ and LMO-mixture batteries, the electrochemical degradation mechanisms that consume cyclable Li-ions in the anode are the primary degradation mechanisms under normal use conditions [28, 29, 30].

These Li-ion consuming degradation mechanisms are caused by side reactions in the battery [28, 31]. The side reactions are irreversible and they consume the cyclable Li-ions in the battery and lead to the decrease in the total number of the cyclable Li-ions. The rate of the consumption of the cyclable Li-ions by side reactions is quantified by the side reaction current density. Integrating the side reaction current density across the width of the battery anode-separator-cathode and over time yield the decrease of the total number of cyclable Li-ions. The decreasing cyclable Li-ions leads to the effect of capacity fade. In some degradation mechanisms, the side reactions also form by-products. For example, for the degradation mechanism that forms SEI film, the SEI film is the by-product that the side reaction forms. The increase in the by-products such as the SEI film leads to the rising internal impedance and thus lead to the power fade.

1.1.4 SOH Indicators

In the context of battery management, the SOH, which is an abstract concept, needs to be deduced from other quantities that are correlated with battery health. This dissertation refers to these quantities as SOH indicators. Monitoring of the SOH in battery management systems is equivalent to monitoring the changes in the values of certain SOH indicators.

Based on the choice of the SOH indicator, the SOH monitoring literature can be divided into two categories. Most of the literature uses battery degradation effects, such as capacity fade [32, 33, 34, 21, 35, 36, 37, 38] and power fade [39, 40], as the SOH indicator. Empirical models, such as equivalent circuit models, are often sufficient for these applications as the mapping between the SOH indicator and the battery voltage, current, and temperature. The simplicity of these models is the key advantage to these techniques.

The second category uses health-relevant electrochemical variables as the SOH indicator. Some example electrochemical variables used as SOH indicators are the number of cyclable Li-ions [41], the SEI film resistance [42, 43, 44, 45, 46, 8], and Lithium deposition [47]. First-principle models, or electrochemical models, are required to estimate these electrochemical variables.

Compared to the first category of SOH indicators, the second category of SOH indicators have several benefits. First, compared to the effects, which are not concerned with the mechanisms causing the effects, the electrochemical variables can give more insight on degradation from the first principles. Secondly, the values of electrochemical variables can be less sensitive to changes in environmental conditions and use patterns. If an electrochemical variable is measured [48], its measurement is expected to be unique under different environmental conditions and use patterns. In contrast, the measurements of effects such as the capacity are affected by the temperature and C-rate under which the measurements are taken [49]. When the electrochemical variables are estimated, due to the use of first-principle models, their estimates have taken the influence of environmental conditions and use patterns under consideration.

For estimation of the degradation effects, where the empirical models are used, the parameters of the empirical models are subject to change under different environmental conditions and use patterns under consideration and can yield different estimates of the capacity and internal resistance under different environmental conditions and use patterns.

However, compared to the wide use of the effects-based SOH indicators in battery management systems, using the electrochemical variables as SOH indicators for battery management purpose is a relatively new and less explored area. There has not been a comprehensive study that explores a variety of electrochemical-based SOH indicators and investigates their effectiveness in indicating the SOH for battery management purpose.

1.2 Research Objective

The research objective of this dissertation is to fill the gap in literature by exploring and comparing the effectiveness of a group of electrochemical variables as SOH indicators for the purpose of EV/HEV battery management.

The effectiveness explored herein is threefold. First, the effectiveness of using an electrochemical variable as the SOH indicator concerns how useful the information carried by the variable is regarding the SOH, including i) how generally the variable can be applied to indicate the changes of the SOH due to different degradation mechanisms and ii) how the information can be applied to facilitate different functionalities of battery management. Second, the effectiveness concerns the availability of the variable, through either measurements or estimation. To evaluate this aspect of the effectiveness, the following questions need to be answered. i) Can the variable be measured? ii) Is the procedure easy to operate? Is there any special equipment required? iii) How long does it take to take the measurements? Can the measurements obtained in-situ and in real time? iv) Is it costly to make the measurements? v) If a measurement that is at the same time accurate, easy, and inexpensive is not available, estimation can be considered as an alternative. Is the variable observable? vi) Is it

possible to design an algorithm with reasonable complexity to estimate the variable? vii) Is the algorithm computationally efficient? viii) How accurate the estimates can be under ideal conditions? Finally, the effectiveness concerns how accurately the variable can be obtained in practice. If the variable is obtained via measurements, the resolution and accuracy of the measurements are concerned. If the variable is obtained via estimation, the robustness of the estimation under practical non-ideal conditions is concerned. The non-ideal conditions include measurement noise, estimation errors of other signals, and modeling errors.

1.3 Methodology

1.3.1 Selection of SOH Indicators

For the Li-ion consuming electrochemical mechanisms that are identified to be the primary degradation mechanisms for the two popular EV/HEV battery types under normal use, two electrochemical variables are identified as candidates for the general SOH indicator for EV/HEV batteries. The first one is the side reaction current density, which measures the rate of the consumption of the cyclable Li-ions. The side reaction current density indicates the SOH by providing instantaneous information regarding how fast the battery is degrading. This information is useful for the control modules in the battery management system so that health-conscious control decisions can be made as soon as a high degradation rate is detected to avoid further degrading the battery inadvertently. Moreover, the side reaction current density is a general SOH indicator because it widely exists in all electrochemical degradation mechanisms that consume cyclable Li-ions [31]. The second general SOH indicator candidate is the number of cyclable Li-ions. All the electrochemical degradation mechanisms that consume cyclable Li-ions cause decrease of the number of cyclable Li-ions, so the number of cyclable Li-ions can serve as a general SOH indicator for the EV/HEV batteries.

For degradation mechanisms that produce by-products, the quantity of the by-

products can also be a valid SOH indicator. For example, for the SEI film formation, the SEI film thickness or the SEI film resistance can be a useful SOH indicator [42, 43, 44, 45, 46, 8]. However, these by-products are mechanism-specific and not generally applicable to all the degradation mechanisms of interest. Moreover, for the SEI film thickness/resistance, there have been arguments questioning its monotonic growth during the overall life of the batteries [30, 29, 50]. Therefore, these electrochemical by-products such as the SEI film are not the primary focus of this dissertation as SOH indicators.

1.3.2 Estimation

The unavailability of the electrochemical variables through common non-invasive measurements makes their estimation necessary for in-situ SOH monitoring. Therefore, in this dissertation, different estimation algorithms are applied to estimate the side reaction current density and the number of cyclable Li-ions individually based on the different role they play in the battery system. The estimation of the side reaction current density is formulated as an inaccessible subsystem identification problem, where the battery health subsystem is treated as an inaccessible subsystem with the side reaction current density as the output. Inaccessibility in this context refers to the fact that the inputs and outputs of the subsystem are not measurable in-situ. This subsystem is identified using retrospective-cost subsystem identification (RCSI) algorithm, and the output of the identified battery health subsystem provides an estimate for the side reaction current density. This formulation is due to the need to track the instantaneous value of the side reaction current density. Identification of the subsystem that produces the side reaction current density provides a way to track the dynamics of the side reaction current density instantaneously. On the other hand, the number of cyclable Li-ions is considered as an unknown parameter of the battery system. This is because the number of cyclable Li-ions has much slower dynamics than the battery charging and discharging dynamics, and thus can be considered a constant during the time scope of estimation. Therefore, the number of cyclable Li-ions is estimated using estimation methods such as the extended Kalman filter (EKF)

that estimate parameters in nonlinear systems.

1.4 Research Questions

The rest of this dissertation focuses on exploring and comparing the effectiveness of estimating the side reaction current density and the number of cyclable Li-ions as the SOH indicator. In particular, the following research questions are posed.

- Can the estimation of the side reaction current density be formulated as an inaccessible subsystem identification problem and solved with RCSI? How robust can the estimation be?
- Can the estimation of the number of cyclable lithium-ions be formulated as a parameter estimation problem and solved with nonlinear estimation methods such as the EKF? How robust can the estimation be?
- Given the methods used to estimate the side reaction current density and the number of cyclable Li-ions, which variable can be more effectively estimated as an SOH indicator?
- Compared to the effects-based SOH indicators, do the estimates of the side reaction current density and the number of cyclable Li-ions provide new insight in degradation? Are the side reaction current density and the number of cyclable Li-ions promising alternatives to the degradation effects as SOH indicators in battery management systems?

1.5 Dissertation Organization

The rest of the dissertation is organized as follows. Chapter 2 summarizes three electrochemical battery models in the literature to prepare for the development of the estimation algorithms in Chapter 3 – 5. Chapter 3 presents estimation of the side reaction current density using RCSI and its robustness to non-ideal conditions

such as measurement noise, state of charge (SOC) estimation errors, and modeling errors. Chapter 4 develops a new subsystem identification algorithm, the two-step filter (TSF), to improve the accuracy of estimating the side reaction current density when SOC estimation errors are present. Chapter 5 presents estimation of the number of cyclable Li-ions using the EKF and its robustness to non-ideal conditions. Chapter 6 gives a comparison between the effectiveness of the side reaction current density and the number of cyclable Li-ions as SOH indicators, as well as a comparison of these electrochemical-based SOH indicators against the effects-based SOH indicators. Chapter 7 provides the summary and conclusions of the dissertation. The future work that can potentially extend the work in this dissertation is also briefly summarized in Chapter 7.

Chapter 2

Battery Models

2.1 Introduction

A battery model is necessary in this study for two reasons. First, the estimation algorithms require a map relating the electrochemical variables that are unavailable from measurements to the signals that are measurable in practice. In this work, this map is a battery model that relates the side reaction current density/the number of cyclable Li-ions to the battery terminal voltage and current. Second, a battery model is required to represent a battery in simulations.

This chapter presents the battery models used in this work. The electrochemical models are adopted to support the use of an electrochemical SOH indicator. These battery models contain two categories: the SOC models and the SOH models. The SOC models represent the charge and discharge dynamics of the battery that governs the battery SOC evolution, and determine the battery voltage as its output. Notice that the SOC models contain not only the SOC dynamics, but also the dynamics regarding the Li-ion concentration in the electrolyte phase and potential. However, for simplicity, this model is referred to as the SOC model herein to differentiate it from the SOH model. The SOH models represent a health subsystem of the battery that governs the instantaneous decreasing of the number of cyclable Li-ions. For each of the models, the electrochemical form, which includes the electrochemical equations, is presented first, and then the electrochemical form is simplified to obtain a form

that is suitable for estimation purpose. This form is referred to as the estimation form.

2.2 Battery SOC Models

2.2.1 Doyle-Fuller-Newman (DFN) Model

The Doyle-Fuller-Newman (DFN) model [51, 52] as depicted in Figure 2.1 is a well-accepted electrochemical model for Li-ion batteries. In the DFN model, the structure of the solid phase in each electrode is modeled with a series of spherical particles, leading to spatial discretization along the thickness of the anode-separator-cathode sandwich, which is defined as the x dimension. The r dimension represents the direction along the radius of each spherical particle. The SOC is measured by the Li-ion concentration in the solid particles.

2.2.1.1 The Electrochemical Form

This section briefly summarizes the electrochemical equations of the DFN model. More detailed descriptions can be found in [51, 52, 53].

Diffusion of Li-ions inside each electrode particle is governed by Fick's law along the r dimension, while diffusion within the electrolyte is along the x dimension; i.e.,

$$\frac{\partial c_{s,j}}{\partial t} = \nabla_r (D_{s,j} \nabla_r c_{s,j}), \quad (2.1)$$

$$\frac{\partial c_e}{\partial t} = \frac{\partial}{\partial x} \left[D_{e,j} \frac{\partial c_e}{\partial x} + \frac{1 - t^+}{\varepsilon_{e,j} F} i_e \right], \quad (2.2)$$

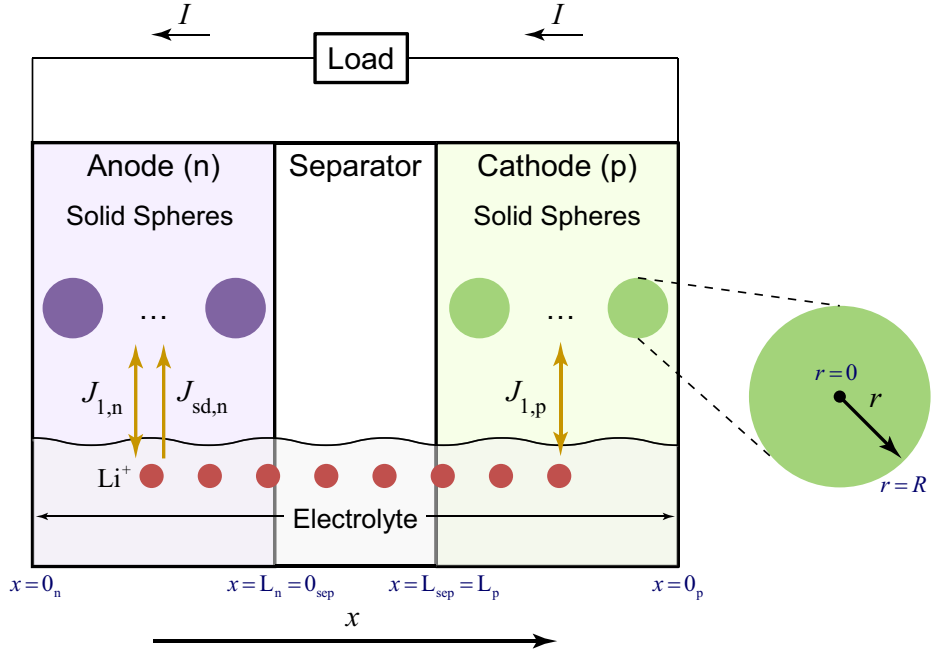


Figure 2.1: The schematic of the DFN model of Li-ion batteries.

with the boundary conditions

$$\frac{\partial c_{s,j}}{\partial r}(0_r, t) = 0, \quad (2.3)$$

$$\frac{\partial c_{s,j}}{\partial r}(R_j, t) = -\frac{J_{1,j}(R_j)}{D_{s,j} F a_{s,j}}, \quad (2.4)$$

$$\frac{\partial c_e}{\partial x}(0_j, t) = 0, \quad (2.5)$$

$$\varepsilon_{e,n} D_{e,n} \frac{\partial c_e}{\partial x}(L_n, t) = \varepsilon_{e,sep} D_{e,sep} \frac{\partial c_e}{\partial x}(0_{sep}, t), \quad (2.6)$$

$$\varepsilon_{e,sep} D_{e,sep} \frac{\partial c_e}{\partial x}(L_{sep}, t) = \varepsilon_{e,p} D_{e,p} \frac{\partial c_e}{\partial x}(L_p, t), \quad (2.7)$$

$$c_e(L_n, t) = c_e(0_{sep}, t), \quad (2.8)$$

$$c_e(L_{sep}, t) = c_e(L_p, t). \quad (2.9)$$

The SOC is computed from $c_{s,n}$ through

$$\bar{\theta}_n = \frac{\bar{c}_{s,n}}{c_{s,max,j}}, \quad (2.10)$$

which measures the percentage of the average solid concentration $\bar{c}_{s,n}$ with respect to

the theoretical maximal Li-ion concentration. Then the SOC is computed as

$$\text{SOC} = \frac{\bar{\theta}_n - \bar{\theta}_{n,0\%}}{\bar{\theta}_{n,100\%} - \bar{\theta}_{n,0\%}} \times 100\%, \quad (2.11)$$

where $\bar{\theta}_{n,100\%}$ and $\bar{\theta}_{n,0\%}$ are $\bar{\theta}_n$ at the full-charge and depleted states, respectively [54].

The distributions of the potential in the solid and electrolyte phases are both along the x dimension,

$$\frac{\partial \phi_{s,j}}{\partial x} = \frac{i_e - i_{\text{total}}}{\sigma_j^{\text{eff}}}, \quad (2.12)$$

$$\frac{\partial \phi_{e,j}}{\partial x} = \frac{2RT}{F} (1 - t^+) \left(1 + \frac{d \ln f_j}{d \ln c_{e,j}} \right) \frac{\partial \ln c_{e,j}}{\partial x} - \frac{i_e}{\kappa_j^{\text{eff}}}, \quad (2.13)$$

with the boundary conditions

$$\frac{\partial \phi_{s,j}}{\partial x} (L_j) = 0, \quad (2.14)$$

$$\phi_e (0_n, t) = 0, \quad (2.15)$$

$$\phi_e (L_n, t) = \phi_e (0_{\text{sep}}, t), \quad (2.16)$$

$$\phi_e (L_{\text{sep}}, t) = \phi_e (L_p, t). \quad (2.17)$$

The total superficial current density i_{total} in (2.12) is obtained by averaging the current I over the total area of electrodes A ,

$$i_{\text{total}} = \frac{I}{A}, \quad (2.18)$$

where positive I indicates discharge. The superficial current density i_e is governed by

$$\frac{\partial i_e}{\partial x} = J_{\text{total},j}, \quad (2.19)$$

$$i_e (0_j, t) = 0, \quad (2.20)$$

where $J_{\text{total},j}$ represents the sum of the current densities of all electrochemical reactions in the battery, including the intercalation reaction that governs the SOC process and

the side reactions that govern the SOH process. Notice that there is neither an intercalation reaction nor a side reaction in the separator, i.e., $J_{\text{total,sep}} = 0$, and thus

$$i_e(x, t) = i_{\text{total}} \quad \forall x \in [0_{\text{sep}}, L_{\text{sep}}]. \quad (2.21)$$

The exchange of Li-ions between the solid electrodes and electrolyte is referred to as the intercalation reaction (represented by the double-sided arrows in Figure 2.1). The intercalation reaction is reversible, and thus the Li-ions used in this reaction can be recycled for future reactions. This reaction is governed by the Butler-Volmer equation

$$J_{1,j} = i_{0,j} a_{s,j} \left[\exp\left(\frac{\alpha_{a,j} F}{RT} \eta_j\right) - \exp\left(-\frac{\alpha_{c,j} F}{RT} \eta_j\right) \right], \quad (2.22)$$

where

$$\begin{aligned} i_{0,j}(x, t) &= k_j (c_{s,j}(R_j, t))^{\alpha_{c,j}} \\ &\quad [c_e(x, t) (c_{s,max,j} - c_{s,j}(R_j, t))]^{\alpha_{a,j}}, \end{aligned} \quad (2.23)$$

$$\eta_p = \phi_{p,s} - \phi_{p,e} - U_{\text{ref},p}(\theta_p), \quad (2.24)$$

$$\eta_n = \phi_{n,s} - \phi_{n,e} - U_{\text{ref},n}(\theta_n) - \frac{J_{\text{total,n}}}{a_{s,j}} R_{\text{film}}, \quad (2.25)$$

where the reference potentials $U_{\text{ref},j}$ are functions of the Li-ion concentration at the surface of the particle through the ratio θ_j defined as

$$\theta_j \triangleq \frac{c_{se,j}}{c_{s,max,j}}, \quad (2.26)$$

where

$$c_{se,j} = c_{s,j}|_{r=R_j}. \quad (2.27)$$

The particular reference potential functions depend on the materials of the electrodes. The intercalation current density $J_{1,j}$ indicates the speed of the charge and discharge

process. The SEI film, whose resistance is captured by R_{film} in (2.25), is assumed to accumulate only on the anode [28].

The total current density $J_{\text{total,j}}$ is split into the intercalation current density $J_{1,j}$ and the side reaction current density $J_{\text{sd},j}$, which is the current density for the side reactions that consume cyclable Li-ions and lead to battery degradation; i.e.,

$$J_{\text{total,j}} = J_{1,j} + J_{\text{sd},j}. \quad (2.28)$$

Hence, the side reactions affect the SOC process by reducing the available current density for the intercalation.

By assuming a uniform distribution of the initial Li-ion concentration in both electrodes, the total number of cyclable Li-ions n_{Li} in the battery can be computed as in [41]

$$\begin{aligned} n_{\text{Li}} &= \epsilon_{s,p} L_p A \bar{c}_{s,p}(0) + \epsilon_{s,n} L_n A \bar{c}_{s,n}(0) \\ &= \epsilon_{s,p} L_p A c_{s,\max,p} \bar{\theta}_p(0) + \epsilon_{s,n} L_n A c_{s,\max,n} \bar{\theta}_n(0) \\ &= \epsilon_{s,p} L_p A c_{s,\max,p} \theta_p(0) + \epsilon_{s,n} L_n A c_{s,\max,n} \theta_n(0). \end{aligned} \quad (2.29)$$

The final equality in (2.29) holds because $\theta_j = \bar{\theta}_j$ when the Li-ion concentration is uniformly distributed.

2.2.1.2 The Estimation Form

The electrochemical form of the DFN model is simplified into the state space form with two inputs and two outputs. First, the partial differential equations (PDEs) contained in the SOC model are reduced to finite dimension as a group of ordinary differential equations (ODEs). The PDE (2.1) governing diffusion in the solid phase is reduced to finite dimension through a second-order Padé approximation of the Laplace transformation of (2.1) [55]. The result of the Padé approximation is

$$\frac{c_{se,j}}{J_{1,j}}(s) = -\frac{5(21D_{s,j} + 2R_j^2 s)}{3F\epsilon_{s,j}(35D_{s,j} + R_j^2 s)s}. \quad (2.30)$$

The spatial dimension of the PDE (2.2) governing diffusion in the electrolyte phase is discretized with the central difference method. Therefore, the state equations of the SOC model are obtained by stacking the ODEs reduced from PDEs (2.2) for all discretization nodes in the x dimension and the ODEs from state space realization of the transfer function (2.30) for all particles. Therefore, the number of the states in the resulting state space model depends on how fine the discretization of the x dimension is. If there are N particles per electrode and M discretization nodes in the separator, with the last node in the anode being also the first node in the separator, and the last node in the separator being also the first node in the cathode, then the total number of the states is $6N + M - 2$.

The inputs to the SOC model are reformulated to be the exogenous input I and the side reaction current density $J_{\text{sd},j}$ herein. In the electrochemical form of the DFN model, the inputs are $J_{1,j}$ and I . However, in the simplified form, by applying (2.28) combined with the fact that $J_{\text{total},j}$ can be calculated from the current I alone, $J_{1,j}$ is expressed as a function of $J_{\text{sd},j}$ and I .

Finally, two outputs are calculated from the DFN model, namely the exogenous output V and the input y_ϕ to the SOH model. The exogenous output V is the difference between the potential of the solid phases of the two electrodes, i.e.,

$$V(t) = \phi_{s,p}(0_p, t) - \phi_{s,n}(0_n, t). \quad (2.31)$$

The input y_ϕ to the SOH model is an optional output that is only required when the SOC model is integrated with the SOH model, and thus it is defined in (2.58) in the development of the SOH model in Section 2.3.

The equations for the DFN model are then put into the discrete form for computation purpose, i.e.,

$$x(k+1) = f(x(k), u(k), w(k)), \quad (2.32)$$

$$y(k) = g(x(k), u(k), w(k)), \quad (2.33)$$

$$y_0(k) = g_0(x(k), u(k), w(k)), \quad (2.34)$$

where states $x(k) \in \mathbb{R}^n$ reflect the battery SOC, the electrolyte concentration, and the potential distribution in the solid and electrolyte phase, the input w and output y_0 are the current I and the voltage V , respectively, the input u to the SOC model is the side reaction current density $J_{\text{sd},j}$, and the output y of the SOC model is y_ϕ . The function $f(\cdot)$ in (2.32) represents (2.1) and (2.2), while $g(\cdot)$ in (2.33) and $g_0(\cdot)$ in (2.34) are static relationships represented by (2.58) and (2.31), respectively.

2.2.2 Single Particle Model (SPM)

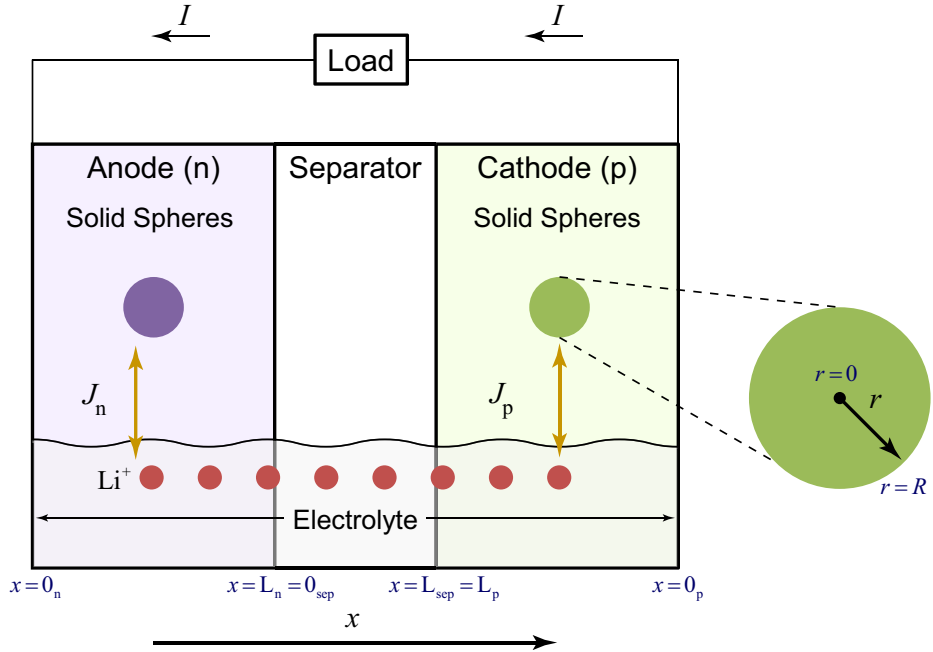


Figure 2.2: The schematic of the SPM of Li-ion batteries.

The Single Particle Model (SPM) [56, 54] is a simplified version of the DFN model, where the solid phase of each electrode is represented with only one spherical particle (as depicted in Figure 2.2) and the distribution of concentration and current density along the width of anode-separator-cathode sandwich are ignored. This simplification eliminates all the states that represent the concentration and potential distribution in the x dimension, which results in a system with fewer states than the DFN model. The SPM can represent the battery charge and discharge dynamics accurately when the current C-rate is low (usually ≤ 1 C).

2.2.2.1 The Electrochemical Form

The main focus of the section is how the electrochemical form of the SPM can be simplified from the electrochemical form of the DFN model presented in Section 2.2.1.2 based on the assumptions made in the SPM. More detailed description about the SPM can be found in [54].

The SPM represents each electrode with only one particle, thus eliminating the representation of the distribution of Li-ions along the x direction, i.e., only one group of (2.1), (2.3), and (2.4) is needed for each electrode.

Moreover, uniform and constant distribution of the electrolyte concentration is assumed in the SPM, and thus (2.2) and (2.5) – (2.9) can be eliminated. The electrolyte concentration is instead modeled by

$$c_e(x, t) = \bar{c}_e, \quad (2.35)$$

where \bar{c}_e is a constant. Therefore, (2.13) is simplified as

$$\frac{\partial \phi_{e,j}}{\partial x} = -\frac{i_{\text{total}}}{\kappa_j^{\text{eff}}}. \quad (2.36)$$

Furthermore, $J_{\text{total},j}$ is assumed to be uniformly distributed along the x dimension of each electrode, and thus (2.19) is simplified as

$$J_{\text{total},n} L_n = i_e(L_n) - i_e(0_n), \quad (2.37)$$

$$J_{\text{total},p} L_p = i_e(0_p) - i_e(L_p), \quad (2.38)$$

Substituting the (2.18), (2.20) and (2.21) into (2.37) and (2.38) yields

$$J_{\text{total},n} = \frac{I}{A L_n}, \quad (2.39)$$

$$J_{\text{total},p} = \frac{I}{A L_p}. \quad (2.40)$$

Assuming uniform distribution of the initial Li-ion concentrations in both elec-

trodes as in the DFN model, the number of cyclable Li-ions is computed as in [41]

$$n_{\text{Li}} = \epsilon_{\text{s,p}} L_{\text{p}} A c_{\text{s,max,p}} \theta_{\text{p}}(0) + \epsilon_{\text{s,n}} L_{\text{n}} A c_{\text{s,max,n}} \theta_{\text{n}}(0). \quad (2.41)$$

2.2.2.2 The Estimation Form

The state equation of the SPM is obtained from (2.1) for the anode and cathode through similar manner as in the DFN model. The number of the states in the SPM is significantly reduced compared to the DFN model with multiple particles per electrode. The number of the states for the SPM herein is 4 because the second-order Padé approximation is used. The SPM is discretized herein using first-order hold to expedite the simulation. $c_{\text{s,j}}$ is obtained through the discretized equations

$$x_{\text{j}}(k+1) = A_{\text{j}} x_{\text{j}}(k) + B_{\text{j}} J_{1,\text{j}}, \quad (2.42)$$

$$c_{\text{se,j}}(k+1) = C_{\text{j}} x_{\text{j}}(k) + D_{\text{j}} J_{1,\text{j}}, \quad (2.43)$$

where

$$A_{\text{j}} = \begin{bmatrix} 1 & 0 \\ 0 & e^{-\frac{35D_{\text{s,j}}T_{\text{s}}}{R_{\text{j}}^2}} \end{bmatrix}, \quad (2.44)$$

$$B_{\text{j}} = \begin{bmatrix} \frac{R_{\text{j}}^2 T_{\text{s}}}{35D_{\text{s,j}}} \\ \frac{-70D_{\text{s,j}}T_{\text{s}}}{R_{\text{j}}^2} \left(\frac{35D_{\text{s,j}}T_{\text{s}}}{R_{\text{j}}^2} \right)^2 R_{\text{j}}^4 \\ \frac{1225D_{\text{s,j}}^2 T_{\text{s}}}{1} \end{bmatrix}, \quad (2.45)$$

$$C_{\text{n}} = \begin{bmatrix} -\frac{105D_{\text{s,j}}^2}{R_{\text{j}}^3 F a_{\text{s,j}} D_{\text{s,j}}} & -\frac{7D_{\text{s,j}}}{R_{\text{j}} F a_{\text{s,j}} D_{\text{s,j}}} \end{bmatrix}, \quad (2.46)$$

$$D_{\text{j}} = \begin{bmatrix} \left(2-2e^{-\frac{35D_{\text{s,j}}T_{\text{s}}}{R_{\text{j}}^2}} \right) R_{\text{j}}^4 - 70D_{\text{s,j}}R_{\text{j}}^2 T_{\text{s}} - 525D_{\text{s,j}}^2 T_{\text{s}}^2 \\ 350D_{\text{s,j}}^2 R_{\text{j}} T_{\text{s}} F a_{\text{s,j}} \end{bmatrix}. \quad (2.47)$$

where T_{s} is the sampling time. The input to (2.42) – (2.43) is $J_{1,\text{j}}$. As in the DFN model, $J_{1,\text{j}}$ is reformulated herein as the linear combination of two inputs, namely the exogenous input I and the side reaction current density $J_{\text{sd,j}}$, based on (2.28). The final state equation for the SPM is obtained by stacking (2.42) for both anode and

cathode.

Unlike the DFN model where the outputs are solved numerically, the two outputs, the voltage and the input y_ϕ to the SOH model of the SPM can be solved analytically. The output voltage, namely the potential difference between the solid phase of the two electrodes, is obtained by solving (2.22) and (2.36). When the degradation is ignored, namely when $J_{sd,j} = 0$, $J_{total,j} = J_{1,j}$, and the voltage can be solved analytically as [54]

$$\begin{aligned} V &= \phi_{s,p}(0_p, t) - \phi_{s,n}(0_n, t) \\ &= U_{ref,p}(\theta_p) - U_{ref,n}(\theta_n) + \frac{RT}{\alpha F} \ln \left(\xi_p + \sqrt{\xi_p^2 + 1} \right) - \frac{RT}{\alpha F} \ln \left(\xi_n + \sqrt{\xi_n^2 + 1} \right) \\ &\quad - \frac{I}{AL_n a_{s,n}} R_{film} - \frac{I}{2A} \left(\frac{L_n}{\kappa_n^{eff}} + 2 \frac{L_{sep}}{\kappa_{sep}^{eff}} + \frac{L_p}{\kappa_p^{eff}} \right), \end{aligned} \quad (2.48)$$

where

$$\xi_j = \frac{J_{total,j}}{2a_{s,j}i_{0,j}}. \quad (2.49)$$

When the degradation is considered, the analytical solution needs to take the SOH model into account, and thus is presented in (2.73) in Section 2.3. Similarly as in the DFN model, the input y_ϕ is defined in the SOH model as (2.68).

The system above is a discrete system with a linear state equation and two non-linear outputs. With the same definition of the signals as in the DFN model, the state space model of the SPM is

$$x(k+1) = Ax(k) + Bu(k) + Fw(k), \quad (2.50)$$

$$y(k) = g(x(k), u(k), w(k)), \quad (2.51)$$

$$y_0(k) = g_0(x(k), u(k), w(k)), \quad (2.52)$$

where A , B , and F is obtained from (2.42) for both electrodes, $g(\cdot)$ represents (2.68), and $g_0(\cdot)$ represents (2.48) or (2.73) depending on whether the degradation is considered.

2.3 Battery SOH Model

The Arora model [31] is used to model the SOH subsystem in this work due to its ability to capture all electrochemical-based degradation mechanisms that consume cyclable Li-ions. The health model in [42, 43] adopted from [28] is an example of the Arora model used specifically for the SEI film formation mechanism. The form of the Arora model also provides insight on how to choose the form of the subsystem model in RCSI.

2.3.1 The Electrochemical Form

In the Arora model, each degradation mechanism is captured by the Butler-Volmer equation for the corresponding irreversible side reaction [31] (represented by the one-way arrow in Figure 2.1). The irreversibility of the side reactions leads to the consumption of cyclable Li-ions, causing capacity fade of the battery. The rate of the side reaction is captured with the side reaction current density $J_{sd,j}$. For LiFePO₄ batteries, degradation is assumed to happen only in the anode [28]. Hence, in the cathode,

$$J_{sd,p} = 0; \quad (2.53)$$

while in the anode,

$$J_{sd,n} = -i_{0,SD} a_{s,n} \exp\left(-\frac{\alpha_{c,n} F}{RT} \eta_{sd}\right), \quad (2.54)$$

where the overpotential η_{sd} can be obtained by

$$\eta_{sd} = \phi_{s,n} - \phi_{e,n} - U_{ref,SD} - \frac{J_{total,n}}{F} R_{film}, \quad (2.55)$$

where $J_{total,j}$ is the total current density, whose distribution is determined only by I , as shown in (2.18) - (2.20).

2.3.2 The Estimation Form

Since degradation is assumed to occur only in the anode [28], the side reaction current density in the cathode is always zero. Hence, the side reaction current density in only the anode, $J_{\text{sd},n}$, is considered and is represented with a shorter notation, J_{sd} .

The electrochemical equations of the SOH model can be simplified into a linear static equation with only one parameter and one input y_ϕ , which is computed in the SOC model. Substituting (2.55) into (2.54) yields

$$J_{\text{sd}} = K_{\text{SOH}} y_\phi, \quad (2.56)$$

where

$$K_{\text{SOH}} \triangleq -i_{0,\text{sd}} a_{\text{s},n} \exp\left(\frac{\alpha_{\text{c},n} F}{RT} U_{\text{ref},\text{sd}}\right), \quad (2.57)$$

$$y_\phi \triangleq \exp\left(-\frac{\alpha_{\text{c},n} F}{RT} \left(\phi_{\text{s},n} - \phi_{\text{e},n} - \frac{J_{\text{total},n}}{a_{\text{s},n}} R_{\text{film}}\right)\right). \quad (2.58)$$

Note that K_{SOH} is a function of the parameters of the battery model, among which $i_{0,\text{sd}}$ and $U_{\text{ref},\text{sd}}$ are associated with the SOH process.

One of the benefits of the linear static formulation of the SOH model is that under the presence of several side-reaction-based degradation mechanisms, the total side reaction current density can be easily obtained by summing all the side reaction current densities. Assume a total of κ side reactions happen simultaneously. Then each side reaction follows

$$J_{\text{sd},\iota} = K_{\text{SOH},\iota} y_\phi, \quad \iota = 1, \dots, \kappa, \quad (2.59)$$

where $J_{\text{sd},\iota}$ and $K_{\text{SOH},\iota}$ are the side reaction current density and the health parameter for the ι^{th} side reaction, respectively. Because the input y_ϕ is computed in the SOC model, all side reactions share the same y_ϕ . Therefore, the total side reaction current

density is

$$J_{\text{sd}} = \sum_{\iota=1}^{\kappa} J_{\text{sd},\iota} = \sum_{\iota=1}^{\kappa} K_{\text{SOH},\iota} y_{\phi} = K_{\text{SOH}} y_{\phi}, \quad (2.60)$$

where $K_{\text{SOH}} = \sum_{\iota=1}^{\kappa} K_{\text{SOH},\iota}$. Therefore, (2.60) is the counterpart of (2.56) when several side reactions are present.

For the DFN model that has multiple particles per electrode, the SOH model has the form

$$\mathcal{J}_{\text{sd}}(k) = \mathcal{K}_{\text{SOH}} \mathcal{Y}_{\phi}(k), \quad (2.61)$$

where the vectors $\mathcal{J}_{\text{sd}}(k)$ and $\mathcal{Y}_{\phi}(k)$ are constructed by stacking J_{sd} and y_{ϕ} for every particle in the anode. Assuming the anode contains N particles, \mathcal{J}_{sd} and \mathcal{Y}_{ϕ} are given by

$$\mathcal{J}_{\text{sd}} \triangleq \begin{bmatrix} J_{\text{sd}}^1 \\ \vdots \\ J_{\text{sd}}^N \end{bmatrix}, \quad \mathcal{Y}_{\phi} \triangleq \begin{bmatrix} y_{\phi}^1 \\ \vdots \\ y_{\phi}^N \end{bmatrix}. \quad (2.62)$$

The gain \mathcal{K}_{SOH} is the diagonal matrix

$$\mathcal{K}_{\text{SOH}} \triangleq \begin{bmatrix} K_{\text{SOH}}^1 & & & \\ & \ddots & & \\ & & K_{\text{SOH}}^N & \end{bmatrix}, \quad (2.63)$$

where the superscripts $1, \dots, N$ in (2.62) and (2.63) are the particle indices.

If $K_{\text{SOH}}^1 = \dots = K_{\text{SOH}}^N \triangleq K_{\text{SOH}}^{\text{unif}}$, then \mathcal{K}_{SOH} can be reduced to the scalar gain $K_{\text{SOH}}^{\text{unif}}$. In this case, there is no need to differentiate the degradation processes in different particles, and the SOH model can be simplified from (2.61) to

$$J_{\text{sd}}^{\text{ave}} = K_{\text{SOH}}^{\text{unif}} y_{\phi}^{\text{ave}}, \quad (2.64)$$

where

$$J_{\text{sd}}^{\text{ave}} \triangleq \frac{1}{N} \sum_{m=1}^N J_{\text{sd}}^m, \quad y_{\phi}^{\text{ave}} \triangleq \frac{1}{N} \sum_{m=1}^N y_{\phi}^m. \quad (2.65)$$

In (2.64), the average of the side reaction current densities among all particles is used instead of \mathcal{J}_{sd} to represent the total degradation rate of the battery.

For the SPM, $N = 1$ in (2.62), and thus (2.56), (2.61), and (2.64) are the same. For consistency, the SOH model is expressed using (2.56) when integrated with the SPM.

Furthermore, for the SPM integrated with the SOH model, both the voltage, $J_{\text{sd}}^{\text{ave}}$, and y_{ϕ}^{ave} can be solved analytically. Define $d\phi_n \triangleq \phi_{\text{s},n} - \phi_{\text{e},n} - \frac{J_{\text{total},n}}{a_{\text{s},n}} R_{\text{film}}$. Substituting (2.25) and (2.24) into (2.22) yields

$$J_{1,n} = \frac{a_{\text{s},n} i_{0,n}}{\exp\left(\frac{\alpha F}{RT} U_{\text{ref},n}\right)} \frac{1}{\exp\left(-\frac{\alpha F}{RT} d\phi_n\right)} - a_{\text{s},n} i_{0,n} \exp\left(\frac{\alpha F}{RT} U_{\text{ref},n}\right) \exp\left(-\frac{\alpha F}{RT} d\phi_n\right). \quad (2.66)$$

Similarly, (2.54) can be written as

$$J_{\text{sd}} = -i_{0,\text{sd}} a_{\text{s},n} \exp\left(\frac{\alpha F}{RT} U_{\text{ref},\text{sd}}\right) \exp\left(-\frac{\alpha F}{RT} d\phi_n\right). \quad (2.67)$$

Solving (2.66) and (2.67) yields

$$y_{\phi} = \exp\left(-\frac{\alpha F}{RT} d\phi_n\right) = \frac{k_4 - \sqrt{k_4^2 - 4k_1(k_2 + k_3)}}{2(k_2 + k_3)}, \quad (2.68)$$

where

$$k_1 = \frac{a_{s,n} i_{0,n}}{\exp\left(\frac{\alpha F}{RT} U_{ref,n}\right)}, \quad (2.69)$$

$$k_2 = -a_{s,n} i_{0,n} \exp\left(\frac{\alpha F}{RT} U_{ref,n}\right), \quad (2.70)$$

$$k_3 = -i_{0,sd} a_{s,n} \exp\left(\frac{\alpha F}{RT} U_{ref,sd}\right), \quad (2.71)$$

$$k_4 = J_{total,n}. \quad (2.72)$$

$k_1 - k_4$ are all functions of signals available from the SOC model or the parameters of the SOC and SOH models. Then, the voltage is

$$\begin{aligned} V &= \phi_{s,p}(0_p, t) - \phi_{s,n}(0_n, t) \\ &= U_{ref,p}(\theta_p) + \frac{RT}{\alpha F} \ln\left(\xi_p + \sqrt{\xi_p^2 + 1}\right) + d\phi_n - \frac{I}{AL_n a_{s,n}} R_{film} \\ &\quad - \frac{I}{2A} \left(\frac{L_n}{\kappa_n^{eff}} + 2 \frac{L_{sep}}{\kappa_{sep}^{eff}} + \frac{L_p}{\kappa_p^{eff}} \right). \end{aligned} \quad (2.73)$$

where

$$d\phi_n = -\frac{RT}{\alpha F} \ln(y_\phi). \quad (2.74)$$

Finally, J_{sd} is available by substituting (2.68) in (2.56).

The SOH model is a linear static equation in the form of (2.56), (2.61), or (2.64). (2.56), (2.61), and (2.64) can all be written as

$$u = \theta^T \phi, \quad (2.75)$$

where u , θ and ϕ represent \mathcal{J}_{sd} , \mathcal{K}_{SOH} and \mathcal{Y}_ϕ in (2.61), or J_{sd}^{ave} , K_{SOH}^{unif} and y_ϕ^{ave} in (2.64).

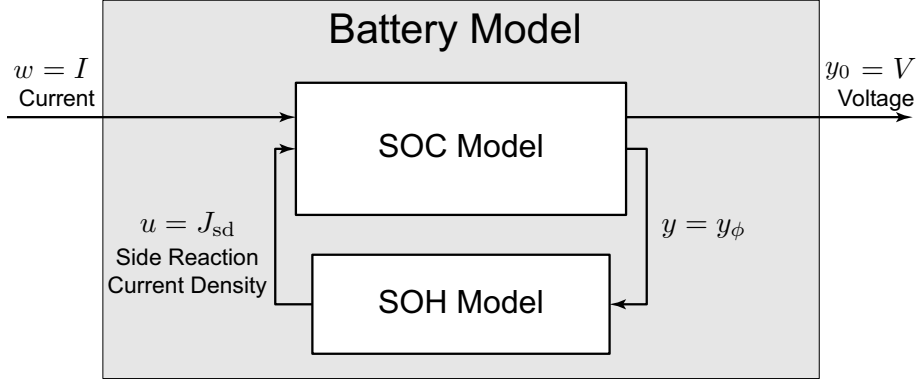


Figure 2.3: The architecture of the battery model.

2.4 Combining SOC Model and SOH Model

Figure 2.3 shows the combined battery model that contains both the SOC and SOH models. The SOC and SOH models are connected in a feedback form. The signals in Figure 2.3 are defined as follows: i) the measurable input w and output y_0 of the overall model are the current I and the voltage V , respectively; ii) the output of the SOH model u is the side reaction current density J_{sd} ; and iii) the input y to the SOH model is y_ϕ . Notice that the SOC model and the SOH model interact with each other through the signals u and y .

2.5 Summary and Conclusions

This chapter presents three widely used electrochemical battery models in the literature. The three models are partitioned into i) the SOC models, which include the DFN model [51, 52] and its simplification, the SPM [56, 54], and ii) the SOH model, which is the Arora model herein [31]. For each of the models, the electrochemical form is first presented, followed by the simplifications and modifications made to the models that yield forms suitable for estimation.

Even though these models are obtained from the literature, two modifications presented herein are original. First, the Arora model is modified to one linear static equation with all parameters lumped into one. This formulation provides a simple representation of the complicated SOH process, which in turn simplifies the design

of the identification algorithm and facilitates the accurate identification of the SOH subsystem. The linearity of the subsystem model also allows easy combination of several degradation mechanisms. Second, this chapter provides an analytical solution of the current densities in the SPM integrated with the Arora model. These two modifications are developed in this work to facilitate the estimation of the side reaction current density in Chapter 3 and 4.

Chapter 3

Estimation of Side Reaction Current Density

3.1 Introduction

In this chapter, the side reaction current density is estimated as the SOH indicator. The side reaction current density is a measure of the rate of cyclable Li-ion consumption, which contributes to capacity fade in all electrochemical-based degradation mechanisms that consume cyclable Li-ions [31].

Although the side reaction current density is known to be associated with the degradation process [31, 28], it has not been used to directly indicate the battery health in battery management applications. This chapter argues that the side reaction current density is a logical choice as a direct SOH indicator in various situations because the side reaction current density provides information regarding both the degradation rate and the overall degradation level through its integral. In situations where the instantaneous degradation rate is concerned, for example where controllers are designed with avoiding a dramatic degradation rate as an objective or constraint [7], the side reaction current density provides the direct measure of the degradation rate. In situations where the overall degradation level over time is concerned, such as the estimation of remaining mileages of EV batteries, the integral of the side reaction current density across the whole battery and over time provides the total loss

in cyclable Li-ions, which is an electrochemical measure of the capacity loss. For degradation mechanisms that result in byproducts such as SEI film, the aforementioned integral is also proportional to the growth in internal resistance. Therefore, this chapter proposes the idea of using the side reaction current density as a direct indicator of the SOH, and provides a method to estimate the side reaction current density directly.

Compared to the other electrochemical SOH indicators [41, 42, 43], the side reaction current density has two advantages. First, the side reaction current density measures the rate of Li-ion consumption, thus giving an instantaneous sense of how fast a battery is degrading at each instant in time. Secondly, as opposed to the SEI film resistance and Lithium deposition, which are mechanism-specific indicators that apply only to the degradation mechanism of SEI film formation and Lithium plating, respectively, the side reaction current density can be applied to all Li-ion-consuming degradation mechanisms [31].

A major challenge of estimating the side reaction current density is that it is not directly measurable in-situ. This dissertation addresses this challenge by treating the battery health system as an inaccessible subsystem of the overall battery system, and using retrospective-cost subsystem identification (RCSI) [57, 58, 59, 60] to identify this subsystem and estimate its output, namely, the side reaction current density.

In this chapter, the estimation of the side reaction current density is primarily simulated using a parameter set for a LiFePO₄ battery as an example. The proposed estimation technique, including the method for estimating the side reaction current density using RCSI and the framework analyzing its robustness, can also be applied to other parameter sets and other battery chemistries to monitor the SOH change resulting from any electrochemical-based degradation mechanism that consumes cyclable Li-ions. To show the applicability of the estimation technique to other types of Li-ion battery chemistries with different parameters, the same technique is later applied to a few example cases using a parameter set for an LMO-mixture battery.

This chapter focuses on the following research questions:

1. Can the side reactions that consume cyclable Li-ions and thus degrade battery

health be formulated as an inaccessible subsystem in the battery?

2. Is it possible to estimate the side reaction current density as the output of the inaccessible subsystem using RCSI?
3. How robust is this estimation against various non-ideal conditions?

3.2 Retrospective-Cost Subsystem Identification

3.2.1 Problem Setup

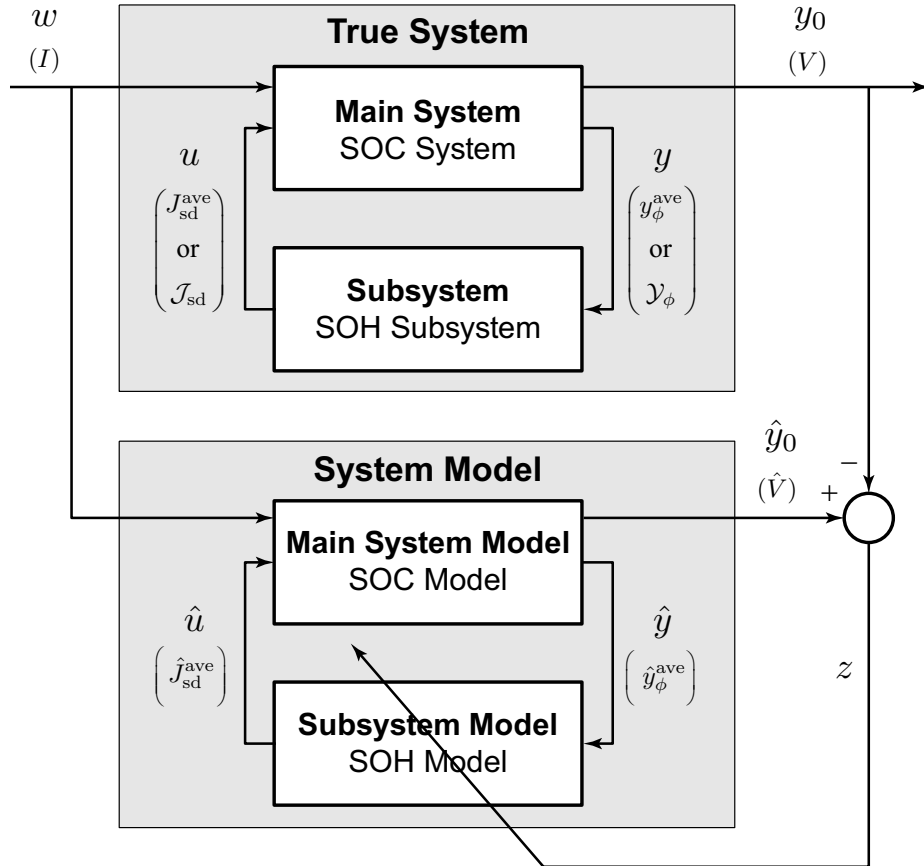


Figure 3.1: The architecture of retrospective-cost subsystem identification for estimation of the side reaction current density. Note that the output of the SOH model is the side reaction current density J_{sd} .

Figure 3.1 presents the architecture of RCSI formulated for the proposed battery health estimation problem. The true system in the upper block contains a known main

system and an unknown subsystem. The subsystem output, u , is the inaccessible signal to be estimated. This representation of the true system has the same architecture as the battery model in Figure 2.3. The lower block, labelled “system model”, is the model of the true system. The main system model is based on knowledge of the main system. The form of the subsystem model is assumed to be a mathematical approximation of the form of the true subsystem. The difference between the output of the true system and the system model is computed to identify the subsystem model parameter and thus estimate the subsystem output, the inaccessible signal of interest.

In the context of the battery health estimation problem, the true system is a battery, where the main system represents the battery SOC system, which is assumed to be known, and the unknown subsystem represents the battery SOH system to be identified. For the simulation study presented herein, the true system is represented by the battery model. The main system is the SOC model represented by (2.32) – (2.34), while the subsystem is the SOH model represented by (2.75), where θ is assumed to be unknown.

Similarly, the system model is the battery model, where the main system model is the SOC model and the subsystem model is the SOH model. The SOC model in the main system model has the form

$$\hat{x}(k+1) = \hat{f}(\hat{x}(k), \hat{u}(k), w(k)), \quad (3.1)$$

$$\hat{y}(k) = \hat{g}(\hat{x}(k), \hat{u}(k), w(k)), \quad (3.2)$$

$$\hat{y}_0(k) = \hat{g}_0(\hat{x}(k), \hat{u}(k), w(k)). \quad (3.3)$$

If accurate knowledge of the main system is assumed, then the number of particles per electrode, which determines the number of states in (2.32) – (2.34), and the parameters in the main system model are identical to those of the main system. In this case, $\hat{f}(\cdot)$ and $f(\cdot)$, $\hat{g}(\cdot)$ and $g(\cdot)$, and $\hat{g}_0(\cdot)$ and $g_0(\cdot)$ are identical. When modeling error between the main system model and the main system is considered, $\hat{f}(\cdot)$ and $f(\cdot)$, $\hat{g}(\cdot)$ and $g(\cdot)$, and $\hat{g}_0(\cdot)$ and $g_0(\cdot)$ are not identical.

For simplification in estimation, the SOH parameters for all of the particles in the

subsystem model are assumed to be identical; thus the form of the subsystem model is assumed to be a linear static equation as (2.64),

$$\hat{J}_{\text{sd}}^{\text{ave}} = \hat{K}_{\text{SOH}}^{\text{unif}} \hat{y}_{\phi}^{\text{ave}}, \quad (3.4)$$

where $\hat{J}_{\text{sd}}^{\text{ave}}$ and $\hat{y}_{\phi}^{\text{ave}}$ are the estimates of the average of \mathcal{J}_{sd} and \mathcal{Y}_{ϕ} , respectively; and $\hat{K}_{\text{SOH}}^{\text{unif}}$ is an estimate of the average of \mathcal{K}_{SOH} weighted by the subsystem input in each particle. When the SOH parameters are assumed identical for all of the particles in the true subsystem as well, that is, K_{SOH}^m are identical and (2.64) is used to represent the true SOH system, $\hat{J}_{\text{sd}}^{\text{ave}}$, $\hat{K}_{\text{SOH}}^{\text{unif}}$ and $\hat{y}_{\phi}^{\text{ave}}$ are the estimates of $J_{\text{sd}}^{\text{ave}}$, $K_{\text{SOH}}^{\text{unif}}$ and y_{ϕ}^{ave} .

Define the output and input of the subsystem model as

$$\hat{u} \triangleq \hat{J}_{\text{sd}}^{\text{ave}}, \quad (3.5)$$

$$\hat{y} \triangleq \hat{y}_{\phi}^{\text{ave}}. \quad (3.6)$$

Then the subsystem model can be expressed in the ARMAX form

$$\hat{u}(k) = \hat{\theta}^T(k) \hat{y}(k), \quad (3.7)$$

where $\hat{\theta}(k) \in \mathbb{R}^{l_u \times l_y}$ is the parameter of the subsystem model,

$$\hat{\theta}(k) \triangleq \hat{K}_{\text{SOH}}^{\text{unif}}(k), \quad (3.8)$$

where l_u and l_y are the dimension of \hat{u} and \hat{y} , respectively. Here $\hat{\theta}$ and $\hat{\phi}$ are both scalars, and thus $l_u = 1$ and $l_y = 1$.

3.2.2 Algorithm Development

RCSI is developed under the assumption that both the main system and the subsystem are in discrete-time linear form. However, with a proper choice of parameters, the algorithm can also be applied to discrete-time nonlinear systems [59, 42, 43]. In this section, the development of RCSI is presented in the linear context with guidelines

to choose the parameters in nonlinear applications.

A two-stage Kalman-filter version of RCSI is presented in this section, which is a variation of [59, 61, 42, 43]. This version of RCSI operates recursively, where each time step contains two stages. In the first stage, the estimates of the inaccessible signal u in past time steps are constructed from the difference between the measurable signal y_0 and its estimate \hat{y}_0 using knowledge of the main system. These constructed estimates of u in the past time steps are referred to as retrospective-cost signals, and this stage is called retrospective-cost-based signal construction. Although the full model of the main system is assumed available, only the Markov parameters of this model are used in the signal construction, which simplifies the algorithm. In the second stage, the subsystem parameter is identified with the constructed estimates of u in past time steps using the Kalman filter. This identified subsystem parameter is then used in the subsystem model to generate \hat{u} as a prediction of u in the next time step. These two stages are described next in detail.

3.2.2.1 Retrospective-Cost-Based Signal Construction

The main system is assumed to be linear and discrete-time with the form

$$x(k+1) = Ax(k) + Bu(k) + Fw(k), \quad (3.9)$$

$$y(k) = Cx(k) + Du(k) + Jw(k), \quad (3.10)$$

$$y_0(k) = E_1x(k) + E_2u(k) + E_3w(k), \quad (3.11)$$

where $x(k) \in \mathbb{R}^n$ is the state, $w(k) \in \mathbb{R}^{l_w}$ is the external input, $u(k) \in \mathbb{R}^{l_u}$ is the output of the subsystem, $y(k) \in \mathbb{R}^{l_y}$ is the input to the subsystem, and $y_0(k) \in \mathbb{R}^{l_{y_0}}$ is the measurable output.

The main system is assumed known, and thus the model of the main system is

constructed as

$$\hat{x}(k+1) = \hat{A}\hat{x}(k) + \hat{B}\hat{u}(k) + \hat{F}w(k), \quad (3.12)$$

$$\hat{y}(k) = \hat{C}\hat{x}(k) + \hat{D}\hat{u}(k) + \hat{J}w(k), \quad (3.13)$$

$$\hat{y}_0(k) = \hat{E}_1\hat{x}(k) + \hat{E}_2\hat{u}(k) + \hat{E}_3w(k), \quad (3.14)$$

$$z(k) = \hat{y}_0(k) - y_0(k), \quad (3.15)$$

where $\hat{x}(k) \in \mathbb{R}^n$, $\hat{y}(k) \in \mathbb{R}^{l_y}$, $z(k) \in \mathbb{R}^{l_z}$, $\hat{y}_0(k) \in \mathbb{R}^{l_{y_0}}$, $\hat{u}(k) \in \mathbb{R}^{l_u}$. The known information of the main system is reflected through matrices $\hat{A}, \dots, \hat{E}_3$. If there is no modeling error in the main system model, then $\hat{A}, \dots, \hat{E}_3$ are identical to A, \dots, E_3 , respectively. For nonlinear systems such as (2.32) – (2.34), the linear equations (3.9), (3.10) and (3.11) are specializations of (2.32), (2.33) and (2.34), respectively. Similarly, (3.12), (3.13) and (3.14) are specializations of (3.1) (3.2) and (3.3), respectively.

The main system model relates the subsystem model output \hat{u} to the estimated output signal \hat{y}_0 using the Markov parameters between \hat{u} and \hat{y}_0 , which are defined as

$$\hat{H}_i \triangleq \begin{cases} \hat{E}_2, & i = 0 \\ \hat{E}_1\hat{A}^{i-1}\hat{B}, & i \geq 1 \end{cases}. \quad (3.16)$$

Markov parameters reflect the impact of the past input \hat{u} on the current output \hat{y}_0 as in

$$\begin{aligned} \hat{y}_0(k) &= \hat{E}_1\hat{A}^k\hat{x}(0) + \hat{E}_3w(k) + \sum_{i=0}^{k-1} \hat{E}_1\hat{A}^i\hat{F}w(k-i-1) \\ &\quad + \sum_{i=0}^k \hat{H}_i\hat{u}(k-i). \end{aligned} \quad (3.17)$$

For nonlinear systems, the Markov parameters serve as tunable parameters in the algorithm, which also reflects the influence of $\hat{u}(k-i)$ on $\hat{y}_0(k)$. One way to tune \hat{H}_i for nonlinear applications is to linearize the system around an operating point and use the linearization to determine \hat{H}_i .

A set of dominant Markov parameters is defined that corresponds to the set of $\hat{u}(k - i)$ that has the largest impact on the output $\hat{y}_0(k)$. The dominant Markov parameters and the corresponding $\hat{u}(k - i)$ can be put into the matrix form

$$\mathcal{H} \triangleq \begin{bmatrix} H_{i_0} & \cdots & H_{i_r} \end{bmatrix} \in \mathbb{R}^{l_z \times r l_u}, \quad (3.18)$$

$$U(k - 1) \triangleq [\hat{u}^T(k - i_0) \cdots \hat{u}^T(k - i_r)]^T, \quad (3.19)$$

where r is a positive integer indicating the size of the set of dominant Markov parameters, and i_0, \dots, i_r are indices of the dominant Markov parameters.

Combining (3.15), (3.17), (3.18) and (3.19) yields

$$z(k) = \mathcal{S}(k) + \mathcal{H}U(k - 1), \quad (3.20)$$

where

$$\begin{aligned} \mathcal{S}(k) \triangleq & \hat{E}_1 \hat{A}^k \hat{x}(0) + \hat{E}_3 w(k) + \sum_{i=0}^{k-1} \hat{E}_1 \hat{A}^i \hat{F} w(k - i - 1) \\ & - y_0(k) + \mathcal{H}' U'(k - 1). \end{aligned} \quad (3.21)$$

\mathcal{H}' is the matrix containing all the Markov parameters H_i except the dominant ones and $U'(k - 1)$ is the matrix containing the $u(k - i)$ corresponding to the entries in \mathcal{H}' .

To utilize the information from several time steps, (3.20) can be rewritten with a delay of k_j time steps in the form

$$z(k - k_j) = \mathcal{S}_j(k - k_j) + \mathcal{H}_j U_j(k - k_j - 1), \quad (3.22)$$

where $0 \leq j \leq s$ and $0 \leq k_1 < k_2 < \dots < k_s$. Notice that the dominant Markov parameters can be different for different steps, i.e., \mathcal{H}_j is not a constant with respect

to j . The extended performance is defined by stacking $z(k - k_1), \dots, z(k - k_s)$ into

$$Z(k) \triangleq [z^T(k - k_1) \ \dots \ z^T(k - k_s)]^T \in \mathbb{R}^{sl_z}. \quad (3.23)$$

Therefore,

$$Z(k) \triangleq \tilde{\mathcal{S}}(k) + \tilde{\mathcal{H}}\tilde{U}(k-1), \quad (3.24)$$

where

$$\tilde{\mathcal{S}}(k) \triangleq [\mathcal{S}(k - k_1) \ \dots \ \mathcal{S}(k - k_s)]^T \in \mathbb{R}^{sl_z}, \quad (3.25)$$

$\tilde{\mathcal{H}} \in \mathbb{R}^{sl_z \times l_{\tilde{U}}}$, and $\tilde{U}(k-1) \in \mathbb{R}^{l_{\tilde{U}}}$. $\tilde{U}(k-1)$ is formed by stacking $U_1(k - k_1 - 1), \dots, U_s(k - k_s - 1)$ and removing repetitions in the components. $\tilde{\mathcal{H}}$ consists of the entries of $\mathcal{H}_1, \dots, \mathcal{H}_s$ arranged according to the structure of $\tilde{U}(k-1)$.

The extended retrospective performance is defined by

$$Z^*(k) \triangleq Z(k) - \tilde{\mathcal{H}}\tilde{U}(k-1) + \tilde{\mathcal{H}}\tilde{U}^*(k-1), \quad (3.26)$$

where the actual past outputs $\tilde{U}(k-1)$ of the subsystem model in (3.24) are replaced by the retrospectively optimized subsystem outputs $\tilde{U}^*(k-1)$. Since the retrospective subsystem outputs serve as estimates of the true subsystem outputs in corresponding past steps, replacing $\tilde{U}(k-1)$ with $\tilde{U}^*(k-1)$ is expected to yield the smallest extended retrospective performance at the past steps. Therefore, the retrospective subsystem outputs can be found by minimizing the retrospective cost function defined as

$$\begin{aligned} \bar{J}(k) &\triangleq Z^{*\top}(k)R_Z(k)Z^*(k) \\ &\quad + \tilde{U}^{*\top}(k-1)R_U(k)\tilde{U}^*(k-1), \end{aligned} \quad (3.27)$$

where $R_Z(k) \in \mathbb{R}^{l_z \times l_z}$ and $R_U(k) \in \mathbb{R}^{l_u \times l_u}$ are positive-definite weightings. In (3.27), $\tilde{U}^{*\top}(k)R_U(k)\tilde{U}^*(k)$ is the regularization term, which is included in $\bar{J}(k)$ to ensure

that $\mathcal{A}(k)$ is invertible.

The unique global minimizer of (3.27) is

$$\tilde{U}^*(k-1) = -\frac{1}{2}\mathcal{A}^{-1}(k)\mathcal{B}(k), \quad (3.28)$$

where

$$\mathcal{A}(k) \triangleq \tilde{\mathcal{H}}^T R_Z(k) \tilde{\mathcal{H}} + R_U(k), \quad (3.29)$$

$$\mathcal{B}(k) \triangleq 2\tilde{\mathcal{H}}^T R_Z(k)[Z(k) - \tilde{\mathcal{H}}\tilde{U}(k-1)]. \quad (3.30)$$

3.2.2.2 Kalman Filter Update of the Subsystem Parameter

Denote the component in $\tilde{U}^*(j-1)$ that estimates $u(k)$, where $k \leq j$, with $\tilde{u}^*(k)$. By replacing $\hat{u}(k)$ in (2.61) with $\tilde{u}^*(k)$, identification of the subsystem becomes identification of the parameters in the ARMAX model

$$\tilde{u}^*(k) = \hat{\theta}^T(k)\hat{y}(k), \quad (3.31)$$

where $\hat{\theta}(k)$ is defined in (3.8). If there are multiple choices of j such that $\tilde{U}^*(j-1)$ contains a component that estimates $u(k)$, then the selection of $\tilde{u}^*(k)$ is chosen to be the latest estimate.

The Kalman filter updating law for the ARMAX model parameters is

$$\begin{aligned} \hat{\theta}(k+1) &= [1 - a(k)][\hat{\theta}(k) + (P(k+1) + Q)\hat{y}(k+1)] \\ &\quad [R_k + \hat{y}(k+1)^T(P(k+1) + Q)\hat{y}(k+1)]^{-1} \\ &\quad (u^*(k+1) - \hat{y}(k+1)\hat{\theta}(k)) + a(k)\hat{\theta}(0). \end{aligned} \quad (3.32)$$

The error covariance P is updated by

$$\begin{aligned} P(k+1) = & [1 - a(k)][(P(k) + Q) - (P(k) + Q) \\ & (R_k + \hat{y}(k+1)(P(k) + Q)\hat{y}^T(k+1))^{-1} + R_1] \\ & + a(k)P(0), \end{aligned} \quad (3.33)$$

where Q , R_k and R_1 are the pre-set parameters. $a(k) \in \{0, 1\}$ is an algorithm reset, that is, $\theta(k)$ and $P(k)$ are reset to their initial values when $a(k) = 1$, otherwise $a(k) = 0$. The error covariance matrix is initialized as $P(0) = \beta I$, where $\beta > 0$.

3.3 Simulation Results under Ideal Conditions

This section presents simulation results of RCSI-based estimation of the side reaction current density under ideal conditions. The ideal conditions refer to the following conditions: i) measurements of the input current and the output voltage contain no noise; ii) exact knowledge of the battery SOC is assumed, and thus the initial SOC in the true system and the system model are set to be exactly the same; and iii) no modeling error exists in both the main system model and the subsystem model.

The simulation results are obtained using two types of excitation signals. The first type is the constant current charge and discharge (CCCD) cycles. In every cycle, the battery model operates under the constant current charge (CCC) mode followed immediately by the constant current discharge (CCD) mode. The mode switches from CCD to CCC when the voltage reaches 2.0 V and from CCC to CCD at 3.6 V. Since the charge and discharge current for EVs is below 10 C, 1-C and 10-C CCCD cycles are chosen to test the slow and fast charge/discharge cases, respectively [32]. For both cases, the SOC is initialized at 0%. Constant voltage modes are not included because the battery degradation is insignificant during constant voltage modes, which results in the unidentifiability of the SOH indicator [42, 43].

The second type of excitation signals is the current profile generated from an EV following the Urban Dynamometer Driving Schedule (UDDS). This current profile

evaluates the effectiveness of the algorithm under dynamic battery loading conditions typical for EV applications. The UDDS current profile presented herein is generated by the Advisor software [62] with the default EV settings. The Li-ion battery in Advisor has a capacity of 7 Ah, while the rated capacity of the battery model herein is 2.5 Ah. Therefore, the current magnitude is scaled down to match the C rates and ensure that the battery is not overdischarged. The initial battery voltage is set to 3.6 V.

The parameters of the SOC model are adopted from [63, 64], where the parameters are identified from the cycling data of commercial LiFePO₄ batteries. The parameters of the SOH model are adopted from [28]. The number of particles in each electrode is obtained by increasing the number starting from 10 at increments of 10 until a further increment yields a voltage response difference less than 5 mV for the 10-C CCC mode. The number of particles is selected to be 50 per electrode. A sampling time of 0.2 s is chosen because the chemical reaction has slow dynamics. The results below also confirm that this sampling rate is fast enough to achieve accurate simulation and estimation.

For RCSI, the weights in the retrospective cost function (3.27) are set as $R_U = 0$ and $R_Z = 1$, and the parameters for Kalman filter update (3.32) and (3.33) are set as $Q = 0.1$, $R_k = 0.5$, and $R_1 = 0$. The parameter estimate and error covariance matrix are initialized at $\theta(0) = 0$ and $P(0) = 100$, respectively. The Markov parameter is set as $\tilde{\mathcal{H}} = H_0 = 2 \times 10^{-7} \Omega \text{ m}^3$.

The performance of RCSI is determined by the relative estimation errors of the side reaction current density and the subsystem parameter defined as

$$\epsilon_{J_{\text{sd}}} \triangleq \frac{J_{\text{sd}} - \hat{J}_{\text{sd}}}{J_{\text{sd}}}, \quad (3.34)$$

$$\epsilon_\theta \triangleq \frac{\theta - \hat{\theta}}{\theta}, \quad (3.35)$$

where J_{sd} and \hat{J}_{sd} are the true and estimated values of the side reaction current density, respectively; θ and $\hat{\theta}$ are the true and estimated values of the subsystem parameter, respectively.

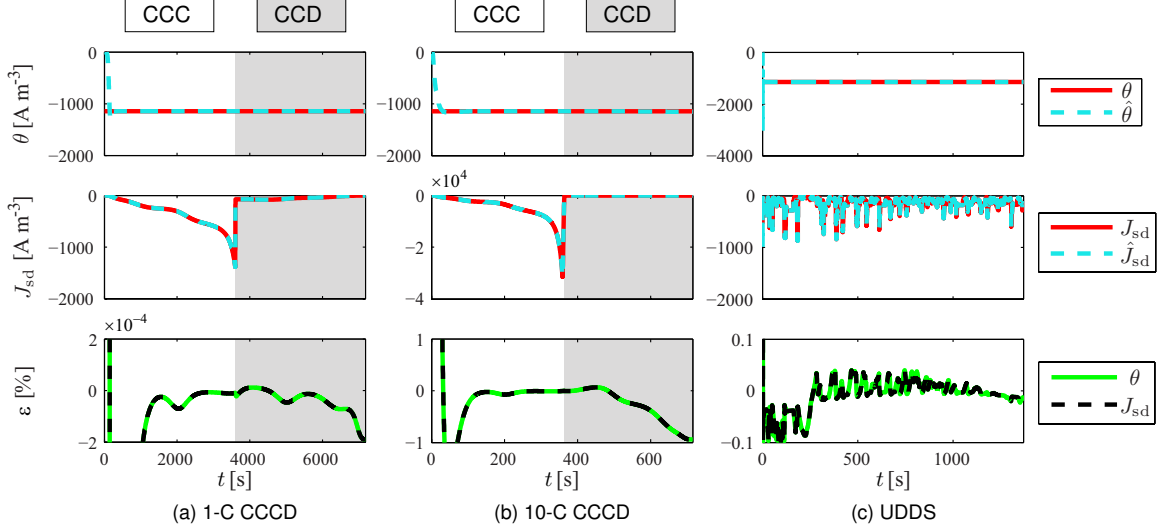


Figure 3.2: The estimates and relative estimation errors ϵ of the subsystem parameter θ and the side reaction current density J_{sd} under ideal conditions with three input currents: (a) a 1-C constant current charge and discharge (CCCD) cycle, (b) a 10-C CCCD cycle, and (c) a simulated current profile generated by an EV following an Urban Dynamometer Driving Schedule (UDDS).

To begin with, it is assumed that no discrepancy exists between the forms of the subsystem and subsystem model. Therefore, the SOH parameters K_{SOH}^m are set identical among all anode particles in the subsystem, and the form of the subsystem also follows (2.64). In this case, the variables to be estimated are K_{SOH}^{unif} and J_{sd}^{ave} , whose estimates are $\hat{K}_{SOH}^{\text{unif}}$ and $\hat{J}_{sd}^{\text{ave}}$, respectively. Therefore, the variables in (3.34) and (3.35) are named as follows,

$$J_{sd} = J_{sd}^{\text{ave}}, \quad \hat{J}_{sd} = \hat{J}_{sd}^{\text{ave}}, \quad (3.36)$$

$$\theta = K_{SOH}^{\text{unif}}, \quad \hat{\theta} = \hat{K}_{SOH}^{\text{unif}}, \quad (3.37)$$

$$y = y_{\phi}^{\text{ave}}, \quad \hat{y} = \hat{y}_{\phi}^{\text{ave}}. \quad (3.38)$$

3.3.1 Constant Current Charge and Discharge Cycles

Figure 3.2 (a) shows the estimates obtained with one 1-C CCCD cycle. The estimated parameter $\hat{\theta}$ converges to the true parameter θ in less than 1000 s after initialization at zero. Meanwhile, the estimated side reaction current density also converges to the

true value. The relative estimation errors $\epsilon_{J_{\text{sd}}}$ and ϵ_θ are bounded within $\pm 2 \times 10^{-4}\%$ after the transient phase.

Figure 3.2 (b) presents the estimates obtained with one 10-C CCCD cycle. The estimates of the subsystem parameter and the side reaction current density converge to their true values in less than 100 s. The relative estimation errors are bounded within $\pm 1\%$ after the transient phase.

The relative estimation errors show that the estimates diverge from their true values during the discharge mode. This divergence is due to the fact that the side reaction current density is near zero during the discharge mode, which is consistent with the assumption in [28] that the degradation is negligible during discharge. As a result, the impact of the subsystem output on the output voltage is negligible; hence the identifiability of the subsystem parameter is weak. The divergence is more evident under the 10-C discharge rate, because the side reaction current density is smaller under the higher discharge C rate. During the 1-C discharge mode, the side reaction current density is on the order of 100 A/m^3 , while it is on the order of 10 A/m^3 during the 10-C discharge mode. This divergence agrees with the conclusions in [42, 43, 65].

It can be concluded from Figure 3.2 (a) and Figure 3.2 (b) that accurate estimates of the side reaction current density and health subsystem parameter can be obtained in both slow (1-C) and fast (10-C) constant current charge modes under ideal conditions. However, during the discharge modes, the estimates slowly diverge from their true values, due to the weak identifiability caused by the negligible side reaction current density.

3.3.2 The Urban Dynamometer Driving Schedule Test Cycles

Figure 3.2 (c) shows the parameter estimates with the UDDS current profile. With $\hat{\theta}(0) = 0$, the parameter estimate $\hat{\theta}$ converges to the true parameter θ within 10 s. The estimate of the side reaction current density can also track the true value throughout the cycle. The relative estimation errors of both the side reaction current density and the subsystem parameter are bounded within $\pm 0.1\%$ after the transient phase. This result suggests that RCSI can estimate both the side reaction current density

and the subsystem parameter effectively under the dynamic operating condition of EVs under ideal conditions. The estimation errors show fluctuations when the true side reaction current density is small and the degradation is negligible, which agrees with the results in Section 3.3.1. The relative estimation errors also diverge at the end of the UDDS cycle. This divergence is due to the decrease of the battery SOC throughout the UDDS cycle except several brief moments of charging by regenerative braking. The SOC level drops to only 14% by the end of the cycle. The true side reaction current density is small when the battery SOC is low, which also leads to the weak identifiability.

In Figure 3.2, the relative estimation errors in the side reaction current density and the health subsystem parameter are similar. On the one hand, x and \hat{x} are close under ideal conditions. On the other hand, it can also be observed from Figure 3.2 that convergence of the estimated side reaction current density is fast, so that \hat{u} and u are close after the transient phase. Then, according to (2.33) and (3.2), \hat{y} and y are close when both x and \hat{x} , and u and \hat{u} are close. Therefore,

$$\epsilon_{J_{sd}} = \frac{\theta y - \hat{\theta} \hat{y}}{\theta y} \approx \frac{\theta y - \hat{\theta} y}{\theta y} = \frac{\theta - \hat{\theta}}{\theta} = \epsilon_\theta. \quad (3.39)$$

Note that (3.39) holds as long as $\hat{y}(k) \approx y(k)$. Hence, (3.39) may be true, even without assuming the ideal conditions, when the differences between y and \hat{y} caused by the discrepancies between x and \hat{x} , and J_{sd} and \hat{J}_{sd} are small. However, if there is large measurement noise, or state or modeling errors that lead to a large difference between y and \hat{y} , the relative estimation errors in the side reaction current density and the health subsystem parameter may be different.

3.4 Robustness to Non-Ideal Conditions

In this section, robustness of the algorithm to non-ideal conditions is examined. First, it is shown that the voltage difference between the true system and the system model caused by non-ideal conditions (e.g., measurement noise, SOC estimation errors, main

system modeling errors, and form discrepancy between the subsystem and the sub-system model) degrades the performance of the algorithm. Then, robustness against measurement noise, SOC estimation errors and modeling errors are examined in Section 3.4.2, 3.4.3 and 3.4.4, respectively. Discussions of the simulation results are given next. Expectations about the performance of RCSI in practice based on the analysis of the simulation results are highlighted.

3.4.1 The Relationship between the Estimation Accuracy and Voltage Errors

It can be observed from (3.27) that the goal of RCSI is to drive the optimal voltage difference, which corresponds to $Z^*(k)$ in (3.26), to zero, assuming that this zero voltage difference indicates that the optimal subsystem output $\tilde{U}^*(k - 1)$ is identical to the true subsystem output. This assumption is not valid in the presence of a voltage difference caused by additional sources.

The impact of the side reaction current density on the output voltage is mainly through the intercalation reaction, and is manifested as an instantaneous impact. Because this instantaneous impact is small, the SOH estimation is sensitive to non-ideal conditions that cause errors in the voltage. These non-ideal conditions are the additional sources that cause an additional voltage difference, and this additional voltage difference is denoted by V_{as} .

Assuming (3.24) is corrected with V_{as} , it follows that

$$Z(k) = \tilde{\mathcal{S}}(k) + \tilde{\mathcal{H}}\tilde{U}(k - 1) + V_{\text{as}}. \quad (3.40)$$

Therefore, (3.26) is updated to

$$Z^*(k) = \tilde{\mathcal{S}}(k) + \tilde{\mathcal{H}}\tilde{U}^*(k - 1) + V_{\text{as}}. \quad (3.41)$$

According to the definition of dominant Markov parameters, $\tilde{\mathcal{H}}\tilde{U}(k - 1)$ dominates

$\tilde{\mathcal{S}}(k)$; thus $\tilde{\mathcal{S}}(k)$ is considered negligible. Hence, (3.41) can be approximated as

$$Z^*(k) \approx \tilde{\mathcal{H}}\tilde{U}^*(k-1) + V_{\text{as}}. \quad (3.42)$$

When the impact of V_{as} on $Z^*(k)$ is large, driving $Z^*(k)$ to zero induces an offset in $\tilde{U}^*(k-1)$ that compensates for the impact of V_{as} , which leads to an additional estimation error.

The additional relative estimation error α_{as} caused by V_{as} is given by

$$\alpha_{\text{as}} = V_{\text{as}} {V_{J_{\text{sd}}}^{-1}}, \quad (3.43)$$

where

$$V_{J_{\text{sd}}} \triangleq \tilde{\mathcal{H}}\tilde{U}^*(k-1), \quad (3.44)$$

When $Z^*(k)$ is zero, the relative estimation error achieves its lower bound, which is determined by the additional estimation error; i.e.,

$$|\epsilon|_{\text{bd}} = |\alpha_{\text{as}}|, \quad (3.45)$$

Therefore, when the relative estimation error is required to be within a bound $\alpha_{\text{as,bd}}$, V_{as} needs to be within the bound

$$V_{\text{as,bd}} = \alpha_{\text{as,bd}} V_{J_{\text{sd}}}. \quad (3.46)$$

Here $Z^*(k)$, $\tilde{\mathcal{H}} = H_0$ and $\tilde{U}^*(k-1)$ are scalars. Then,

$$V_{J_{\text{sd}}} = H_0 J_{\text{sd}}(k). \quad (3.47)$$

For the parameter values used herein, $H_0 = 2 \times 10^{-7} \Omega \text{ m}^3$; and for 1-C CCC mode, $|J_{\text{sd}}|$ is on the order of 10^3 A m^{-3} for most of the operating time. Therefore, $|V_{J_{\text{sd}}}| = |H_0 J_{\text{sd}}|$ is on the order of 10^{-4} V (0.1 mV) for most of the operating time. Then,

according to (3.46), if a bound of $\pm 10\%$ for α_{as} is required, then $V_{as,bd}$ needs to be on the order of 0.01 mV. Similarly, when $V_{as,bd}$ is given, the corresponding $\alpha_{as,bd}$ can be computed from

$$\alpha_{as,bd} = V_{as,bd}/V_{J_{sd}}. \quad (3.48)$$

In the rest of this section, the above analyses are verified by testing the robustness to measurement noise, SOC estimation errors, and modeling error, respectively. The 1-C CCCD cycle is used for excitation in this section except in the cases shown in Figure 3.8 (b) and (c) in Section 3.4.4.2. Based on the observation that the side reaction current density is less identifiable in the CCD mode, only the estimation results during the CCC mode are examined. Other excitations, such as 10-C CCCD cycles and UDDS cycles, can be analyzed in a similar manner.

The voltage differences between different battery models or different simulation situations are denoted as follows.

$$\delta V_{mod1/mod2} \triangleq V_{mod2} - V_{mod1}, \quad (3.49)$$

$$\delta V_{sit1/sit2} \triangleq V_{sit2} - V_{sit1}, \quad (3.50)$$

where the subscripts mod1 and mod2 denote two different models, while sit1 and sit2 denote two different simulation situations.

For simplicity, the names of different models are denoted as follows. The name DFN n denotes the DFN model with n particles per electrode. For example, the DFN model with 50 particles per electrode, which is the model used in Section 3.3, is denoted by DFN50. The name SPM denotes the single particle model.

3.4.2 Robustness to Measurement Noise

In this section, the input and output measurement noise levels are determined individually based on the desired relative estimation error bounds.

As an example, normal distributions with zero mean and tunable standard devi-

ation are assumed for both the input and output measurement noise, i.e.,

$$I_{\text{noise}} \sim \mathcal{N}(0, \sigma_{I_{\text{in}}}^2) [\text{mA}], \quad (3.51)$$

$$V_{\text{noise}} \sim \mathcal{N}(0, \sigma_{V_{\text{in}}}^2) [\text{mV}]. \quad (3.52)$$

$\sigma_{I_{\text{in}}}$ and $\sigma_{V_{\text{in}}}$ can be tuned based on the analysis in Section 3.4.1 and the desired relative estimation error bound. Here a relative estimation error bound on the order of 10% is chosen as the desired estimation accuracy, and thus $|V_{\text{as}}|$ must be on the order of 0.01 mV.

Computing the effect of current measurement noise on voltage analytically is difficult because of the nonlinearity of the battery model. Hence, $\sigma_{I_{\text{in}}}$ is selected numerically based on the simulated voltage response of DFN50 driven by a constant charge current that is 1 C with a perturbation ΔI . The battery model is simulated 11 times with ΔI set to 0 mA, ± 100 mA, ± 10 mA, ± 1 mA, ± 0.1 mA, and ± 0.01 mA. The first simulation with $\Delta I = 0$ mA is the nominal case that records the voltage response of 1-C CCC mode without any perturbation in the input current. ΔV_i ($i = 2, \dots, 11$) is defined as the absolute voltage difference between the i^{th} simulation and the first simulation, that is,

$$\Delta V_i(k) \stackrel{\triangle}{=} |V_i(k) - V_1(k)|. \quad (3.53)$$

Figure 3.3 presents the box-and-whisker plots of ΔV_i corresponding to different ΔI . It can be observed that, in the cases that $\Delta I = \pm 1$ mA, $\Delta V_{6,7}(k)$ are generally on the order of 0.01 mV. Therefore, $\sigma_{I_{\text{in}}}$ is chosen to be 1 mA.

Figure 3.4 (a) shows the estimation results in the presence of input measurement noise with $\sigma_{I_{\text{in}}} = 1$ mA. The relative estimation errors are both bounded within $\pm 12\%$ after the initial transient phase, which is on the desired order of 10% for the relative estimation error bound.

The standard deviation of output measurement noise can be directly set to the level of required $|V_{\text{as}}|$, in this case 0.01 mV. Figure 3.4 (b) presents the estimation

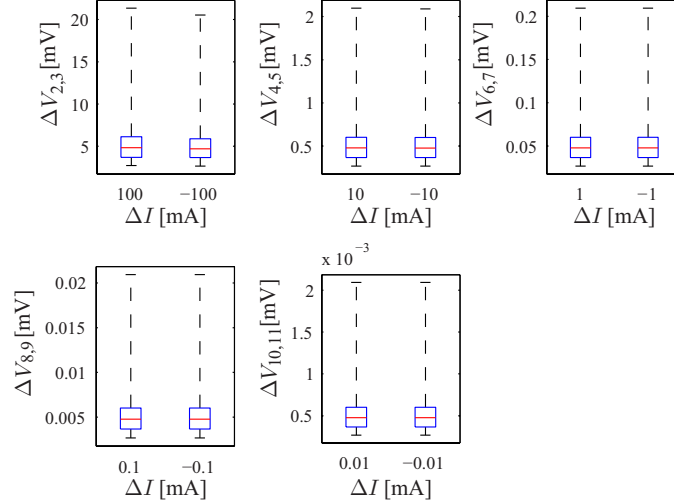


Figure 3.3: The voltage difference ΔV of the DFN50 model caused by the current perturbation ΔI during the 1-C constant current charge mode.

results under output measurement noise with $\sigma_{V_n} = 0.01$ mV. The relative estimation errors are both bounded within $\pm 18\%$ after the initial transient phase, which is also on the desired order of 10%.

Therefore, assuming that the input and output measurement noise are zero mean, Gaussian, and white, the standard deviation for input and output measurement noise must be on the order of 1 mA and 0.01 mV, respectively, in the case where a relative estimation error bound on the order of 10% is required. For other relative estimation error bounds, the tolerable levels of measurement noise can be obtained in the same manner.

3.4.3 Robustness to SOC Estimation Errors

The estimation error in the SOC corresponds to the difference between the state of the main system and the state of the main system model. Because of the energy storage nature of batteries, the dynamics of solid concentration in each electrode contains a single integrator, hence the battery system is marginally stable with one eigenvalue at 1 for each electrode. Moreover, the states are not significantly affected by the subsystem, because the feedback from the side reaction current density on the main system dynamics is negligible. Therefore, the difference in the states that correspond

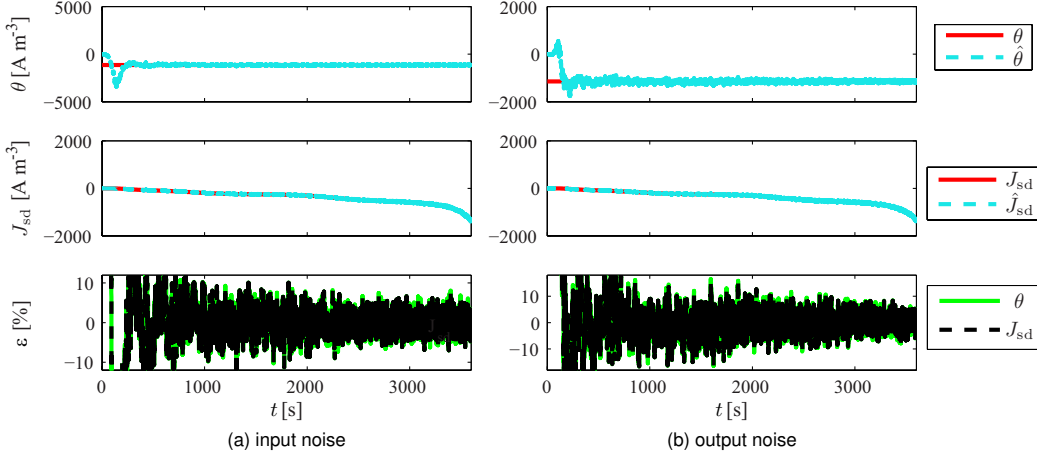


Figure 3.4: The estimates and relative estimation errors ϵ of the subsystem parameter θ and the side reaction current density J_{sd} under the presence of (a) input and (b) output measurement noise. The bounds of the relative estimation errors are on the order of 10% as required.

to eigenvalues at 1 are persistent. The persistent state difference also causes a voltage difference between the true system and the system model, which causes error in the estimates of the side reaction current density and health subsystem parameter.

In this section, a 1% SOC estimation error is assumed because an error on this level is often expected in the SOC estimation [34, 54, 40]. The SOC in the true system is initialized at 0% as in Section 3.3, while the SOC in the system model is initialized at 1%. The estimation results are presented in Figure 3.5 (a). Both $\epsilon_{J_{sd}}$ and ϵ_θ are on the order of 1000% for most of the operating time. Figure 3.5 (b) presents the difference between the cases with 0% and 1% initial SOC levels in the voltage responses of DFN50 during the 1-C CCC mode. It can be observed that the voltage difference is on the order of 1 mV for most of the operating time. This level of voltage difference leads to a value of α_{as} on the order of 1000%, which agrees with the estimation results. The results indicate that the presence of an SOC estimation error can degrade the performance of RCSI in the estimation of side reaction current density. Therefore, an accurate estimation of the SOC is required to minimize the estimation error of the side reaction current density. Alternatively, co-estimation of the SOC and the side reaction current density can be pursued. An example method for the co-estimation of the SOC and the side reaction current density is the TSF

that is discussed in Chapter 4.

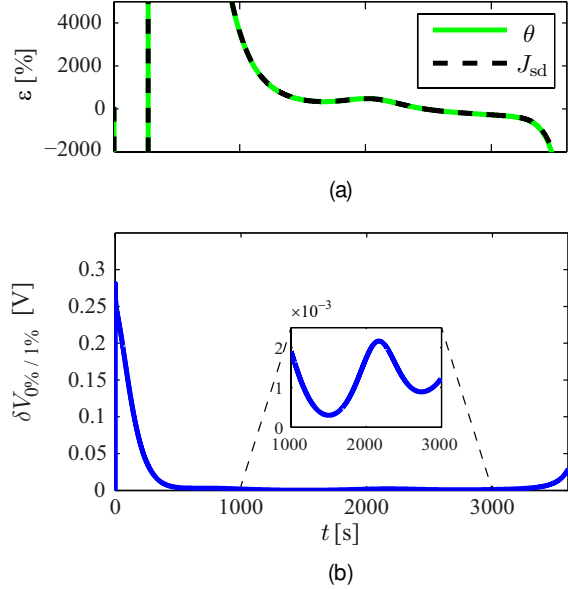


Figure 3.5: (a) The relative estimation errors ϵ of the subsystem parameter θ and the side reaction current density J_{sd} and (b) the voltage difference under the presence of a 1% SOC error. The bound of the relative estimation errors in (a) is on the same order as expected from the voltage difference in (b).

3.4.4 Robustness to Modeling Error

3.4.4.1 Modeling Error in Main System Model

Many factors can contribute to the modeling error in the main system model, such as the truncation errors caused by approximating an infinite dimensional system with a finite-dimensional system, parameter uncertainties and discrepancies between the physical effects included in the mathematical model and the true physics.

I. Error in Model Structure

In this section, the impact of the main system modeling errors caused by the finite-dimensional approximation is analysed as an example of the error in model structure. DFN50 is used as the true main system in the simulation, while either SPM or the DFN model with fewer particles per electrode (e.g., DFN30 and DFN10) is used as the main system model. The estimation errors caused by these modeling errors

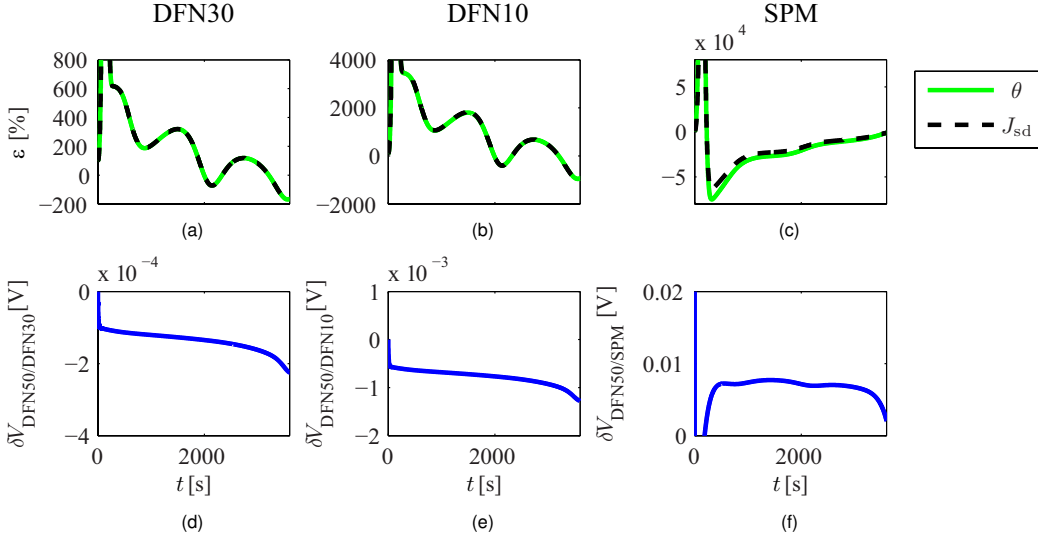


Figure 3.6: The relative estimation errors ϵ of the subsystem parameter θ and the side reaction current density J_{sd} under the 1-C constant current charge mode with DFN50 as the true main system and (a) DFN30, (b) DFN10, and (c) SPM as the main system model. The differences in the voltage responses during 1-C constant current charge mode between DFN50 and (d) DFN30, (e) DFN10, and (f) SPM. The bounds of the relative estimation errors in (a), (b), and (c) are on the same orders as expected from the voltage differences in (d), (e), and (f), respectively.

are compared with the anticipated estimation errors based on the voltage differences between different models to confirm the analysis in Section 3.4.1.

Figure 3.6 (a), (b) and (c) present the relative estimation errors in cases with DFN30, DFN10, and SPM as the main system model, which are on the order of 100%, 1000% and $10^4\%$ for most of the operating time, respectively. Figure 3.6 (d), (e) and (f) show the voltage difference under 1-C CCC mode between DFN50 and DFN30, DFN10, as well as SPM, which are on the order of 0.1 mV, 1 mV and 10 mV for most of the operating time, respectively. Based on these voltage differences, according to (3.48), the anticipated estimation errors in the three cases are on the order of 100%, 1000% and $10^4\%$, respectively. Therefore, the levels of anticipated estimation errors from the voltage differences in the three cases are all in accordance with the observed levels of the corresponding relative estimation errors.

Unlike all the other examples herein, Figure 3.6 (c) shows an appreciable discrepancy between $\epsilon_{J_{sd}}$ and ϵ_θ . This is an example where a large modeling error in the

main system model yields different relative estimation errors in the side reaction current density and health subsystem parameter by causing a large difference between y and \hat{y} . This result illustrates that the accuracy of the identified health subsystem parameter and of the estimated side reaction current density are not necessarily the same.

The results show that the modeling errors in the main system models degrade the accuracy of the estimated side reaction current density. The estimation is less accurate with a smaller number of particles per electrode in the main system model. Therefore, the estimation of the side reaction current density using RCSI requires a high fidelity battery model with very small voltage difference from the real battery.

A competing requirement for a high fidelity model is low computation complexity for real-time simulation and on-line estimation. For the DFN50 model used herein, the simulation is five times faster than the real time on average. This time difference indicates that the computation required by the estimation algorithm designed herein can be done within a much shorter time than required for on-line estimation. The simulations herein are performed using Matlab 2014a on a 64-bit computer with 2.7-GHz processor. Although practical applications may not have this computational power, the computational speed gained by switching to a compiled language can partially offset the loss in the computational power. Methods also exist to significantly reduce the computational complexity of numerically solving the DFN model [55, 66]. Therefore, even with the requirement of using a high fidelity model, the proposed method is still potentially suitable for on-line estimation.

II. Error in Model Parameters

In this section, the impact of parametric error caused by battery degradation on the estimation accuracy is studied. Two parameters, R_{film} and $D_{s,n}$, are selected as the example parameters with error because they are reported to change as the LiFePO₄ battery degrades [46, 44]. In particular, [46] reports 100% and 560% increase in R_{film} and diffusion coefficients D_s , respectively, after 600 hybrid pulse power characterization cycles at 25 °C. For the diffusion coefficients, only the one at the anode, namely $D_{s,n}$, is increased because changes in the diffusion coefficient are caused by accumu-

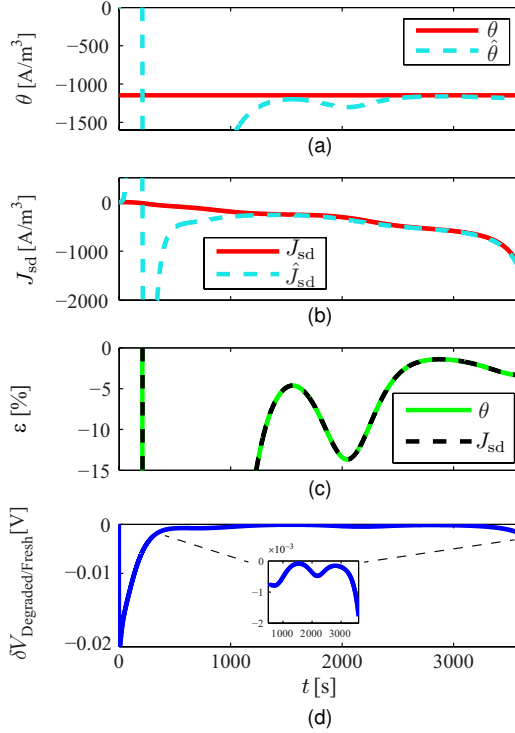


Figure 3.7: The estimates of (a) the subsystem parameter θ and (b) the side reaction current density J_{sd} , and (c) relative estimation errors ϵ under parametric errors in R_{film} and $D_{s,n}$. (d) presents the voltage difference between the DFN50 model with values of R_{film} and $D_{s,n}$ in fresh and degraded batteries during 1-C constant current charge mode.

lation of the SEI film [46] and the SEI is herein assumed to grow only at the anode [28]. The parameters for the fresh battery are used in the system model and R_{film} and $D_{s,n}$ in the true system are increased according to the percentages reported in [46] to simulate the estimation of the side reaction current density in a degraded battery using the parameters for the fresh battery in the model.

Figure 3.7 (a) – (c) shows the estimation results when the errors in R_{film} and $D_{s,n}$ are considered. It can be observed that the estimates \hat{J}_{sd} and $\hat{\theta}$ stay close to their true values after 1000 seconds, and the relative estimation errors ϵ_θ and $\epsilon_{J_{sd}}$ are both bounded within [-15, 0]% after 1200 seconds. Figure 3.7 (d) shows the voltage difference, $\delta V_{\text{Degraded}/\text{Fresh}}$, between the DFN50 model with values of R_{film} and $D_{s,n}$ in fresh and degraded batteries during 1-C CCC mode. It can be observed that $\delta V_{\text{Degraded}/\text{Fresh}}$ starts on a level as high as 20 mV at the beginning of 1-C CCC mode,

which corresponds to the region where the estimation errors are large. After 1200 seconds, when the relative estimation errors are on the order of 10% in Figure 3.7 (a) – (c), $\delta V_{\text{Degraded}/\text{Fresh}}$ is on the order of 0.01 to 0.1 mV. Hence, the relative estimation error is on the same order as (when $\delta V_{\text{Degraded}/\text{Fresh}}$ is on the order of 0.01 mV) or one order of magnitude more accurate than (when $\delta V_{\text{Degraded}/\text{Fresh}}$ is on the order of 0.1 mV) what is expected from the analysis in Section 3.4.1. This is because J_{sd} and R_{film} are highly correlated, while the analysis in Sec. 3.4.1 assumes independence between J_{sd} and additional sources. Hence, $\delta V_{\text{Degraded}/\text{Fresh}}$ is a combined effect of the parametric errors and the change in J_{sd} caused by the parametric errors, which is larger than the voltage difference caused by the parametric errors alone. At the end of the 1-C CCC mode, although the voltage difference $\delta V_{\text{Degraded}/\text{Fresh}}$ increases to slightly over 1 mV, neither the magnitude nor the duration of this increase is significant enough to cause large changes in the estimates and thus the relative estimation errors stays below 10%. This result shows that the estimation of the side reaction current density is still accurate even under the considered parametric errors in $D_{\text{s},n}$ and R_{film} introduced by battery ageing.

3.4.4.2 Form Discrepancy between Subsystem and Subsystem Model

It is hitherto assumed that the forms of the subsystem and the subsystem model are exactly the same. However, this assumption is usually not satisfied in practice. Moreover, representing a subsystem with a subsystem model of different form causes difficulty in subsystem identification, and results in less accurate estimates of the side reaction current density.

In this section, the performance of RCSI is examined when the form of the subsystem model is different from the form of the true subsystem. In particular, an example is provided to show how a subsystem model with identical SOH parameters can be used to estimate a true subsystem with non-identical SOH parameters. Hence, the true subsystem follows the form as in (2.61), while the form of the subsystem model still follows (3.4). The following distribution of K_{SOH}^m is arbitrarily chosen for the true

subsystem as an example.

$$k_{\text{SOH}}^m \sim \mathcal{N}(k_0, 25k_0^2), \quad (3.54)$$

$$K_{\text{SOH}}^m = |k_{\text{SOH}}^m|, \quad (3.55)$$

where k_0 equals to the value of $K_{\text{SOH}}^{\text{unif}}$ in Section 3.3. Simulations show that distributions with higher covariances can lead to larger estimation error.

Furthermore, after removing the assumption in (3.36)-(3.38) that no form discrepancy exists between the subsystem and the subsystem model, the following variables are re-defined in this section,

$$J_{\text{sd}} \triangleq \frac{1}{N} \sum_{m=1}^N J_{\text{sd}}^m, \quad \hat{J}_{\text{sd}} \triangleq \hat{J}_{\text{sd}}^{\text{ave}}, \quad (3.56)$$

$$\theta \triangleq \frac{\sum_{m=1}^N K_{\text{SOH}}^m y_\phi^m}{\sum_{m=1}^N y_\phi^m}, \quad \hat{\theta} \triangleq \hat{K}_{\text{SOH}}^{\text{unif}}, \quad (3.57)$$

$$y \triangleq \frac{1}{N} \sum_{m=1}^N y_\phi^m, \quad \hat{y} \triangleq \hat{y}_\phi^{\text{ave}}. \quad (3.58)$$

Figure 3.8 (a) presents the estimation results with 1-C CCC mode. Both $\epsilon_{J_{\text{sd}}}$ and ϵ_θ are within $\pm 20\%$ after the transient phase. Simulations show that the voltage difference is generally on the order of 10^{-3} V between DFN50 with the health subsystem parameters following the distribution in (3.54) to (3.55) and DFN50 with the health parameters all equal to the weighted average of the true parameters. This indicates that the relative estimation errors are expected to be on the order of 10%, which agrees with the $\pm 20\%$ bound in the estimates.

Besides the 1-C CCC mode, the UDDS cycle is also used as the excitation to examine the impact of form discrepancy in the subsystem model. Figure 3.8 (b) presents the estimation results with the UDDS cycle, where the relative estimation errors are both within $\pm 20\%$ during the whole cycle. Oscillations during the whole cycle and divergence at the end of the cycle are present due to the weak identifiability

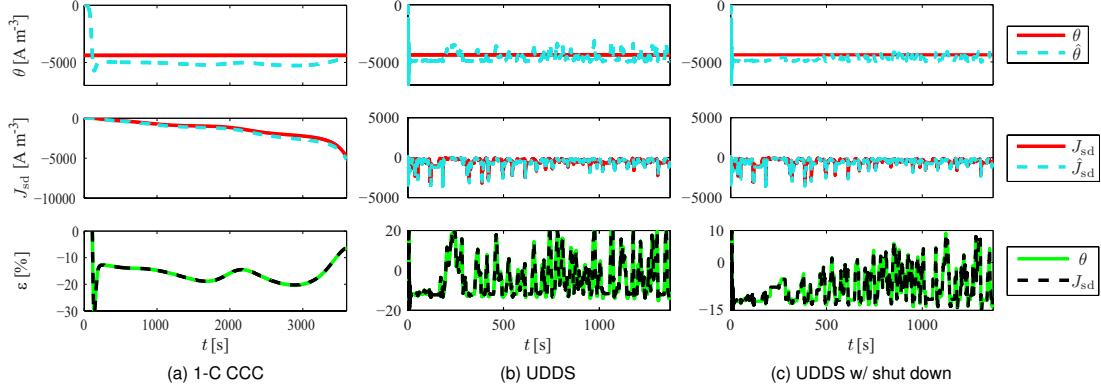


Figure 3.8: The relative estimation errors ϵ of the subsystem parameter θ and the side reaction current density J_{sd} under (a) the 1-C constant current charge (CCC) mode and (b) the urban dynamometer driving schedule (UDDS) cycle under the presence of form discrepancy between the subsystem and the subsystem model. (c) presents the relative estimation errors under the same UDDS cycle as in (b), but with the estimation algorithm shut down whenever discharge current is above 5 C. Note that shutting down the estimation algorithm during high-C-rate discharge reduces estimation errors.

caused by high discharge C-rate and low SOC level as in Figure 3.2 (c).

The estimation errors can be reduced by shutting down the estimation algorithm during high-C-rate discharge when the true side reaction current density is small. In this case, the algorithm operates only when the input current can produce a large true side reaction current density, which is also the time when an estimate of the side reaction current density is needed. The threshold of the discharge C-rate for which the algorithm is shut down is chosen based on the particular current profile to balance the number of effective data points for estimation and the identifiability. Figure 3.8 (c) presents the estimation results of the same case as in Figure 3.8 (b), but with the algorithm shut down whenever the discharge current is above 5 C. Comparison between Figure 3.8 (b) and Figure 3.8 (c) shows an improvement in the bound for the relative estimation errors from $\pm 20\%$ to $[-15, 10]\%$. This improvement in the estimation accuracy can be more significant when the excitation current is more aggressive.

Similarly, to address the identifiability issue associated with low SOC, limiting the SOC region during which the estimation algorithm is operated can further improve

the estimation accuracy near the end of the UDDS cycle. Because a low-accuracy SOC estimate suffices to determine the time to shut down the estimation algorithm, a possible method to estimate the true SOC level is Coulomb counting.

3.4.5 Discussions and Extensions of the Simulation Results

For all the results in this section, similar results can be obtained for other types of excitation current. The numerical results depend on $V_{J_{sd}}$ for the particular excitation type and the voltage errors caused by additional sources. Notice that even if one excitation type has a higher $V_{J_{sd}}$, it does not necessarily yield more robust estimation results, because the voltage difference caused by additional sources also varies among different excitation types. For example, in 10-C CCC mode, $V_{J_{sd}}$ is generally 10 times higher than that for 1-C CCC mode. However, the expected bound for the relative estimation error in the 10-C case is not 1/10 of the bound for the 1-C case when there is modeling error in the main system model, because the voltage differences among the SPM and the DFN models are also larger for high C rate. Therefore, the expected bound for the relative estimation error for one excitation type cannot be extrapolated to other excitation types. The robustness level for an excitation type can be obtained by following the framework developed in Section 3.4.1.

Furthermore, the expected performance of RCSI on real-life battery cycling data can be deduced by analyzing the difference between voltage responses of battery models and real-life battery measurement data. The result in [63], which identifies the parameter set used herein from experimental data, shows that the absolute error between the voltage measurements and the simulated voltage of the DFN model with this parameter set is below 40 mV for 80% of the time. This voltage error is about 10^3 larger than the $V_{as,bd}$ identified in Section 3.4.1 that corresponds to the relative estimation error bound of 10%. This analysis indicates that estimation of the side reaction current density for the same battery under the same experimental condition in [63] is expected to be difficult given that the modeling error is relatively large compared to the voltage difference caused by the side reaction.

However, this does not mean that the side reaction current density cannot be esti-

mated in practice. The results from the numerical analyses in Section 3.4 is applicable only to this particular battery parameter set, with this particular cycling profile, under this particular experimental condition. The side reaction current density could still be estimated successfully in other cases with different battery parameter sets, cycling profiles, or experimental conditions as long as they can make the corresponding V_{as} below the desired $V_{as,bd}$. Meanwhile, according to (3.46), given a desired $\alpha_{as,bd}$, $V_{as,bd}$ is a function of $V_{J_{sd}}$. Therefore, the side reaction current density can be successfully estimated within a reasonable $\alpha_{as,bd}$ even under the presence of practical non-ideal conditions for scenarios where the battery parameters or the cycling profile yield a large $V_{J_{sd}}$.

The main generalizable conclusion that can be drawn from Section 3.4 is that the side reaction current density can be very sensitive to non-ideal conditions that cause errors in the measurement or estimation of the voltage, because the side reaction current density is a small value that has a limited impact on the voltage. When this algorithm is applied to battery experiment data to estimate the side reaction current density, the analysis in Section 3.4.1 needs to be followed in order to predict the margin of the robustness.

Various methods can be applied to improve the robustness in estimation of the side reaction current density. To improve the robustness to the presence of measurement noise and modeling errors, very accurate sensors and models with higher fidelity are needed to obtain a value of V_{as} that satisfies the required $V_{as,bd}$. Under the presence of SOC estimation errors, the TSF, an inaccessible subsystem estimation algorithm modified from RCSI, is developed in Chapter 4 to improve the estimation accuracy of the side reaction current density.

3.5 A Framework to Obtain Lower Bound of Relative Estimation Errors for Voltage-Error-Based Algorithms

The analyses in Section 3.4.1 can be easily generalized to other estimation algorithms that estimate the side reaction current density by minimizing the error between the measured voltage and the voltage estimate of a battery model. In this section, a general framework is developed to obtain the lower bound of the relative estimation error of the side reaction current density when estimation is based on minimizing voltage errors. This framework also gives the same lower bound of the covariance of the estimates as given by the Fisher information [67, 68], which is a method used in the field of information theory to obtain the lower bound of covariance of unbiased estimates. Notice that, unlike the lower bound of the covariance that applies only to unbiased estimates, the lower bound of the relative estimation error provided by this framework does not require the estimate to be unbiased.

Define the sensitivity of the voltage to the side reaction current density as

$$s(V|J_{\text{sd}}) \triangleq \frac{\partial V}{\partial J_{\text{sd}}}. \quad (3.59)$$

It can be observed that $\tilde{\mathcal{H}}$ in RCSI is a realization of $s(V|J_{\text{sd}})$ through the Markov parameters. Then, the voltage caused by J_{sd} is

$$V_{J_{\text{sd}}} \triangleq s(V|J_{\text{sd}})J_{\text{sd}}. \quad (3.60)$$

Then the error z between the measured voltage and the estimated voltage can be decomposed into

$$z = \hat{V} - V = s(V|J_{\text{sd}})(\hat{J}_{\text{sd}} - J_{\text{sd}}) + V_{\text{as}}. \quad (3.61)$$

For any estimation algorithm whose goal is to minimize the voltage error, the relative

estimation error of the side reaction current density achieves its lower bound when $z = 0$. It can be deduced from (3.61) that when $z = 0$,

$$\hat{J}_{\text{sd}} - J_{\text{sd}} = \frac{V_{\text{as}}}{s(V|J_{\text{sd}})}. \quad (3.62)$$

Combining (3.60) and (3.62) yields that the lower bound of the relative estimation error is

$$|\epsilon_{J_{\text{sd}}}| = \left| \frac{\hat{J}_{\text{sd}} - J_{\text{sd}}}{J_{\text{sd}}} \right| = \left| \frac{V_{\text{as}}}{V_{J_{\text{sd}}}} \right|, \quad (3.63)$$

which is the same as the result shown in (3.43) and (3.45).

The equivalence between (3.63) and (3.43) and (3.45) demonstrates that the lower bound of the relative estimation error under non-ideal conditions that cause errors in either voltage measurements or voltage estimates is determined by the sensitivity $s(V|J_{\text{sd}})$ of the voltage to the side reaction current density, the magnitude of the side reaction current density J_{sd} , and the voltage error V_{as} caused by non-ideal conditions. This lower bound is also independent of the estimation algorithm as long as the algorithm estimates the side reaction current density by minimizing the voltage error. Therefore, all the results and discussions in Section 3.4 that are obtained in the context of RCSI can also be applied to estimation of the side reaction current density using other estimation algorithms based on minimization of voltage error. It can also be concluded that the estimation results obtained using RCSI in Section 3.4 have achieved the lower bound of the relative estimation errors of the side reaction current density.

The lower bound for the relative estimation error deduced in (3.63) also yields the same lower bound of the covariance of unbiased estimates as given by the Fisher information, a quantity that measures how easily one can observe parameters in a probability density function from collected data [64]. The Cramér-Rao bound of the variance of an unbiased parameter estimator is equal to the inverse of the Fisher

information [67, 68]. The Fisher information is defined as [67, 64]

$$\mathcal{I}(\zeta) = \frac{\mathbf{s}(y|\zeta)^T \mathbf{s}(y|\zeta)}{\sigma^2}, \quad (3.64)$$

where \mathbf{s} is the sensitivity matrix of the output y to ζ , the variable to estimate, and σ^2 is the covariance of the noise in the output measurement. Then the lower bound of the covariance of the estimate of ζ is [67]

$$\text{cov}(\hat{\zeta}) = \frac{1}{\mathcal{I}(\zeta)}. \quad (3.65)$$

In estimation of the side reaction current density, the sensitivity of the output voltage to the side reaction current density is $s(V|J_{\text{sd}})$ and σ^2 is the covariance of V_{as} . Then according to the Fisher information, the covariance of an unbiased estimate of the side reaction current density satisfies

$$\text{cov}(\hat{J}_{\text{sd}}) \geq \frac{1}{\mathcal{I}(J_{\text{sd}})} = \frac{\text{cov}(V_{\text{as}})}{s(V|J_{\text{sd}})^2} = \frac{\mathbb{E}(V_{\text{as}}^2)}{s(V|J_{\text{sd}})^2}. \quad (3.66)$$

The final equality is because the noise in the Fisher information is assumed to be zero mean, and thus $\text{cov}(V_{\text{as}}) = \mathbb{E}(V_{\text{as}}^2)$.

On the other hand, when \hat{J}_{sd} is an unbiased estimate of J_{sd} , $\mathbb{E}(\hat{J}_{\text{sd}}) = J_{\text{sd}}$, and thus

$$\text{cov}(\hat{J}_{\text{sd}}) = \mathbb{E} \left[\left(\hat{J}_{\text{sd}} - J_{\text{sd}} \right)^2 \right]. \quad (3.67)$$

The lower bound of the covariance of the estimate is achieved with the relative estimation error achieving its lower bound. Substituting (3.62) into (3.67), the covariance of the estimate \hat{J}_{sd} when the lower bound of the relative estimation error is achieved can be expressed as

$$\text{cov}(\hat{J}_{\text{sd}}) = \frac{\mathbb{E}[V_{\text{as}}^2]}{s(V|J_{\text{sd}})^2}, \quad (3.68)$$

which is the lower bound of the covariance of an unbiased \hat{J}_{sd} .

Comparing (3.66) and (3.68), it can be observed that the analyses of the lower bound of the relative estimation error and the Fisher information yield the same lower bound for the covariance of the estimate of the side reaction current density. This equality is due to the fact that both the lower bound of the relative estimation error deduced herein and the Fisher information are obtained by comparing the sensitivity of the output voltage to the side reaction current density and the voltage error caused by additional sources.

3.6 Simulation Results with LMO-Mixture Battery Parameters

In this section, the estimation technique is applied to a different parameter set for a different battery chemistry, namely the LMO-mixture chemistry. The estimation is performed under example cases such as ideal conditions and SOC estimation errors through simulations. The goal of this section is to demonstrate that the estimation technique, including RCSI-based estimation algorithm and the robustness analysis in Section 3.5, is not restricted to the parameter set of the LiFePO₄ battery used in Section 3.3 and 3.4, but is generally applicable to various Li-ion battery types and chemistries to monitor degradation caused by side reactions that consume cyclable Li-ions.

The parameters of the SOC model are adopted from [3], where the parameters are identified from experimental data of an LMO-mixture battery. Due to lack of parameters for the side reactions in LMO-mixture batteries, the parameters of the SOH model are again adopted from [28]. The number of particles is selected to be 50 per electrode. The sampling time is 0.2 s. For RCSI, the weights in the retrospective cost function (3.27) are set as $R_U = 0$ and $R_Z = 1$, and the parameters for Kalman filter update (3.32) and (3.33) are set as $Q = 0.1$, $R_k = 0.5$, and $R_1 = 0$. The parameter estimate and error covariance matrix are initialized at $\theta(0) = 0$ and

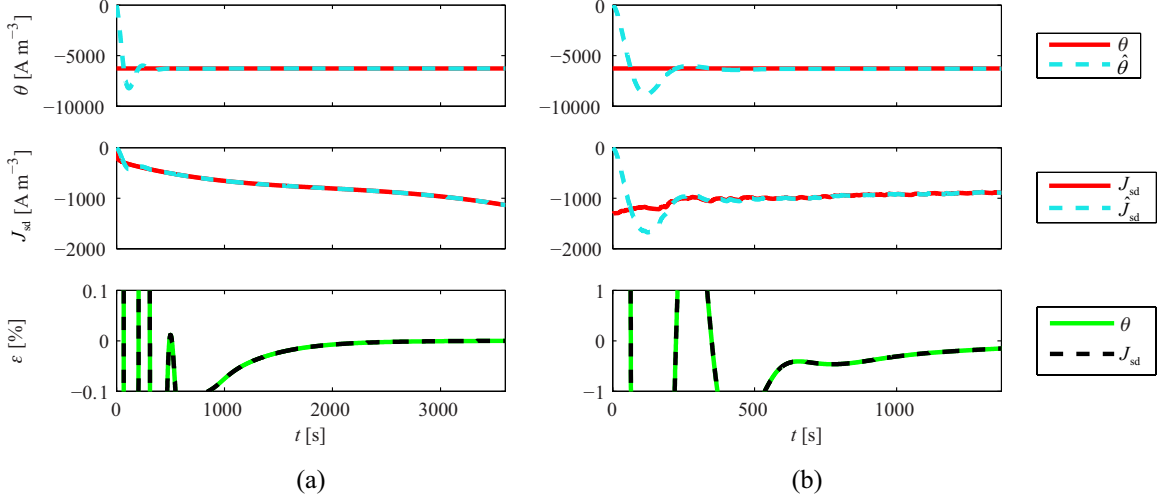


Figure 3.9: The estimates and relative estimation errors ϵ of the subsystem parameter θ and the side reaction current density J_{sd} using a parameter set for an LMO-mixture battery under ideal conditions with two input currents: (a) a 1-C constant current charge (CCC) cycle and (b) a simulated current profile generated by an EV following an Urban Dynamometer Driving Schedule (UDDS).

$P(0) = 100$, respectively. The Markov parameter is set as $\tilde{\mathcal{H}} = H_0 = 4 \times 10^{-7} \Omega \text{ m}^3$.

The side reaction current density is first estimated under ideal conditions using both 1-C CCC and the UDDS cycles. The initial SOC is set at 0% and 100% for 1-C CCC and the UDDS cycle respectively. Figure 3.9 shows the estimates $\hat{\theta}$ and \hat{J}_{sd} , and the relative estimation errors $\epsilon_{\hat{\theta}}$ and $\epsilon_{\hat{J}_{sd}}$ under ideal conditions. It can be observed that the estimates converge to their respective true values within 500 seconds under both the 1-C CCC and UDDS cycles. The final relative estimation errors $\epsilon_{\hat{\theta}}$ and $\epsilon_{\hat{J}_{sd}}$ are bounded within $\pm 0.1\%$ and $\pm 1\%$ for the 1-C CCC and UDDS cycles, respectively. It can also be observed that the magnitude of J_{sd} is larger during the UDDS cycle than during the 1-C CCC cycle. This result indicates that the unidentifiability observed during high C-rate discharge for the LiFePO₄ battery does not apply to this parameter set for the LMO-mixture battery. On the contrary, the observability of θ and J_{sd} is expected to be stronger during the UDDS cycle because of the larger J_{sd} . The bound of relative estimation errors during the UDDS cycle is still larger than the 1-C CCC cycle because the dynamic J_{sd} trajectory makes the estimates more difficult to converge.

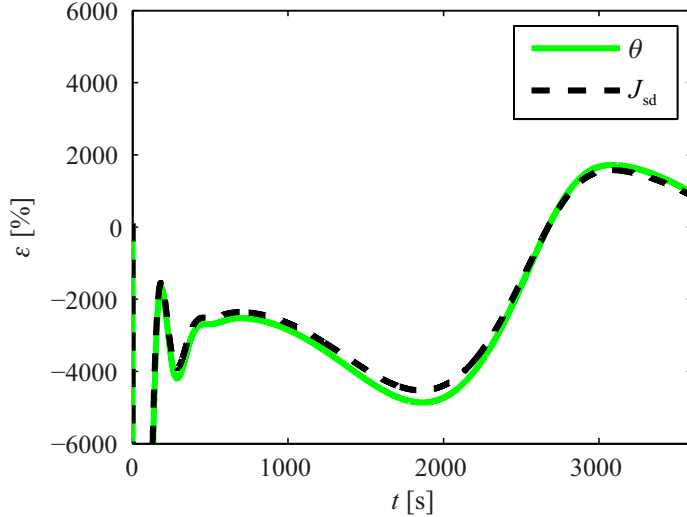


Figure 3.10: The relative estimation errors ϵ of the subsystem parameter θ and the side reaction current density J_{sd} using a parameter set for an LMO-mixture battery under 1% SOC estimation error during 1-C constant current charge (CCC) cycle.

Then, a simulation is performed to estimate the side reaction current density under the 1-C CCC cycle under 1% SOC estimation error as an example. All the other parameters and settings of the models and RCSI are the same as under the ideal conditions. Figure 3.10 presents the relative estimation errors $\epsilon_{J_{\text{sd}}}$ and ϵ_{θ} under the 1% SOC estimation error. It can be seen that the relative estimation errors are on the order of $10^3\%$.

The result shown in Figure 3.10 can be explained using the framework developed in Section 3.5. In the nonlinear battery model, the sensitivity of the nonlinear voltage to the side reaction current density can be approximated by comparing the change in the output voltage caused by perturbing the side reaction current density from the nominal value by a small amount while all other parameters remain unperturbed [69]. To this end, the DFN50 model is simulated three times using 1-C constant current charge. The first time is with the value of all parameters being the same as in the LMO-mixture parameter set used in the true system. The voltage simulated from the first time is denoted as $V_{100\%J_{\text{sd}}}$. Then the DFN50 model is simulated with $\pm 1\%$ perturbation in the value of $i_{0,\text{sd}}$, and thus J_{sd} is perturbed by $\pm 1\%$ as well. The voltage responses in the final two simulations are denoted with $V_{99\%J_{\text{sd}}}$ and $V_{101\%J_{\text{sd}}}$,

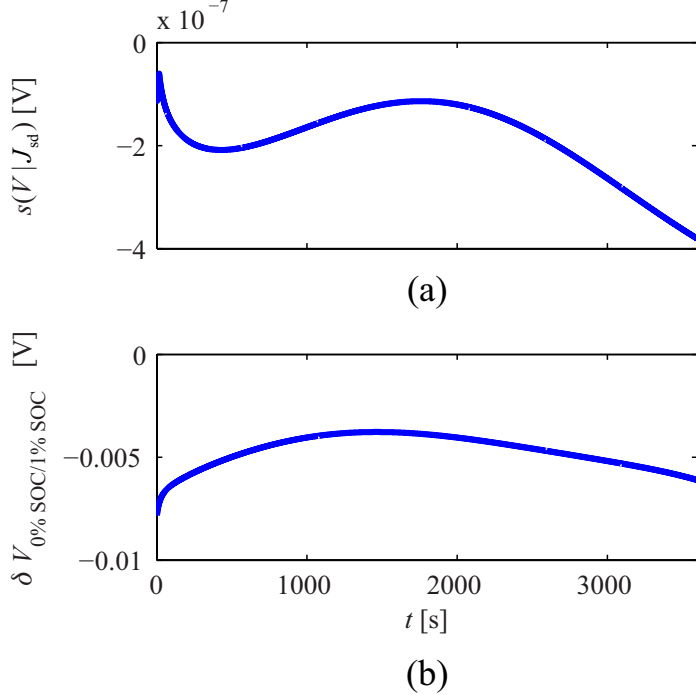


Figure 3.11: (a) The sensitivity of the voltage to the side reaction current density, $s(V|J_{\text{sd}})$, and (b) the voltage difference under the presence of a 1% SOC error, $\delta V_{0\% \text{SOC}/1\% \text{SOC}}$ using the LMO-mixture parameter set.

respectively. Then, the sensitivity of the voltage to the side reaction current density is approximated by

$$s(V|J_{\text{sd}}) \approx \frac{|V_{100\% J_{\text{sd}}} - V_{99\% J_{\text{sd}}}| + |V_{100\% J_{\text{sd}}} - V_{101\% J_{\text{sd}}}|}{2 \times 1\% J_{\text{sd}}}. \quad (3.69)$$

Figure 3.11 (a) depicts $s(V|J_{\text{sd}})$ obtained using (3.69). It can be observed that $s(V|J_{\text{sd}})$ is on the order of $10^{-7} \text{ V m}^3 \text{ A}^{-1}$. This result agrees with the fact that H_0 in RCSI, which is also a measure of the sensitivity of the voltage to the side reaction current density, is also set at $O(10^{-7})$. Figure 3.11 (b) shows the voltage difference $\delta V_{0\% \text{SOC}/1\% \text{SOC}}$ for the LMO-mixture battery. It can be observed that $\delta V_{0\% \text{SOC}/1\% \text{SOC}}$ is on the order of 10^{-3} V . In addition, Figure 3.9 shows that J_{sd} is on the order of 10^3 A m^{-1} . According to (3.63), the lower bound of the relative estimation errors is expected to be on the order of 10³%, which agrees with the relative estimation errors observed in Figure 3.10. This result shows that RCSI has achieved the lower bound of the relative estimation errors.

This section demonstrates that the estimation technique, including RCSI-based estimation algorithm and the robustness analysis in Section 3.5, is also applicable to a parameter set for an LMO-mixture battery to estimate the side reaction current density and analyze the robustness of the estimation. The fact that the technique can be applied to both parameter sets for LiFePO₄ and LMO-mixture batteries shows that the technique developed in Chapter 3 is not restricted to certain parameters or certain battery chemistries.

3.7 Summary and Conclusions

In this chapter, the effectiveness of RCSI in estimation of the side reaction current density is explored. The side reaction current density is estimated directly for the first time as the SOH indicator. The battery SOH process that produces the side reaction current density is formulated as an inaccessible subsystem in the battery. The estimate of the side reaction current density is obtained by identifying the inaccessible battery SOH subsystem using RCSI. Robustness of the side reaction current density estimation is examined under various non-ideal conditions, such as measurement noise, SOC estimation errors, modeling errors in the main system model, and the form discrepancy between the subsystem and the subsystem model.

When the ideal condition (i.e., no measurement noise, no SOC estimation error and no modeling error) is assumed, the results show that RCSI can accurately and quickly estimate the side reaction current density as well as identify the battery health subsystem when the degradation effect is significant. Using a parameter set for a LiFePO₄ battery, an accurate estimation can be made throughout slow (1-C) and fast (10-C) CCCD cycle, and the UDDS cycle, with relative estimation errors bounded within $\pm 0.1\%$, $\pm 1\%$ and $\pm 0.3\%$, respectively.

This chapter also develops a framework to obtain the lower bound of relative estimation error under non-ideal conditions for algorithms that estimate the side reaction current density by minimizing the error between measured voltage and estimated voltage. This framework determines that the lower bound of the relative estimation error

of the side reaction current density is proportional to the voltage error caused by non-ideal conditions, and inversely proportional to the sensitivity of the voltage to the side reaction current density and the magnitude of the side reaction current density itself. Simulations verify that RCSI can achieve the lower bound of the relative estimation error of the side reaction current density provided by this framework under the presence of measurement noise, SOC estimation errors, modeling errors in the main system model, and the form discrepancy between the subsystem and the subsystem model. With the LiFePO₄ parameter set used herein, the threshold for the voltage error caused by non-ideal conditions is identified to be $O(0.01)$ mV so that the bound of the relative estimation errors is on the order of $\pm 10\%$ under 1-C CCC mode. Based on this small threshold value, the algorithm is expected to be sensitive to non-ideal conditions, which is a result of the side reaction current density having a small impact on the battery output voltage. Based on the results obtained, high fidelity models and accurate sensors would be needed in practice. However, these numerical results are specific to the particular parameter set and the cycling profiles considered herein. For other scenarios where the combination of the battery parameters and the cycling profile yield a larger $V_{J_{sd}}$ or a smaller V_{as} , the side reaction current density can be estimated with a smaller $\alpha_{as,bd}$ even under the presence of non-ideal conditions.

The proposed method for estimating the side reaction current density is generally applicable to various Li-ion battery types and chemistries to monitor degradation caused by side reactions that consume cyclable Li-ions. Although most of the numerical results herein are obtained from simulations using a parameter set for a LiFePO₄ battery, the proposed estimation technique, including the method for estimating the side reaction current density using RCSI and the framework analyzing its robustness, can also be applied to other parameter sets and other battery chemistries to monitor the SOH change resulting from any electrochemical-based degradation mechanism that consumes cyclable Li-ions. A few simulation examples using a parameter set of an LMO-mixture battery is provided to verify the generality of this estimation technique.

In summary, this chapter makes three main contributions. First, the side reaction

current density is estimated as a direct SOH indicator for the first time. Second, the side reaction current density and the SOH subsystem parameter are estimated using RCSI. Finally, a framework is provided to analyze the robustness of estimating the side reaction current density to non-ideal conditions that cause errors in the measurement or estimate of the voltage. The analyses from the framework are confirmed with simulation results, based on which predictions are made on the robustness of estimating the side reaction current density in practice.

Chapter 4

Two-Step Filter

4.1 Introduction

Chapter 3 frames the battery SOH monitoring problem as an inaccessible subsystem identification problem and conceives an approach to monitor SOH by estimation of the side reaction current density when SOC is perfectly known. However, an SOC estimation error on the level of 1% is often expected in practice [54, 34, 40].

Simulation results in Chapter 3 show that estimation of the side reaction current density is sensitive to SOC estimation errors. RCSI can correct for state estimation errors when the system is both controllable through the feedback of the subsystem output and observable. However, due to the negligible feedback from the side reaction current density to the battery electrochemical dynamics, the controllability of the battery system is very weak. Furthermore, the fact that there is a feedthrough from the side reaction current density to the terminal voltage [65] and that a battery is a marginally stable system due to its energy storing nature makes the SOC estimation errors persistent. Hence, a new approach is needed that can track the side reaction current density under SOC estimation errors.

In this chapter, a new inaccessible subsystem identification technique called the two-step filter (TSF) is introduced for SOH monitoring to overcome the problems caused by persistent SOC estimation errors. Similar to RCSI, the system is divided into two parts: the Main System represents the part of the system that is known and

the Subsystem refers to the part that is unknown and to be identified. In the battery case, they correspond to the electrochemical dynamics and the health subsystem, respectively. SOC estimation error is caused by an initialization error in the states of the Main System that correspond to eigenvalues of 1. Thus, the first step in the TSF is a modification of RCSI to take into account the Main System state error. In the second step, the estimation goal is expressed as a nonlinear function of both the battery health subsystem parameter and the Main System state initialization error. Then, the modified extended Kalman filter (MEKF) [70] is used to estimate the unknown subsystem parameter and the Main System state error. In essence, the TSF minimizes the impact of the SOC estimation errors on estimation accuracy of the side reaction current density by evaluating the voltage error caused by the SOC estimation errors and then eliminating this voltage error in estimation of the side reaction current density.

The rest of the chapter first demonstrates the performance of the TSF using a time varying linearized battery model. Then the application of the TSF on the nonlinear battery model is discussed.

4.2 The Development of the Two-Step Filter

4.2.1 Problem Setup

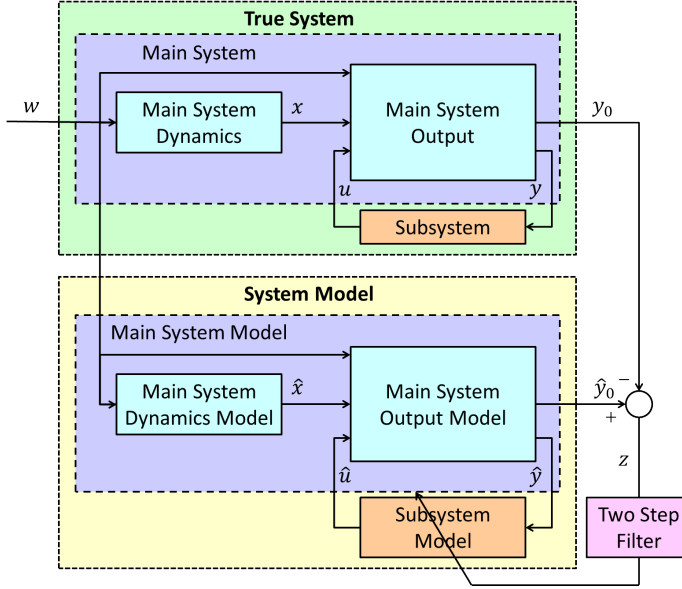


Figure 4.1: The architecture for the two-step filter.

Figure 4.1 shows the generic framework for the TSF. The True System consists of a known Main System and an unknown Subsystem. The dynamic equations and the output equations of the Main System are considered separately, because the Subsystem is in a closed-loop with only the output equations due to the assumption that the Subsystem output $u(k)$ does not affect the dynamics, but only the system output $y_0(k)$ via direct feedthrough. The Main System Dynamics block is driven by the external excitation signal $w(k)$. The Main System Output block is coupled with the Subsystem via the variables $y(k)$ and $u(k)$.

The System Model part consists of the Main System Model and the Subsystem Model. The Main System Model block is assumed to be identical to the Main System block of the True System with the exception that there may be initialization errors in the states. The Subsystem Model block, on the other hand, has the same form as the Subsystem block in the True System, but its parameters are unknown.

Note that the input and output of the Subsystem are not directly measurable; i.e.,

the Subsystem is inaccessible. Instead, the output error $z(k) = \hat{y}_0(k) - y_0(k)$ is used to estimate the Subsystem parameters; hence, this is an inaccessible subsystem identification problem. The goal of the algorithm is to identify the unknown Subsystem under the presence of the Main System state estimation error $\hat{x}(k) - x(k)$.

4.2.2 The System

The equations of the Main System are

$$x(k+1) = Ax(k) + Fw(k), \quad (4.1)$$

$$y(k) = Cx(k) + Du(k) + Jw(k), \quad (4.2)$$

$$y_0(k) = E_1x(k) + E_2u(k) + E_3w(k), \quad (4.3)$$

whereas the Subsystem is described by the equation

$$u(k) = \theta y(k), \quad (4.4)$$

where the parameter θ is unknown.

The features of this framework that are important for the context of this work are as follows:

1. There is no feedback from the Subsystem output, $u(k)$, into the Main System Dynamics. This architecture is motivated by the battery health problem where the health subsystem in a battery has a negligible impact on the SOC dynamics (i.e., Main System Dynamics).
2. The output $y_0(k)$ is a function of the Main System state $x(k)$ and the Subsystem output $u(k)$. This is motivated by the approximation in battery health problem that the effect of the health subsystem on the terminal voltage can be considered as a direct feedthrough.
3. The Main System is marginally stable where matrix A is diagonal with at least one eigenvalue being 1. This property is due to the battery being an energy

storage device.

4.2.3 Estimation Setup

It is assumed that the Main System is known and can be modeled accurately. Hence, the Main System Model is described by the following set of equations:

$$\hat{x}(k+1) = A\hat{x}(k) + Fw(k), \quad (4.5)$$

$$\hat{y}(k) = C\hat{x}(k) + D\hat{u}(k) + Jw(k), \quad (4.6)$$

$$\hat{y}_0(k) = E_1\hat{x}(k) + E_2\hat{u}(k) + E_3w(k), \quad (4.7)$$

The Subsystem Model is assumed to have the same form as (4.4), but with an unknown parameter; i.e.,

$$\hat{u}(k) = \hat{\theta}(k)\hat{y}(k). \quad (4.8)$$

Therefore, the goal is to estimate the true Subsystem parameter θ with $\hat{\theta}(k)$ so that the Subsystem output $u(k)$ can be estimated.

Estimating θ and $u(k)$ with $\hat{\theta}$ using the structure of Figure 4.1 is a challenge due to two reasons:

1. Due to the features 1) and 3) above, the main system state error $\hat{x}(k) - x(k)$ is persistent, which affects the estimation of $u(k)$.
2. Due to the feature 2), the difference $z(k) = \hat{y}_0(k) - y_0(k)$ can be caused by either the difference between $\hat{u}(k)$ and $u(k)$ or the state difference $\hat{x}(k) - x(k)$. The unique determination of $u(k)$ from only the measurement of $y_0(k)$ is not possible given that $x(k)$ is not measured.

These difficulties make the estimation of θ using RCSI challenging under the presence of main system state error. Hence, a new approach is described below.

4.2.4 The Two-Step Filter

Assume that $A \in R^{n \times n}$ is organized as

$$A = \begin{bmatrix} I_m & 0 \\ 0 & \Lambda \end{bmatrix} \quad (4.9)$$

where I_m represents the identity matrix of dimension m ($m \leq n$) and

$$\Lambda = \begin{bmatrix} \lambda_1 & & & \\ & \lambda_2 & & \\ & & \ddots & \\ & & & \lambda_{n-m} \end{bmatrix} \quad (4.10)$$

with $\lambda_i < 1$ for all i .

The main system state vector is $x = [x_1(k) \ \cdots \ x_n(k)]^T$ where the states x_1, x_2, \dots, x_m are such that their initialization errors are persistent. Define the persistent state vectors $\zeta(k)$ and $\hat{\zeta}(k)$ as

$$\zeta \triangleq [x_1 \ \cdots \ x_m]^T, \quad (4.11)$$

$$\hat{\zeta} \triangleq [\hat{x}_1 \ \cdots \ \hat{x}_m]^T. \quad (4.12)$$

Let d represent the constant main system state difference vector,

$$d \triangleq \hat{\zeta}(k) - \zeta(k) = \begin{bmatrix} \hat{x}_1(k) - x_1(k) \\ \vdots \\ \hat{x}_m(k) - x_m(k) \end{bmatrix} \in \mathbf{R}^m. \quad (4.13)$$

Let \mathcal{E}_1 and \mathcal{C} consist of the elements of E_1 and C , respectively, that correspond to the persistent states:

$$\mathcal{E}_1 \triangleq \begin{bmatrix} E_{1,1} & \cdots & E_{1,m} \end{bmatrix} \in \mathbf{R}^{l_{y_0} \times m}, \quad (4.14)$$

$$\mathcal{C} \triangleq \begin{bmatrix} C_1 & \cdots & C_m \end{bmatrix} \in \mathbf{R}^{l_y \times m}. \quad (4.15)$$

where l_{y_0} and l_y are the length of y_0 and y , respectively.

4.2.4.1 The First Step

Assume that the initial estimation errors in all the asymptotically stable main system states diminish when time step is larger than a constant T . For any $k > T$, the error $z(k)$ is expressed as a function of $u(k)$, $\hat{u}(k)$ and d :

$$\begin{aligned} z(k) &= \hat{y}_0(k) - y_0(k) \\ &= \mathcal{E}_1 \left[\hat{\zeta}(k) - \zeta(k) \right] + E_2 [\hat{u}(k) - u(k)] \\ &= \mathcal{E}_1 d + E_2 [\hat{u}(k) - u(k)]. \end{aligned} \quad (4.16)$$

Next, a cost function is formulated:

$$J(u^s(k)) = z^{s\text{T}}(k) R_z z^s(k) + u^{s\text{T}}(k) R_u u^s(k), \quad (4.17)$$

where R_z and R_u are tunable positive semi-definite weights; the substituted $z(k)$, $z^s(k)$, is defined such that $\hat{u}(k)$ in $z(k)$ is replaced by any substitute $u^s(k)$,

$$z^s(k) \triangleq z(k) - \mathcal{E}_1 d - E_2 \hat{u}(k) + E_2 u^s(k). \quad (4.18)$$

The optimal u , $u^*(k)$, is defined to be the minimizer of $J(u^s(k))$. When $R_u = 0$, the minimizer of $J(u^s(k))$ also minimizes $z^s(k)$ given that the effect of d in $z(k)$ is not compensated by $u^*(k)$. Let $z^*(k)$ denote the $z^s(k)$ that corresponds to $u^*(k)$;

i.e.,

$$z^*(k) = z(k) - \mathcal{E}_1 d - E_2 \hat{u}(k) + E_2 u^*(k). \quad (4.19)$$

Substitute (4.18) into (4.17) and find $u^*(k)$:

$$\begin{aligned} \frac{\partial J}{\partial u^s} \Big|_{u^s=u^*(k)} &= 2u^{*\top}(k) (E_2^\top R_z E_2 + R_u) + \\ &2(z(k) - \mathcal{E}_1 d - E_2 \hat{u}(k))^\top R_z E_2 = 0. \end{aligned} \quad (4.20)$$

Note that $z(k) \in \mathbf{R}^{l_{y_0}}$ and $E_2^\top R_z E_2 + R_u$ is symmetric.

The solution to (4.20) is

$$\begin{aligned} u^*(k) &= - (E_2^\top R_z E_2 + R_u)^{-1} E_2^\top R_z \\ &[z(k) - \mathcal{E}_1 d - E_2 \hat{u}(k)]. \end{aligned} \quad (4.21)$$

The terms that can be constructed from the measurable signal $z(k)$ and estimated signal $\hat{u}(k)$ are lumped into the variable $\tilde{u}(k)$:

$$\begin{aligned} \tilde{u}(k) &\triangleq - (E_2^\top R_z E_2 + R_u)^{-1} E_2^\top R_z \\ &[z(k) - E_2 \hat{u}(k)]. \end{aligned} \quad (4.22)$$

Therefore,

$$\tilde{u}(k) = u^*(k) - (E_2^\top R_z E_2 + R_u)^{-1} E_2^\top R_z \mathcal{E}_1 d. \quad (4.23)$$

The goal of the first step is to calculate $\tilde{u}(k)$ from $z(k)$ and $\hat{u}(k)$ as in (4.22).

4.2.4.2 The Second Step

Ideally it is desired that $z^*(k)$ converges to zero. By substituting (4.16) into (4.19), it can be shown that $u^*(k) = u(k)$ when $z^*(k) = 0$. Therefore, $u^*(k)$ in (4.23) can

be constructed as

$$u^*(k) = \theta y(k). \quad (4.24)$$

For $k > T$, express $y(k)$ using the estimated signals $\hat{y}(k)$ and $\hat{u}(k)$:

$$\begin{aligned} y(k) &= Cx(k) + Du(k) + Jw(k) \\ &= \hat{y}(k) - \mathcal{C}d - D(\hat{u}(k) - u(k)) \\ &= [\hat{y}(k) - D\hat{u}(k)] - \mathcal{C}d + D\theta y(k). \end{aligned} \quad (4.25)$$

Therefore,

$$\begin{aligned} y(k) &= (I_{l_y} - D\theta)^{-1} [\hat{y}(k) - D\hat{u}(k)] \\ &\quad - (I_{l_y} - D\theta)^{-1} \mathcal{C}d. \end{aligned} \quad (4.26)$$

Substitute (4.24) and (4.26) into (4.23) to obtain

$$\begin{aligned} \tilde{u}(k) &= \theta (I_{l_y} - D\theta)^{-1} (\hat{y}(k) - D\hat{u}(k)) \\ &\quad - \theta (I_{l_y} - D\theta)^{-1} \mathcal{C}d \\ &\quad - (E_2^T R_z E_2 + R_u)^{-1} E_2^T R_z \mathcal{E}_1 d. \end{aligned} \quad (4.27)$$

(4.27) constructs $\tilde{u}(k)$ with the unknown parameters θ and d . Now, any nonlinear estimation method can be used to estimate θ and d from $\tilde{u}(k)$ calculated in the first step. In this paper, the Modified Extended Kalman Filter (MEKF) [70] is used in the second step to estimate θ and d .

When the subsystem is SISO and only one of the eigenvalues of A is 1, the MEKF algorithm for (4.27) is as presented below.

Define the parameter vector as $\omega \triangleq \begin{bmatrix} \theta & d \end{bmatrix}^T$. The estimation of the parameter vector is defined to be $\hat{\omega}(k) \triangleq \begin{bmatrix} \hat{\theta}(k) & \hat{d}(k) \end{bmatrix}^T$. Let $P(k)$ be the covariance matrix

of $\hat{\omega}(k)$. Then,

$$\hat{\omega}(k+1) = \hat{\omega}(k) + K(k) \left[\tilde{u}(k) - \hat{u}(\hat{\omega}(k)) \right], \quad (4.28)$$

$$P(k+1) = (\alpha + 1) [P(k) - K(k) H(k) P(k) + Q(k)], \quad (4.29)$$

where

$$\begin{aligned} \hat{u}(\hat{\omega}(k)) &= \frac{\hat{\theta}(k)}{1 - D\hat{\theta}(k)} (\hat{y}(k) - D\hat{u}(k)) - \mathcal{C} \frac{\hat{\theta}(k)\hat{d}(k)}{1 - D\hat{\theta}(k)} \\ &\quad - (E_2^T R_z E_2 + R_u)^{-1} E_2^T R_z \mathcal{E}_1 \hat{d}(k), \end{aligned} \quad (4.30)$$

$$\begin{aligned} H(k) &= \left. \frac{\partial \tilde{u}(\omega)}{\partial \omega} \right|_{\omega=\hat{\omega}(k)} \\ &= \begin{bmatrix} \frac{1}{(1-D\hat{\theta}(k))^2} (\hat{y}(k) - D\hat{u}(k) - \mathcal{C}\hat{d}(k)) \\ -\frac{\mathcal{C}\hat{\theta}(k)}{1-D\hat{\theta}(k)} - (E_2^T R_z E_2 + R_u)^{-1} E_2^T R_z \mathcal{E}_1 \end{bmatrix}^T, \end{aligned} \quad (4.31)$$

$$K(k) = P(k) H^T(k) (H(k) P(k) H^T(k) + R_t(k))^{-1}. \quad (4.32)$$

$Q(k)$ is the process noise covariance matrix. $R_t(k)$ is the output noise covariance matrix. $\alpha \in [0, 1]$ acts like a forgetting factor with $\alpha + 1 = \frac{1}{\lambda}$ where λ is the forgetting factor.

4.2.5 Estimation of the Subsystem Output

Because there is a persistent difference between $\hat{x}(k)$ and $x(k)$, the input to the subsystem model $\hat{y}(k)$ will not converge to the true subsystem input $y(k)$. Therefore, even when $\hat{\theta}(k)$ converges to θ , the output of the subsystem model $\hat{u}(k)$ will not converge to the subsystem output $u(k)$ unless a correction based on $\hat{d}(k)$ is introduced.

To estimate the subsystem output $u(k)$, $\hat{y}(k)$ should be corrected with $\hat{d}(k)$. Let $\hat{u}'(k)$ and $\hat{y}'(k)$ denote the corrected estimates of the subsystem output $u(k)$ and subsystem input $y(k)$, respectively, which can be derived as follows.

The difference between $\hat{y}(k)$ and $y(k)$ is given as

$$\begin{aligned}\hat{y}(k) - y(k) &= \mathcal{C}d + D(\hat{u}(k) - u(k)) \\ &= \mathcal{C}d + D\left(\hat{\theta}(k)\hat{y}(k) - \theta y(k)\right)\end{aligned}\quad (4.33)$$

Solving for $y(k)$ yields

$$y(k) = (I_{l_y} - D\theta)^{-1} \left[(\hat{y}(k) - \mathcal{C}d) - D\hat{\theta}(k)\hat{y}(k) \right]. \quad (4.34)$$

Replacing d and θ with their estimates \hat{d} and $\hat{\theta}$, we obtain

$$\hat{y}'(k) = \hat{y}(k) - (I_{l_y} - D\hat{\theta}(k))^{-1} \mathcal{C}\hat{d}(k). \quad (4.35)$$

Then,

$$\begin{aligned}\hat{u}'(k) &= \hat{\theta}\hat{y}'(k) \\ &= \hat{\theta}(k) \left[\hat{y}(k) - (I_{l_y} - D\hat{\theta}(k))^{-1} \mathcal{C}\hat{d}(k) \right].\end{aligned}\quad (4.36)$$

4.3 Application to Estimation of Side Reaction Current Density

4.3.1 Modified Battery Model

The goal of this section is to find a model structure that is suitable as the System Model in estimation of the side reaction current density. To achieve this goal, the SPM presented in Section 2.2.2 is first modified so that i) the feedback of the side reaction current density to the charge and discharge dynamics is removed, and ii) only one eigenvalue of the dynamics of the model is 1. This modification can significantly simplify the application of the TSF in estimation of side reaction current density. Then the modified SPM is augmented with the SOH model to serve as the System Model.

First, because the feedback of the side reaction current density to the battery charge and discharge dynamics is negligible compared with the influence of the external input, namely the current, the term $Bu(k)$ in (2.50) can be removed.

Then, to minimize the number of the eigenvalues that are 1, the SPM is modified by removing the state equation for the solid concentration in the cathode and computing $c_{\text{se,p}}$ using $c_{\text{se,n}}$ and the number of cyclable Li-ions instead. In this modification, the distribution of Li-ion concentration inside the particles is assumed to be uniform for every instant. Even though solid Li-ion concentration is not always uniformly distributed in practice, the assumption of uniform distribution is a valid approximation when the C-rate is low to allow enough time for the diffusion of Li-ions inside particles. Under this approximation, (2.41) is modified into

$$n_{\text{Li}} = \epsilon_{\text{s,p}} L_p A c_{\text{s,max,p}} \theta_p(k) + \epsilon_{\text{s,n}} L_n A c_{\text{s,max,n}} \theta_n(k), \quad (4.37)$$

and thus $c_{\text{se,p}}(k)$ can be computed from

$$\theta_p(k) = \frac{n_{\text{Li}}(k) - \epsilon_{\text{s,n}} L_n A c_{\text{s,max,n}} \theta_n(k)}{\epsilon_{\text{s,p}} L_p A c_{\text{s,max,p}}}. \quad (4.38)$$

Therefore, the state space model of the SPM in this chapter is modified from (2.50) – (2.52) into

$$x(k+1) = Ax(k) + FI(k), \quad (4.39)$$

$$V(k) = g_0(x(k), I(k)), \quad (4.40)$$

where A and F are obtained from (2.42) for the anode, and $g_0(\cdot)$ represents (2.48) where $c_{\text{se,p}}$ is obtained from (4.38). Therefore, under the second-order Padé approximation, $x(k) = \begin{bmatrix} x_1 & x_2 \end{bmatrix}^T \in \mathbf{R}^2$ and A is diagonal with the eigenvalue associated with the first state being 1. There is no term containing the subsystem output $u(k)$ in (4.39). Hence, the initialization error in the first state is persistent. Furthermore, the system presented in (4.39) and (4.40) have the same form as the System Model in Figure 4.1.

Therefore, the nonlinear battery model, including the modified SPM and the SOH model, can be written as

$$x(k+1) = Ax(k) + FI(k), \quad (4.41)$$

$$y(k) = g(x(k), J_{\text{sd}}(k), I(k)), \quad (4.42)$$

$$V(k) = g_0(x(k), J_{\text{sd}}(k), I(k)), \quad (4.43)$$

$$J_{\text{sd}}(k) = \theta y(k). \quad (4.44)$$

In this section, the parameters of the model are obtained from [3], which identifies parameters of an HEV battery that is of the LMO-mixture chemistry. The technique developed in this section is also applicable to other parameter values for other battery chemistries.

4.3.2 Application on Time Varying Linearized Battery Model

In this section, the TSF is applied in a time varying linearization of the modified SPM to estimate the side reaction current density, subsystem parameter and the persistent main system state error that pertain to SOC estimation error. Although this time varying linear battery model is far from sufficient in representing the battery dynamics, this section serves as a preparation for the next section in discussion of application of the TSF in nonlinear battery model.

In this section, the True System is

$$x(k+1) = Ax(k) + FI(k), \quad (4.45)$$

$$y(k) = C(k)x(k) + D(k)J_{\text{sd}}(k) + J(k)I(k), \quad (4.46)$$

$$V(k) = E_1(k)x(k) + E_2(k)J_{\text{sd}}(k) + E_3(k)I(k), \quad (4.47)$$

$$J_{\text{sd}}(k) = \theta y(k), \quad (4.48)$$

where (4.45) is (4.41), and (4.46) – (4.48) are linearization of (4.42) – (4.44) around

$x(k)$, $I(k)$, and $J_{\text{sd}}(k)$. Therefore,

$$C(k) = \left. \frac{\partial g(x, J_{\text{sd}}, I)}{\partial x} \right|_{x=x(k), I=I(k), J_{\text{sd}}=J_{\text{sd}}(k)}, \quad (4.49)$$

$$D(k) = \left. \frac{\partial g(x, J_{\text{sd}}, I)}{\partial J_{\text{sd}}} \right|_{x=x(k), I=I(k), J_{\text{sd}}=J_{\text{sd}}(k)}, \quad (4.50)$$

$$J(k) = \left. \frac{\partial g(x, J_{\text{sd}}, I)}{\partial I} \right|_{x=x(k), I=I(k), J_{\text{sd}}=J_{\text{sd}}(k)}, \quad (4.51)$$

$$E_1(k) = \left. \frac{\partial g_0(x, J_{\text{sd}}, I)}{\partial x} \right|_{x=x(k), I=I(k), J_{\text{sd}}=J_{\text{sd}}(k)}, \quad (4.52)$$

$$E_2(k) = \left. \frac{\partial g_0(x, J_{\text{sd}}, I)}{\partial J_{\text{sd}}} \right|_{x=x(k), I=I(k), J_{\text{sd}}=J_{\text{sd}}(k)}, \quad (4.53)$$

$$E_3(k) = \left. \frac{\partial g_0(x, J_{\text{sd}}, I)}{\partial I} \right|_{x=x(k), I=I(k), J_{\text{sd}}=J_{\text{sd}}(k)}. \quad (4.54)$$

Then, the System Model is

$$\hat{x}(k+1) = A\hat{x}(k) + FI(k), \quad (4.55)$$

$$\hat{y}(k) = C(k)\hat{x}(k) + D(k)\hat{J}_{\text{sd}}(k) + J(k)I(k), \quad (4.56)$$

$$\hat{V}(k) = E_1(k)\hat{x}(k) + E_2(k)\hat{J}_{\text{sd}}(k) + E_3(k)I(k), \quad (4.57)$$

$$\hat{J}_{\text{sd}}(k) = \hat{\theta}(k)\hat{y}(k). \quad (4.58)$$

The matrices $C(k)$, $D(k)$, $J(k)$, $E_1(k)$, $E_2(k)$, and $E_3(k)$ are also used as the matrices C , D , J , E_1 , E_2 , and E_3 in the TSF. It is shown in (2.44) that only the first state corresponds to eigenvalue 1, $d = \hat{x}_1(1) - x_1(1)$, and thus the parameter vector in the TSF is $\omega = [\theta \ d]^T$.

The Main System state is initialized at $x(1) = \begin{bmatrix} -1.6218 \times 10^{10} & 0 \end{bmatrix}^T$. This state corresponds to 0% SOC, which is the same SOC level as in Chapter 3. The Main System Model state is initialized at $\hat{x}(1) = \begin{bmatrix} -1.6926 \times 10^{10} & 0 \end{bmatrix}^T$. This state corresponds to 1% SOC, and thus there is 1% SOC error between the True System and the System Model. Therefore, $d = \hat{x}_1(1) - x_1(1) = -7.0793 \times 10^8$, which is due to the 1% SOC error. The input to the system is 1-C constant current, which simulates the fast charge of EVs.

The estimated parameter vector with the TSF is initialized at $\hat{\omega}(1) = [\hat{\theta}(1) \quad \hat{d}(1)]^T = [0 \quad 0]^T$. The parameters in the TSF are set as follows: the weights in the cost function of the first step are set to be $R_z = I_1$ and $R_u = 0$; the initial covariance matrix is set to be $P_0 = 10^3 I_2$; the parameters in the MEKF are set to be $Q(k) = 10I_2$, $R_t(k) = I_1$ and $\alpha = 0.01$.

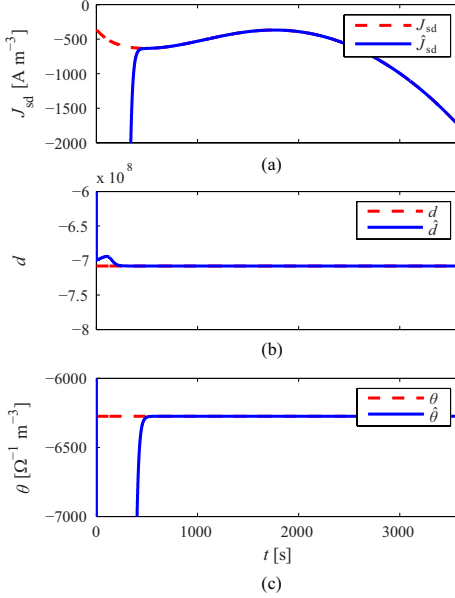


Figure 4.2: The estimates of the side reaction current density J_{sd} , the Main system state error d , and the subsystem parameter θ in the time-varying linearized battery model using the two-step filter.

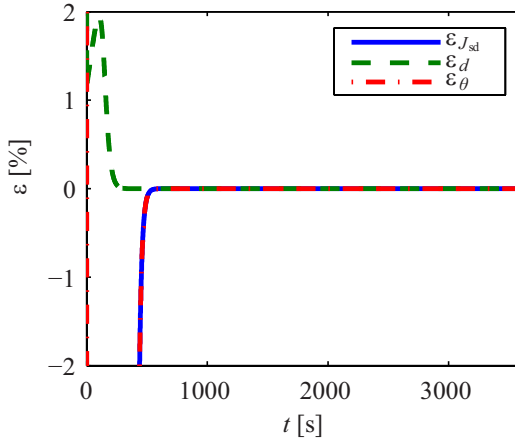


Figure 4.3: The relative estimation errors of the side reaction current density J_{sd} , the Main system state error d , and the subsystem parameter θ in the time-varying linearized battery model using the two-step filter.

Figure 4.2 shows the estimates of the side reaction current density J_{sd} , the Main system state error d , and the subsystem parameter θ in the time-varying linearized battery model using the TSF. All three estimates converge to their true values in 600 seconds. Figure 4.3 shows the relative estimation errors, $\epsilon_{J_{\text{sd}}}$, ϵ_d , and ϵ_θ , in the time-varying linearized battery model. All the relative estimation errors converge to 0 after 600 seconds. This result shows that the TSF can estimate both the side reaction current density and the state error caused by the SOC estimation error in a time varying linearized battery model.

4.3.3 Application on Nonlinear Battery Model

In this section, the TSF is applied to the nonlinear battery, which contains the SPM and the SOH model, to estimate the side reaction current density under the presence of SOC estimation error. Both the True System and System Model are the nonlinear SPM with the SOH model.

Because the TSF is developed under linear discrete context, when the TSF is applied to the nonlinear system, the matrices C , D , J , E_1 , E_2 , and E_3 are obtained through linearization. Define

$$\hat{C}(k) \triangleq \left. \frac{\partial g(x, J_{\text{sd}}, I)}{\partial x} \right|_{x=\hat{x}(k), I=I(k), J_{\text{sd}}=\hat{J}_{\text{sd}}(k)}, \quad (4.59)$$

$$\hat{D}(k) \triangleq \left. \frac{\partial g(x, J_{\text{sd}}, I)}{\partial J_{\text{sd}}} \right|_{x=\hat{x}(k), I=I(k), J_{\text{sd}}=\hat{J}_{\text{sd}}(k)}, \quad (4.60)$$

$$\hat{J}(k) \triangleq \left. \frac{\partial g(x, J_{\text{sd}}, I)}{\partial I} \right|_{x=\hat{x}(k), I=I(k), J_{\text{sd}}=\hat{J}_{\text{sd}}(k)}, \quad (4.61)$$

$$\hat{E}_1(k) \triangleq \left. \frac{\partial g_0(x, J_{\text{sd}}, I)}{\partial x} \right|_{x=\hat{x}(k), I=I(k), J_{\text{sd}}=\hat{J}_{\text{sd}}(k)}, \quad (4.62)$$

$$\hat{E}_2(k) \triangleq \left. \frac{\partial g_0(x, J_{\text{sd}}, I)}{\partial J_{\text{sd}}} \right|_{x=\hat{x}(k), I=I(k), J_{\text{sd}}=\hat{J}_{\text{sd}}(k)}, \quad (4.63)$$

$$\hat{E}_3(k) \triangleq \left. \frac{\partial g_0(x, J_{\text{sd}}, I)}{\partial I} \right|_{x=\hat{x}(k), I=I(k), J_{\text{sd}}=\hat{J}_{\text{sd}}(k)}. \quad (4.64)$$

Then $\hat{C}(k)$, $\hat{D}(k)$, $\hat{J}(k)$, $\hat{E}_1(k)$, $\hat{E}_2(k)$, and $\hat{E}_3(k)$ are used as the matrices C , D , J , E_1 , E_2 , and E_3 in the TSF.

As in Section 4.3.2, the Main System state is initialized at 0% SOC while the Main System Model state is initialized at 1% SOC to introduce 1% initial SOC estimation error. The true parameter vector is defined as $\omega(1) = [\theta \ d]^T$. The estimated parameter vector with the TSF is initialized at $\hat{\omega}(1) = [\hat{\theta}(1) \ \hat{d}(1)]^T = [0 \ 0]^T$. The parameters in the TSF are set as follows: the weights in the cost function of the first step are set to be $R_z = I_1$ and $R_u = 0$; the initial covariance matrix is set to be $P_0 = 10^3 I_2$; the parameters in the MEKF are set to be $Q(k) = 10I_2$, $R_t(k) = I_1$ and $\alpha = 0.01$. The input is 1-C constant current.

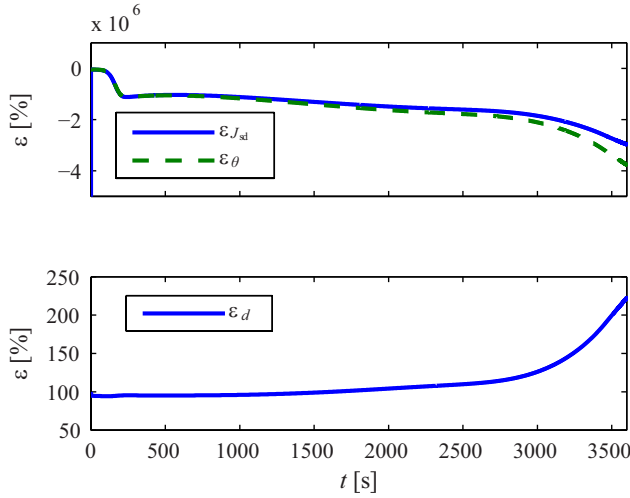


Figure 4.4: The relative estimation errors of the side reaction current density ($\epsilon_{J_{sd}}$), the subsystem parameter (ϵ_θ), and the Main system state error (ϵ_d) in the nonlinear battery model using the two-step filter.

Figure 4.4 shows the relative estimation errors, $\epsilon_{J_{sd}}$, ϵ_θ , and ϵ_d , in the nonlinear battery model using the TSF. It can be seen that both $\epsilon_{J_{sd}}$ and ϵ_θ are on the order of $10^6\%$, and ϵ_d is on the order of 100%. This result indicates that the TSF with matrices obtained by linearization cannot estimate the side reaction current density J_{sd} accurately under 1% SOC estimation error. Furthermore, in the first 2500 s, ϵ_d remains very close to the 100%, which corresponds to the initial estimate. This means that the estimate of the Main system state error d adapts only slightly and \hat{d} remains close to 0 during the first 2500 s. It is only during the last 1100 s that ϵ_d grows rapidly until 222%. This result indicates that the TSF is not working as expected to

reduce estimation errors of \hat{J}_{sd} and $\hat{\theta}$ by estimating d . Without adaptation of \hat{d} , the TSF should give similar estimation errors of \hat{J}_{sd} and $\hat{\theta}$ as using the RCSI, which has no mechanism to adapt d in this situation.

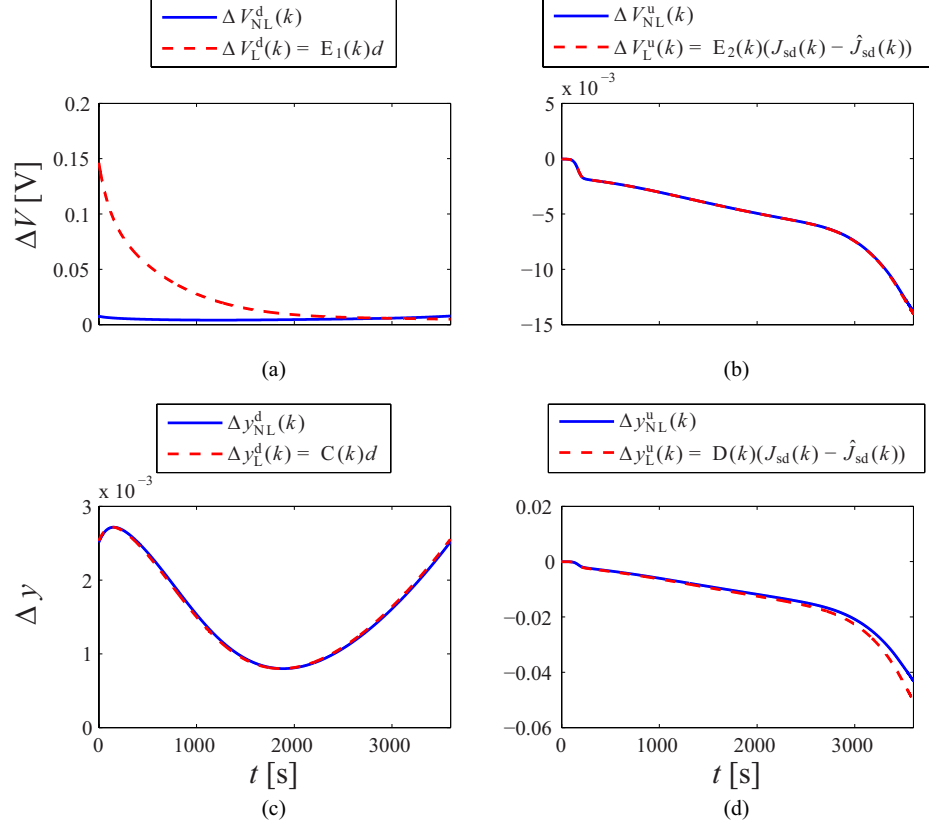


Figure 4.5: The comparison between (a) $\Delta V_{\text{NL}}^{\text{d}}(k)$ and $\Delta V_{\text{L}}^{\text{d}}(k)$, (b) $\Delta V_{\text{NL}}^{\text{u}}(k)$ and $\Delta V_{\text{L}}^{\text{u}}(k)$, (c) $\Delta y_{\text{NL}}^{\text{d}}(k)$ and $\Delta y_{\text{L}}^{\text{d}}(k)$, and (d) $\Delta y_{\text{NL}}^{\text{u}}(k)$ and $\Delta y_{\text{L}}^{\text{u}}(k)$.

The large estimation errors in Figure 4.4 are caused by the inaccurate approximation of the nonlinear voltage function with linearization. Specifically, the matrix E_1 , which indicates the sensitivity of the output voltage $V(k)$ to the state $x(k)$, cannot be accurately evaluated by $E_1(k)$ in (4.52), and thus not by $\hat{E}_1(k)$, which is an

approximation of $E_1(k)$. To compare the nonlinear model and the linearization, define

$$\Delta V_{\text{NL}}^{\text{d}}(k) = V_{\hat{x}, J_{\text{sd}}}(k) - V_{x, J_{\text{sd}}}(k), \quad (4.65)$$

$$\Delta V_{\text{L}}^{\text{d}}(k) = E_1(k)d, \quad (4.66)$$

$$\Delta V_{\text{NL}}^{\text{u}}(k) = V_{x, \hat{J}_{\text{sd}}}(k) - V_{x, J_{\text{sd}}}(k), \quad (4.67)$$

$$\Delta V_{\text{L}}^{\text{u}}(k) = E_2(k)(\hat{J}_{\text{sd}}(k) - J_{\text{sd}}(k)), \quad (4.68)$$

$$\Delta y_{\text{NL}}^{\text{d}}(k) = y_{\hat{x}, J_{\text{sd}}}(k) - y_{x, J_{\text{sd}}}(k), \quad (4.69)$$

$$\Delta y_{\text{L}}^{\text{d}}(k) = C(k)d, \quad (4.70)$$

$$\Delta y_{\text{NL}}^{\text{u}}(k) = y_{x, \hat{J}_{\text{sd}}}(k) - y_{x, J_{\text{sd}}}(k), \quad (4.71)$$

$$\Delta y_{\text{L}}^{\text{u}}(k) = D(k)(\hat{J}_{\text{sd}}(k) - J_{\text{sd}}(k)), \quad (4.72)$$

where $x(k)$ and $J_{\text{sd}}(k)$ indicate the state and side reaction current density in the True System in the example shown in Figure 4.4, respectively. $\hat{x}(k)$ and $\hat{J}_{\text{sd}}(k)$ indicate the state and side reaction current density in the System Model in the example shown in Figure 4.4, respectively. $V_{i,j}(k)$ is the voltage response of the nonlinear battery model whose trajectories of the state and side reaction current density follow the trajectories of i and j , respectively. $y_{i,j}(k)$ is the input to subsystem y of the nonlinear battery model whose trajectories of the state and side reaction current density follow the trajectories of i and j , respectively. $C(k)$, $D(k)$, $E_1(k)$, and $E_2(k)$ are defined in (4.49), (4.50), (4.52), and (4.53), respectively. Therefore, how well the trajectory of $\Delta V_{\text{L}}(k)$ and $\Delta y_{\text{L}}(k)$ match the trajectory of $\Delta V_{\text{NL}}(k)$ and $\Delta y_{\text{NL}}(k)$ with the same superscripts, respectively, shows how accurate the linearization approximates the nonlinearity of the outputs $V(k)$ and $y(k)$. Specifically, the pair $\Delta V_{\text{NL}}^{\text{d}}(k)$ and $\Delta V_{\text{L}}^{\text{d}}(k)$ indicates the accuracy of using $E_1(k)$ to evaluate the sensitivity of the output voltage $V(k)$ to $x(k)$, the pair $\Delta V_{\text{NL}}^{\text{u}}(k)$ and $\Delta V_{\text{L}}^{\text{u}}(k)$ indicates the accuracy of using $E_2(k)$ to evaluate the sensitivity of the output voltage $V(k)$ to $J_{\text{sd}}(k)$, the pair $\Delta y_{\text{NL}}^{\text{d}}(k)$ and $\Delta y_{\text{L}}^{\text{d}}(k)$ indicates the accuracy of using $E_1(k)$ to evaluate the sensitivity of $y(k)$ to $x(k)$, and the pair $\Delta y_{\text{NL}}^{\text{u}}(k)$ and $\Delta y_{\text{L}}^{\text{u}}(k)$ indicates the accuracy of using $E_2(k)$ to evaluate the sensitivity of $y(k)$ to $J_{\text{sd}}(k)$.

Figure 4.5 compares (a) $\Delta V_{\text{NL}}^{\text{d}}(k)$ and $\Delta V_{\text{L}}^{\text{d}}(k)$, (b) $\Delta V_{\text{NL}}^{\text{u}}(k)$ and $\Delta V_{\text{L}}^{\text{u}}(k)$, (c) $\Delta y_{\text{NL}}^{\text{d}}(k)$ and $\Delta y_{\text{L}}^{\text{d}}(k)$, and (d) $\Delta y_{\text{NL}}^{\text{u}}(k)$ and $\Delta y_{\text{L}}^{\text{u}}(k)$. It can be observed from Figure 4.5 that the trajectories of (b) $\Delta V_{\text{NL}}^{\text{u}}(k)$ and $\Delta V_{\text{L}}^{\text{u}}(k)$, (c) $\Delta y_{\text{NL}}^{\text{d}}(k)$ and $\Delta y_{\text{L}}^{\text{d}}(k)$, and (d) $\Delta y_{\text{NL}}^{\text{u}}(k)$ and $\Delta y_{\text{L}}^{\text{u}}(k)$ match well with each other, which indicates that $E_2(k)$, $C(k)$, and $D(k)$ can evaluate the sensitivities accurately. On the other hand, $\Delta V_{\text{L}}^{\text{d}}(k)$ is significantly larger than $\Delta V_{\text{NL}}^{\text{d}}(k)$ before 2500 s. This means that linearization significantly overestimates the sensitivity of the output voltage $V(k)$ to $x(k)$ before 2500 s.

In estimation, because the true $x(k)$ and $J_{\text{sd}}(k)$ are unknown, $\hat{C}(k) - \hat{E}_2(k)$ are used to approximate $C(k) - E_2(k)$. Because $\hat{C}(k) - \hat{E}_2(k)$ are obtained by linearizing the nonlinear functions around the estimates, they are only an approximation of the sensitivities at the true operating point. Therefore, it is expected that evaluating the sensitivities using $\hat{C}(k) - \hat{E}_2(k)$ is less accurate than using $C(k) - E_2(k)$. Hence, it can be concluded that it is inaccurate to evaluating the sensitivity of the output voltage $V(k)$ to $x(k)$ using $\hat{E}_1(k)$.

The overestimation observed in Figure 4.5 agrees with the behavior observed for ϵ_d in Figure 4.4. Because linearization significantly overestimates the sensitivity of the output voltage $V(k)$ to $x(k)$ before 2500 s, the estimate $\hat{d}(k)$ is expected to be significantly smaller than the true d during the same range, which is in accordance with to the close to 100% ϵ_d that corresponds to small adaptation of $\hat{d}(k)$ before 2500 s observed in Figure 4.4.

This overestimation also explains the large estimation errors for the side reaction current density and the subsystem parameter. It can be concluded from Figure 4.5 (b) that the sensitivity of the voltage $V(k)$ to the side reaction current density J_{sd} can be accurately evaluated using $E_2(k)$. With the parameter set used in this chapter, E_2 is on the order of 10^{-10} and the side reaction current density J_{sd} is on the order of 10^3 A m^{-3} . Similar to the analysis in Section 3.4.1, the additional relative estimation error α_{as} caused by voltage errors introduced by additional sources V_{as} is given by

$$\alpha_{\text{as}} = V_{\text{as}} V_{J_{\text{sd}}}^{-1} = V_{\text{as}} (E_2 J_{\text{sd}})^{-1} = O(10^7 V_{\text{as}}). \quad (4.73)$$

When \hat{d} has almost no adaptation and stays close to 0, V_{as} is the voltage difference caused by the state error, namely $\Delta V_{\text{NL}}^{\text{d}}$. Figure 4.5 (a) shows that $\Delta V_{\text{NL}}^{\text{d}}$ is on the order of 10^{-3} V. Therefore, in the example in Figure 4.4,

$$\alpha_{\text{as}} = O(10^7 V_{\text{as}}) = O(10^4) = O(10^6\%). \quad (4.74)$$

This result shows that the additional relative estimation error is on the order of $10^6\%$, which agrees with $\epsilon_{J_{\text{sd}}}$ and ϵ_{θ} shown in Figure 4.4.

To show that the inaccurate evaluation of the sensitivity of the output voltage $V(k)$ to $x(k)$ using $\hat{E}_1(k)$ is the only reason for the large estimation errors shown in Figure 4.4, the estimation is performed using the same nonlinear model but with a E_1 that is directly obtained from the voltage difference. Define

$$E_{1,\text{non}}(k) \triangleq \frac{\Delta V_{\text{NL}}^{\text{d}}(k)}{d}, \quad (4.75)$$

where d is the state difference corresponds to 1% SOC estimation error as in the example shown in Figure 4.4. Then $E_{1,\text{non}}(k)$ is the sensitivity of the voltage to the state approximated directly from the nonlinear function.

Figure 4.6 shows the estimates \hat{J}_{sd} , \hat{d} , and $\hat{\theta}$ using the TSF with E_1 approximated by $E_{1,\text{non}}(k)$. The initialization of the estimates and all the parameters are set the same as in the example shown in Figure 4.4. It can be observed that all the estimates track their respective true values accurately after 500 s. This result shows that the TSF can estimate J_{sd} , d , and θ accurately if an accurate evaluation of E_1 , the sensitivity of the voltage to the state, is available.

4.3.4 Evaluating the Sensitivity of the Voltage to the States

In this section, the method to obtain an accurate evaluation of E_1 for the estimation of the side reaction current density is discussed. In particular, E_1 is evaluated with the trajectory of $E_{1,\text{non}}(k)$ defined in (4.75) that is constructed directly from the voltage responses of different initial SOC levels.

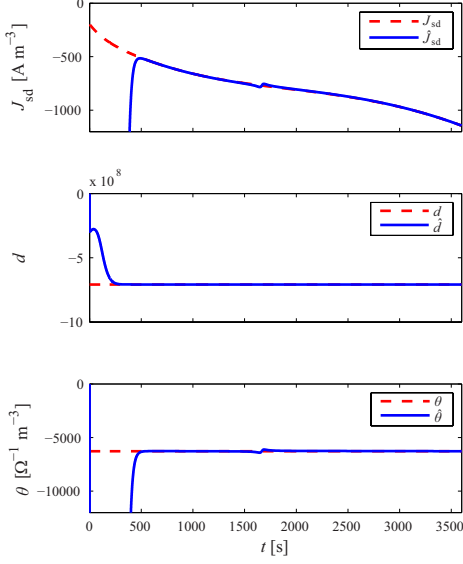


Figure 4.6: The estimates of the side reaction current density J_{sd} , the Main system state error d , and the subsystem parameter θ in the time-varying linearized battery model using the two-step filter with $E_{1,\text{non}}(k)$ approximating E_1 .

However, this method faces two challenges in practice. The first challenge is that $E_{1,\text{non}}(k)$ is a function of d , which is a function of the initial SOC estimation error. In practice, the initial SOC estimation error is unknown, and thus d is unknown. Hence, $E_{1,\text{non}}(k)$ cannot be obtained exactly. Define $E_{1,\text{non},d}(k)$ as the $E_{1,\text{non}}(k)$ that corresponds to a particular d . Notice that $\Delta V_{\text{NL}}^d(k)$ should also be obtained using the same d . Figure 4.7 (a) compares the first entry of $E_{1,\text{non},d}(k)$ obtained using d that correspond to 10%, 1%, 0.1%, and 0.01% SOC estimation errors. To better illustrate the difference in $E_{1,\text{non},d}(k)$, Figure 4.7 (b) shows the difference between the first entry of $E_{1,\text{non},d}(k)$ corresponding to 1% SOC estimation error and i) 0.1% as well as ii) 0.01% SOC estimation errors. The reason that only the first entry of $E_{1,\text{non},d}(k)$ is shown is that in estimation of the side reaction current density only the first component of $x(k)$ corresponds to eigenvalue 1, and thus only the first entry of E_1 is required in the TSF. Figure 4.7 confirms that $E_{1,\text{non},d}(k)$ changes with d .

With only the first challenge, it seems possible to approximate $E_{1,\text{non},d}(k)$ that corresponds to any d for SOC estimation errors lower than 1% with $E_{1,\text{non},d}(k)$ that corresponds to a particular d among them. As shown in Figure 4.7 (b), the differences among $E_{1,\text{non},d}(k)$ for d corresponding to 1%, 0.1%, and 0.01% SOC estimation errors

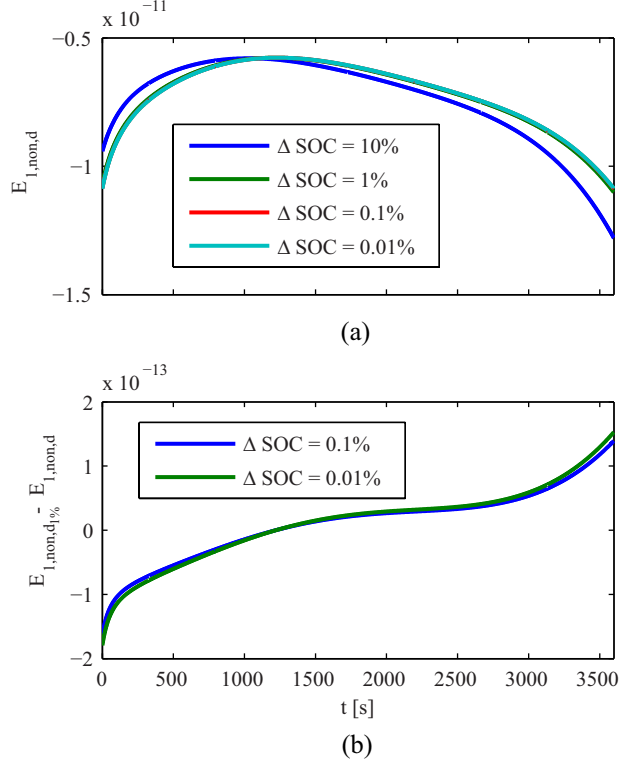


Figure 4.7: (a) The comparison between the first entry of $E_{1,\text{non},d}$ obtained using d that correspond to 10%, 1%, 0.1%, and 0.01% SOC estimation errors. (b) The difference between the first entry of $E_{1,\text{non},d}$ corresponding to 1% SOC estimation error and i) 0.1% and ii) 0.01% SOC estimation errors.

are insignificant, which is about 1% of $E_{1,\text{non},d}(k)$ for all three d . Therefore, it seems possible to simply obtain $E_{1,\text{non},d}(k)$ that corresponds to a particular d (for example $E_{1,\text{non},d}(k)$ corresponding to d that is caused by 1% SOC estimation error) and use it to approximate $E_{1,\text{non},d}(k)$ corresponding to any d for SOC estimation errors lower than 1%.

However, this possibility is invalid in presence of the second challenge with this method, which is that the accuracy for the evaluation of E_1 needs to be very high to accurately estimate the side reaction current density. It can be inferred from (4.73) that, for this particular parameter set and current profile, V_{as} has to be on the order of 10^{-8} V for α_{as} to be on the order of 10%. This required level of V_{as} is $10^{-3}\%$ of ΔV_{as} . Therefore, the error in evaluation of E_1 has to be within $\pm 10^{-3}\%$ of $E_{1,\text{non}}$ so that the relative estimation error of J_{sd} is within $\pm 10\%$. This requirement is difficult

to achieve in practice because it requires i) accurate voltage measurement and ii) accurate knowledge of d . The second requirement is especially difficult because the unknown d is the reason that the TSF, as well as the accurate evaluation of E_1 is needed.

The following simulation is to demonstrate that it is inaccurate to estimate J_{sd} , θ , and d using the TSF with E_1 approximated by $E_{1,non,d}$ corresponding to a different d than the actual d . Figure 4.8 shows $\epsilon_{J_{sd}}$, ϵ_θ , and ϵ_d obtained by approximating E_1 with $E_{1,non,d}$ corresponding to d for 0.1% SOC estimation error when the true d corresponds to 1% SOC estimation error, which is the same as in Figure 4.4 and in Figure 4.6. All the initial estimates and the parameters in the TSF are set the same as in Figure 4.4 and in Figure 4.6. It can be observed from Figure 4.8 that $\epsilon_{J_{sd}}$ and ϵ_θ are on the order of 10⁵%. These relative estimation errors are less than $\frac{1}{10}$ of the relative estimation errors shown in Figure 4.4, which corresponds to almost no adaptation of \hat{d} . This result indicates that the TSF can improve the estimation accuracy of J_{sd} and θ . However, the relative estimation errors on the order of 10⁵% is still very large. Therefore, the estimates of J_{sd} and θ are still very inaccurate even when $E_{1,non}$ used in the TSF can be approximated within $\pm 1\%$ error.

On the other hand, it can also be observed from Figure 4.8 that ϵ_d is within $\pm 12\%$ even though $\epsilon_{J_{sd}}$ and ϵ_θ are on the order of 10⁵%. This is because the sensitivity of the voltage to d is much higher than to J_{sd} . With small error in evaluating E_1 , the error in estimating d is also small, but the small error between \hat{d} and d can create a voltage difference V_{as} that is still too high to accurately estimate J_{sd} . This result shows that even when the SOC estimation error can be estimated to a reasonable accuracy by the TSF, the improvement in the accuracy of estimating J_{sd} and θ is limited.

4.3.5 Discussion

Simulation results in this chapter demonstrate that accurate estimation of the side reaction current density requires high evaluation accuracy of the sensitivity of the voltage to the SOC. It can be observed from the simulation results shown in Section 4.3.3 – 4.3.4 that J_{sd} , θ , and d can be estimated when the sensitivity to states is

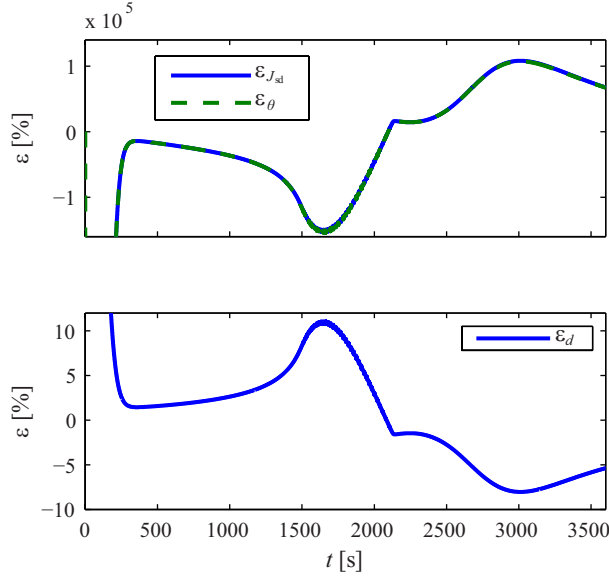


Figure 4.8: The relative estimation errors of the side reaction current density ($\epsilon_{J_{sd}}$), the subsystem parameter (ϵ_θ), and the Main system state error (ϵ_d) when E_1 in the TSF is approximated using $E_{1,\text{non},d}$ for d corresponding to 0.1% SOC estimation error while the true d corresponds to 1% SOC estimation error.

accurately evaluated in E_1 , but even an evaluation of E_1 with an error that is as small as 1% is not accurate enough to obtain a reasonable estimation accuracy for J_{sd} , θ , and d . Because the states here represent the battery SOC, it can be concluded that accurate evaluation of the sensitivity of the voltage to the SOC is required for accurate estimation of the side reaction current density using the TSF under the presence of SOC estimation errors.

This requirement on high evaluation accuracy of the sensitivity of the voltage to the SOC is caused by the low impact of J_{sd} on the voltage. As discussed in Sec. 3.4, the low impact of J_{sd} on the voltage is the reason behind large estimation errors in estimating the side reaction current density under non-ideal conditions. In Chapter 3, this low impact makes it necessary to have accurate SOC estimation. In the TSF, because the SOC estimation error is taken into account in the estimation algorithm, the requirement for accuracy is transferred from the SOC estimation to the evaluation of the sensitivity of the voltage to the SOC, namely E_1 . Obtaining highly accurate evaluation of E_1 is also difficult in practice because of the inaccurate models and measurements, as well as the unknown d . This difficulty is due to the nature of the

problem that the side reaction current density is a small value that has a limited impact on the voltage, but not due to the incapability of the algorithm or of the method to approximate E_1 . Therefore, the challenges discussed in Section 4.3.4 for approximating E_1 is the effect of the same reason behind the weak robustness observed in Sec. 3.4. Although the TSF is developed to improve the estimation accuracy of the side reaction current density under SOC estimation errors, any difficulty caused by the nature of the problem itself cannot be solved by twisting the estimation algorithm.

It can also be extrapolated from the results in this section and in Section 3.4.4 that the estimation of J_{sd} , θ , and d using the TSF with the True System being the DFN model or a real battery can be very inaccurate. The voltage difference V_{as} created by the modeling errors can i) make it very difficult to approximate E_1 accurately and ii) cause very large relative estimation errors in J_{sd} and θ . Similarly, other non-ideal conditions that can cause additional voltage difference, such as measurement noise, is also not considered in this chapter.

However, similar to the discussion in Section 3.4.5, this does not mean that the side reaction current density cannot be estimated in practice. The numerical analysis in this section is applicable only to this particular battery parameter set, with this particular cycling profile, under this particular experimental condition. The side reaction current density could still be estimated successfully in other cases with other battery parameter sets, cycling profiles, or experimental conditions as long as they can make the voltage difference V_{as} caused by inaccurate measurements, models, and approximation of E_1 below a desired bound.

4.4 Summary and Conclusions

In this chapter, a new subsystem identification algorithm, the TSF, is developed. The TSF can estimate both the subsystem parameter and the persistent main system state estimation error simultaneously for marginally stable systems as exemplified by the SOH monitoring problem in batteries when SOC estimation errors are present. In this chapter, MEKF is used in the second step as the nonlinear estimation method.

Other nonlinear estimation methods, such as the Unscented Kalman Filter (UKF) [71], can also be used as alternatives.

The TSF is applied to a battery model that is the modified SPM integrated with the Arora model to estimate the side reaction current density when SOC estimation errors are present. The TSF is first applied to a linear time varying model that is obtained via linearization of the battery model. The simulation results show that the side reaction current density, SOH subsystem model, and the SOC estimation error can be accurately estimated in the time varying linearized battery model. The TSF is then applied to the nonlinear battery model. All the matrices in the TSF except the matrix E_1 that represents the sensitivity of the voltage to the SOC are obtained through linearization around the estimates. The simulation results show that the side reaction current density, SOH subsystem model, and the SOC estimation error can be estimated when E_1 is accurately evaluated. Finally, the method to evaluate E_1 is discussed. In particular, E_1 is evaluated through comparing voltage responses with different initial SOC. Two challenges are identified with this method. First, the sensitivity of the voltage to the states depends on the unknown SOC estimation error, and thus E_1 cannot be evaluated accurately without knowing the exact SOC estimation error. Second, to accurately estimate the side reaction current density and the SOH subsystem parameter, the requirement for the accuracy of evaluation of E_1 is very high. These two challenges make it difficult to estimate the side reaction current density using the TSF in practice. This difficulty is due to the nature of the low impact of the side reaction current density to the voltage, but not due to the incapability of the TSF algorithm or of the method to evaluate E_1 .

It can be concluded that accurate evaluation of the sensitivity of the voltage to the SOC is required for accurate estimation of the side reaction current density using the TSF under the presence of SOC estimation errors. This conclusion agrees with the fact that the TSF improves estimation accuracy of the side reaction current density by evaluating the voltage error caused by the SOC estimation errors and then eliminating this voltage error in estimation of the side reaction current density. Because the evaluation of the sensitivity of the voltage to the SOC determines the

evaluation of the voltage error caused by the SOC estimation errors, it also affects the estimation accuracy of the side reaction current density using the TSF. It can also be deduced that similar requirements for the sensitivity of the voltage to the SOC is also expected for other estimation algorithms that improve estimation accuracy of the side reaction current density under the presence of SOC estimation errors by evaluating the voltage errors caused by the SOC estimation errors through the sensitivity of the voltage to the SOC. Similarly, other estimation algorithms that improve estimation accuracy of the side reaction current density under the presence of other non-ideal conditions by evaluating the voltage errors caused by the non-ideal conditions through the sensitivities of the voltage would also require accurate evaluation of the sensitivity of the voltage to the non-ideal conditions.

In summary, this chapter makes four main contributions. First, a new subsystem identification algorithm, the TSF, is developed based on RCSI used in Chapter 3. The TSF can be applied to estimate the subsystem parameter and output, as well as the persistent main system state estimation error simultaneously in any system that is marginally stable and with weak feedback of the subsystem output. Second, the TSF is applied to estimate the side reaction current density in the battery under the presence of the SOC estimation error when the sensitivity of the voltage to the state can be accurately evaluated. Third, the method for obtaining approximation of the sensitivity of the voltage to the state through voltage responses is presented. Fourth, the challenges for applying the TSF in practice to estimate the side reaction current density with E_1 evaluated using this method are identified. The challenges are mainly because accurate estimation of the side reaction current density requires highly accurate evaluation of the sensitivity of the voltage to the SOC. These challenges verify the analyses in Chapter 3 that the high sensitivity of the estimate of the side reaction current density to SOC estimation error is a fundamental problem caused by the fact that the side reaction current density has low impact on the voltage, and cannot be solved by changing estimation algorithms.

Chapter 5

Estimation of the Number of Cyclable Li-ions

5.1 Introduction

In this chapter, the number of cyclable Li-ions is estimated as the SOH indicator. In a Li-ion battery, the number of cyclable Li-ions is a measure of the charge that moves between the electrodes during charge and discharge of the battery. Therefore, the number of cyclable Li-ions is a measure of the capacity of Li-ion batteries [28, 72]. During the process of Li-ion-consuming electrochemical degradation, cyclable Li-ions are consumed through side reactions, which results in capacity fade [31, 72]. Therefore, the remaining number of cyclable Li-ions reflects the remaining capacity after degradation; thus this remaining number can be used as an SOH indicator.

The number of cyclable Li-ions has the following advantages compared with other electrochemical SOH indicators. i) Compared with the SEI film resistance that can be applied only to the SEI-film-formation mechanism, the number of cyclable Li-ions is a general SOH indicator for all electrochemical-based mechanisms that consume Li-ions. ii) Compared with the side reaction current density, the number of cyclable Li-ions is expected to be more robust to uncertainties, because it results from the integration of the side reaction current density over time and space.

In this chapter, SOH monitoring is investigated using LMO-mixture battery as

an example. With Mn dissolution reduced by adding other Li-compounds, Li-ion consumption dominates Mn dissolution and becomes the main ageing mechanism for batteries with LMO-mixture cathode materials [73, 74]. Therefore, the number of cyclable Li-ions becomes a suitable SOH indicator for these batteries. However, the estimation technique developed in this chapter can also be applied to other parameter sets and other battery chemistries to monitor the SOH change resulting from any electrochemical-based degradation mechanism that consumes cyclable Li-ions.

Compared with [41], which also estimates the number of cyclable Li-ions as the SOH indicator, albeit for a battery with different cathode material, this chapter proposes three novel approaches to take practical conditions into account in simulations.

- i) In this chapter, the system model used in the algorithm is the single particle model (SPM) [56, 54], a simplified battery electrochemical model that contains only two states, which yields a computational complexity suitable for on-line estimation. To verify the sufficiency of using the SPM in the algorithm, the true system (the battery) is represented with the Doyle-Fuller-Newman (DFN) model [51], an electrochemical model with higher fidelity than the SPM, in the simulations. In contrast, the simulations in [41] are based on the SPM completely.
- ii) In practice, parameters of the battery are not directly available, and are typically estimated from the input-output signal pairs of the battery, which is referred to as parameterization. Therefore, unlike [41] that assumes the parameters other than the ones subject to on-line estimation are known and identical to the ones of the true battery, in this chapter the process of parameterization is also simulated as a preparation stage for estimation of the number of cyclable Li-ions. This preparation stage brings the simulation study closer to practice by considering the effect of the inevitable modeling error introduced by parameterization.
- iii) This chapter provides a robustness analysis of estimating the number of cyclable Li-ions under a variety of non-ideal conditions (i.e., with the SOC estimation error, modeling error, and measurement noise) to consider the impact of un-modeled non-ideal conditions on estimation accuracy. Furthermore, unlike [41] that uses an adaptive PDE observer with nonlinear least squares, this chapter uses the EKF as the estimation algorithm. The EKF is chosen instead of the method in [41] because

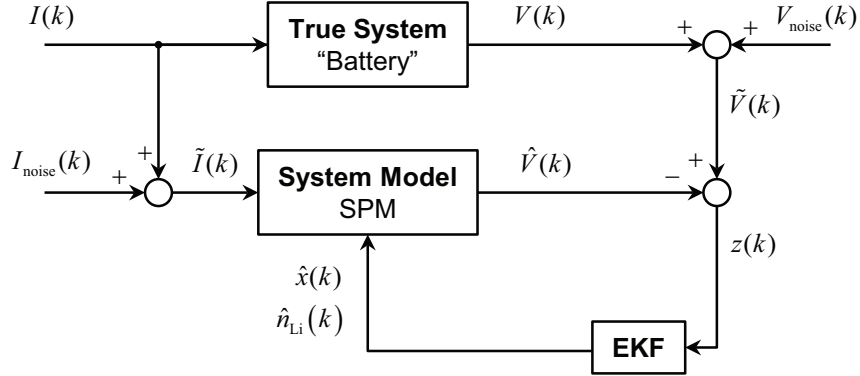


Figure 5.1: The block diagram for estimation of the number of cyclable Li-ions using the extended Kalman filter (EKF). The true system is a battery in practice but is represented with a battery model, namely the Doyle-Fuller-Newman (DFN) model, in the simulation study presented herein. The system model is the single particle model (SPM), a simplification of the DFN model.

this chapter mainly focuses on exploring the effectiveness of estimating the number of cyclable Li-ions as the SOH indicator, while [41] focuses on co-estimation of the SOC and the SOH.

This chapter mainly addresses the following research questions:

1. Is it possible to estimate the number of cyclable Li-ions as a parameter of the battery system using the EKF?
2. How robust is this estimation against various non-ideal conditions?
3. Is the number of cyclable Li-ions robust enough to be an effective SOH indicator in practice?

5.2 Problem Setup

The goal of this chapter is to estimate the number of cyclable Li-ions at a given point of time through the current and voltage trajectories during battery charge/discharge. By comparing estimates at different points of time throughout battery service life, the trend of degradation can be obtained. Because the dynamics of the number of cyclable Li-ions is significantly slower than the charge and discharge dynamics, the

change in the number of cyclable Li-ions during a short period of charge/discharge can be ignored. Therefore, within the scope of this chapter, the number of cyclable Li-ions is considered as a parameter of the battery, a nonlinear system. Figure 5.1 presents the block diagram used in this paper for estimation of the number of cyclable Li-ions as a parameter estimation problem in nonlinear systems. In this section, the overall structure of the diagram is explained.

5.2.1 True System

In practice, the true system is a battery; while for the simulation study presented herein, the true system is represented with the DFN model.

Notice that the SOH model is not included in the true system. This is because i) the influence of the side reaction current density to the voltage is insignificant as shown in Section 3.4 and ii) the dynamics of the number of cyclable Li-ions is significantly slower than the charge and discharge dynamics, and thus the influence of the side reaction current density on the number of cyclable Li-ions during a short period of time can be ignored. Furthermore, the side reactions are also ignored in the charge and discharge dynamics here. Therefore, in this chapter, the DFN model has the form

$$x(k+1) = f(x(k), I(k)), \quad (5.1)$$

$$V(k) = g_0(x(k), I(k)), \quad (5.2)$$

where $f(\cdot)$ and $g_0(\cdot)$ represent (2.32) and (2.34), respectively, with $J_{\text{sd}} = 0$.

The input $I(k)$ and output $V(k)$ of the true system are the current and voltage, respectively. The measurements of $I(k)$ and $V(k)$ are $\tilde{I}(k)$ and $\tilde{V}(k)$, which are corrupted by measurement noise $I_{\text{noise}}(k)$ and $V_{\text{noise}}(k)$, respectively.

5.2.2 System Model

The system model acts as an estimate of the true system. The modeling information used by estimation algorithms is based on the system model. This paper assumes that the parameters/signal in the system model that estimates a parameters/signal ζ in the true system is denoted with $\hat{\zeta}$. This notation convention applies to all parameter/signals in the system model except the measurement $\tilde{I}(k)$ and known constants F , R , α and T_s . The input and output of the system model are the current measurement $\tilde{I}(k)$ and the voltage estimate $\hat{V}(k)$, respectively. The SPM is chosen as the system model. Compared with the DFN model, the SPM has fewer states and simpler model structure, which yields lower computational complexity that is beneficial for on-line estimation.

To incorporate the number of cyclable Li-ions as a parameter in the system model, the SPM is modified in this chapter using the similar technique in Section 4.3.1, i.e., removing the state equation for the solid concentration in the cathode and computing $c_{se,p}$ using $c_{se,n}$ and the number of cyclable Li-ions instead. Therefore, the state space model of the SPM in this chapter is the same as (4.39) – (4.40), i.e.,

$$\hat{x}(k+1) = \hat{A}\hat{x}(k) + \hat{F}\tilde{I}(k), \quad (5.3)$$

$$\hat{V}(k) = \hat{g}_0(\hat{x}(k), \tilde{I}(k)), \quad (5.4)$$

where \hat{A} and \hat{F} are obtained from (2.42) for the anode, and $g_0(\cdot)$ represents (2.48) where $\hat{c}_{se,p}$ is obtained from (4.38).

5.2.3 Estimation Technique

The EKF, an estimation technique for nonlinear systems, is chosen as the estimation algorithm in this chapter. The benefit of using the EKF lies in the particular structure of the SPM, which feeds modeling information to the EKF, and is discussed in detail in Section 5.3. The EKF receives the error $z(k)$ between the measurement $\tilde{V}(k)$ and estimate $\hat{V}(k)$ of the voltage as the input and yields the estimate of the state, $\hat{x}(k)$,

and the estimate of the number of cyclable Li-ions, $\hat{n}_{\text{Li}}(k)$.

5.2.4 Estimation Process

The estimation process in this chapter is composed of two stages: i) the preparation stage and ii) the estimation stage. The preparation stage, which is not presented in Figure 5.1, does not involve estimation of the number of cyclable Li-ions using the EKF, but prepares for the estimation by parameterizing the system model from charging/discharging current and voltage data of the true system. This stage is to simulate the process in practice where the parameters used in the system model need to be determined from cycling data from the battery. The estimation stage estimates the number of cyclable Li-ions using the scheme from Figure 5.1 with the parameters of the system model from the preparation stage.

5.3 The Extended Kalman Filter

The goal of this chapter is to estimate the number of cyclable Li-ions, which translates into a parameter estimation problem in a nonlinear system. This problem can be solved by nonlinear extensions of the Kalman filter. In this chapter, the EKF is chosen. The linear dynamics (5.3) in the SPM eliminate the need for linearization of the state equation. Moreover, with the second-order Padé approximation, the SPM has only two states. These two facts simplify the design of the EKF, which is the main reason that the EKF is chosen herein.

The extended estimated state $\hat{X}(k)$ of the SPM is defined by treating \hat{n}_{Li} as the third state. Then,

$$\hat{X}(k) \triangleq (\hat{x}^T(k), \hat{n}_{\text{Li}})^T \in \mathbb{R}^3. \quad (5.5)$$

Then the evolution of the SPM using the extended state $\hat{X}(k)$ follows

$$\hat{X}(k+1) = \hat{A}_e \hat{X}(k) + \hat{B}_e \tilde{I}(k), \quad (5.6)$$

$$\hat{V}(k) = \hat{f}_e(\hat{X}(k), \tilde{I}(k)), \quad (5.7)$$

where

$$\hat{A}_e = \begin{bmatrix} \hat{A} & 0 \\ 0 & 1 \end{bmatrix}, \quad \hat{B}_e = \begin{bmatrix} \hat{F} \\ 0 \end{bmatrix}, \quad (5.8)$$

and $\hat{f}_e(\hat{X}(k), \tilde{I}(k))$ satisfies $\hat{f}_e(\hat{X}(k), \tilde{I}(k)) = \hat{f}(\hat{x}(k), \tilde{I}(k))$.

Then, the algorithm for the EKF in this chapter is summarized as follows.

$$\hat{X}^-(k) = \hat{A}_e \hat{X}^+(k-1) + \hat{B}_e \tilde{I}(k-1), \quad (5.9)$$

$$\hat{P}^-(k) = \hat{A}_e \hat{P}^+(k-1) \hat{A}_e^T + P_\omega, \quad (5.10)$$

$$L(k) = \hat{P}^-(k) \hat{C}^T(k) [\hat{C}(k) \hat{P}^-(k) \hat{C}^T(k) + P_\nu]^{-1}, \quad (5.11)$$

$$\hat{X}^+(k) = \hat{X}^-(k) + L(k) [\tilde{V}(k) - \hat{V}(k)], \quad (5.12)$$

$$\hat{P}^+(k) = (I_{l_x} - L(k) \hat{C}(k)) \hat{P}^-(k). \quad (5.13)$$

where

$$\hat{C}(k) = \left. \frac{\partial \hat{f}_e(\hat{X}, \tilde{I})}{\partial \hat{X}} \right|_{\hat{X}=\hat{X}^-(k), \tilde{I}=\tilde{I}(k)}, \quad (5.14)$$

$$\hat{V}(k) = \hat{f}_e(\hat{X}^-(k), \tilde{I}(k)), \quad (5.15)$$

I_3 refers to the identity matrix of size 3. $P_\omega \in \mathbb{R}$ and $P_\nu \in \mathbb{R}$ represent the covariance matrices for the process and measurement noise, respectively. Here, P_ω and P_ν are two tunable parameters.

$\hat{X}^-(k)$ and $\hat{P}^-(k)$ are the predictions of the state $X(k)$ and the covariance of the error $\hat{X}^-(k) - X(k)$ obtained from previous estimates. Notice that (5.9) and (5.15) in this prediction step are obtained from the SPM, which occurs in the system

model block in Figure 5.1. $\hat{X}^+(k)$ and $\hat{P}^+(k)$ are the EKF estimates of $X(k)$ and the covariance of the estimation error $\hat{X}^+(k) - X(k)$. For this application,

$$\hat{x}(k) \triangleq (\hat{X}_1^+(k), \hat{X}_2^+(k))^T, \quad (5.16)$$

$$\hat{n}_{\text{Li}}(k) \triangleq \hat{X}_3^+(k), \quad (5.17)$$

where \hat{X}_i^+ denotes the i^{th} component in \hat{X}^+ .

5.4 The Preparation Stage: Parameterization

In this section, the preparation stage for estimation of the number of cyclable Li-ions, namely parameterization of the SPM, is discussed. To this end, the genetic algorithm is used to identify 16 parameters in the SPM that contribute to the voltage response. Notice that this stage is used to obtain a set of parameters for the estimation stage and it is not the purpose of this chapter to discuss how to parameterize a battery model. Therefore, a comparison between different parameterization methods is beyond the scope of this chapter and is not discussed herein.

5.4.1 Parameterization using Genetic Algorithm

In this section, the process of parameterizing the SPM using the genetic algorithm is discussed. The benchmark of parameterization is the DFN model with 50 particles per electrode, which is the model that is used for the true system. The parameters of the DFN model are obtained from [3] where an HEV battery with LMO-mixture cathode material is identified with experimental data.

The DFN model is cycled with two current trajectories to obtain the output voltage trajectories to be used in the genetic algorithm. One trajectory is 1-C (6-A) constant current charge (CCC) between stoichiometry at 0% and 100% SOC (θ_n between 0.126 and 0.676). The other trajectory is the current trajectory generated from an EV following the UDDS. Similar to Chapter 3, this UDDS current trajectory is generated by the Advisor software [62] with the default EV settings. The Li-ion

battery in Advisor has a capacity of 7 Ah, while the rated capacity of the battery model in this chapter is 6 Ah. Therefore, the current magnitude is scaled down to match the C-rates and to ensure that the battery is not overdischarged.

In the genetic algorithm, the same input current trajectories are given to the SPM to generate voltage trajectories. The goal of the genetic algorithm is to minimize the mean squared error between the voltage responses of the SPM and the DFN model; i.e., the fitness function is

$$f_{GA} = \frac{1}{N_1 + N_U} \sqrt{\|V_{DFN,1} - V_{SPM,1}\|^2 + \|V_{DFN,U} - V_{SPM,U}\|^2}, \quad (5.18)$$

where N_1 and N_U are the total numbers of data points in the 1-C CCC and UDDS trajectories, respectively. V_{DFN} and V_{SPM} are the voltage response trajectories from the DFN model and the SPM, respectively. The subscripts 1 and U denotes the 1-C CCC and UDDS trajectories, respectively.

This chapter assumes that i) the function of the reference potential with respect to the stoichiometry for both electrodes, namely $\hat{U}_{ref,p}(\hat{\theta}_p)$ and $\hat{U}_{ref,n}(\hat{\theta}_n)$, are known; and ii) the stoichiometry of both electrodes at the beginning and end of the 1-C CCC and UDDS modes are known. The first assumption is valid in practice because the reference potentials can be determined using half cells. The second assumption is valid in practice because the stoichiometry can be obtained from the measurement of the open circuit voltage after resting. Therefore, the reference potential function and the stoichiometry at the beginning and the end of the two modes in the SPM are set the same as in the DFN model.

This chapter further applies the assumption that the number of cyclable Li-ions remains the same throughout the 1-C CCC mode to establish the relationship between $\hat{c}_{s,max,p}$ and $\hat{c}_{s,max,n}$. Based on (2.41),

$$\begin{aligned} & \hat{\epsilon}_{s,p} \hat{L}_p \hat{A} \hat{c}_{s,max,p} \hat{\theta}_p(0) + \hat{\epsilon}_{s,n} \hat{L}_n \hat{A} \hat{c}_{s,max,n} \hat{\theta}_n(0) \\ &= \hat{\epsilon}_{s,p} \hat{L}_p \hat{A} \hat{c}_{s,max,p} \hat{\theta}_p(N_1) + \hat{\epsilon}_{s,n} \hat{L}_n \hat{A} \hat{c}_{s,max,n} \hat{\theta}_n(N_1), \end{aligned} \quad (5.19)$$

where $\hat{\theta}_p(0)$, $\hat{\theta}_n(0)$, $\hat{\theta}_p(N_1)$, and $\hat{\theta}_n(N_1)$ are the same as in the DFN model and obtained from [3]. Therefore,

$$\hat{c}_{s,\max,p} = \frac{\hat{\epsilon}_{s,n}\hat{L}_n[\hat{\theta}_n(N_1) - \hat{\theta}_n(0)]}{\hat{\epsilon}_{s,p}\hat{L}_p[\hat{\theta}_p(0) - \hat{\theta}_p(N_1)]}\hat{c}_{s,\max,n}. \quad (5.20)$$

In the SPM, $\hat{c}_{s,\max,n}$ is identified from the genetic algorithm, while $\hat{c}_{s,\max,p}$ is calculated from $\hat{\epsilon}_{s,n}$, $\hat{\epsilon}_{s,p}$, \hat{L}_n , \hat{L}_p , and $\hat{c}_{s,\max,n}$ identified by the genetic algorithm.

Because the radius R_n and R_p of particles are available from the electrode materials and the anode material is universal among different Li-ion battery chemistries, this chapter assumes that R_n is known and fixes \hat{R}_n to 10^{-6} given in [3] to accelerate the genetic algorithm but identifies \hat{R}_p within the range of $[10^{-7}, 10^{-5}]$ to allow enough freedom for voltage matching.

Initial parameters in the genetic algorithm are obtained from the literature. Here the initial parameters are set as the same as in the DFN model, which is presented in the column Originial in Table 5.1. GA_{1+U,1} and GA_{1+U,2} in Table 5.1 represent two identified parameter sets from two independent runs of genetic algorithm identification using both a 1-C CCC current trajectory and a UDDS current trajectory. Figure 5.2 presents the voltage responses of the SPM with the parameter sets from GA_{1+U,1}, GA_{1+U,2}, and Original, and the DFN model under the 1-C CCC and UDDS trajectories. It can be observed that the two parameter sets are different from each other but can produce similar voltage responses, which also match the voltage response of the DFN model better than the SPM using the same parameters as in the DFN model.

5.4.2 Discussions about Parameterization

First, notice that the number of cyclable Li-ions can be deduced from the identified parameter set by first deducing $\hat{c}_{s,\max,p}$ using (5.20) and then deducing \hat{n}_{Li} using

Variable	Original	GA _{1+U,1}	GA _{1+U,2}	GA _{10+U}
A [m ²]	1.0452	1.235	1.026	1.529
L_n [m]	5.00E-5	4.559E-5	1.284E-5	1.382E-5
L_p [m]	2.54E-5	1.178E-5	4.062E-5	1.952E-5
L_{sep} [m]	3.64E-5	4.738E-5	2.993E-5	3.247E-5
R_p [m]	1.00E-6	1.836E-6	1.069E-6	6.263E-6
$\epsilon_{s,n}$	0.58	0.4674	0.4862	0.3780
$\epsilon_{s,p}$	0.50	0.2312	0.2873	0.7450
$\epsilon_{e,n}$	0.332	0.5659	0.3637	0.5477
$\epsilon_{e,p}$	0.33	0.3788	0.3760	0.4414
$\epsilon_{e,sep}$	0.50	0.2704	0.2421	0.2485
$D_{s,n}$ [m ² s ⁻¹]	2.00E-16	3.771E-16	3.759E-16	4.379E-16
$c_{s,max,n}$ [mol m ⁻³]	1.61E+4	1.855E+4	7.613E+4	5.855E+4
$i_{0,n}$ [A m ⁻²]	36	50.00	11.53	11.14
$i_{0,p}$ [A m ⁻²]	26	11.69	12.15	12.82
R_{film} [Ω m ²]	0.002	1.000E-3	4.900E-3	4.700E-3
c_e [mol m ⁻³]	1.20E+3	1.747E+3	1.367E+3	1.217E+3

Table 5.1: The identified parameter sets from the genetic algorithm. The parameter set in the column labelled Original is from [3]. The parameter sets in the columns labelled GA_{1+U,1} and GA_{1+U,2} are obtained from two independent runs of genetic algorithm identification using current trajectories including a 1-C constant current charge (CCC) trajectory and a Urban Dynamometer Driving Schedule (UDDS) trajectory. The parameter set in the column labelled GA_{10+U} is obtained from genetic algorithm identification using current trajectories including a 10-C CCC trajectory and a UDDS trajectory.

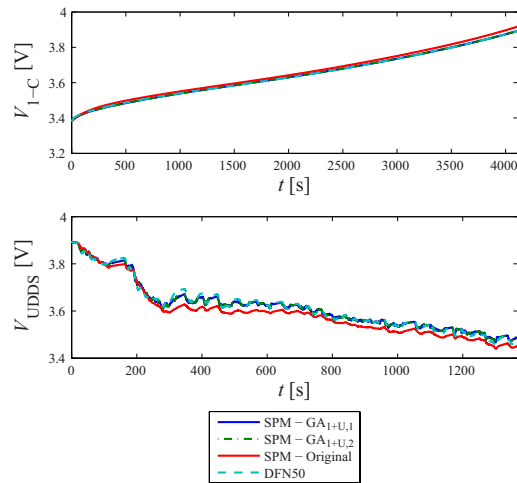


Figure 5.2: Comparison among the voltage responses of the SPM with the parameter sets from GA_{1+U,1}, GA_{1+U,2}, and Original, and the DFN model.

Deduced Variables	Original	GA _{1+U,1}	GA _{1+U,2}	GA _{10+U}
$c_{s,\max,p}$ [mol m ⁻³]	4.1E+4	1.616E+5	4.534E+4	2.341E+4
n_{Li} [mol]	5.7E-1	5.700E-1	5.694E-1	5.460E-1

Table 5.2: The variables deduced from the parameter sets in [3] (Original), two independent runs of genetic algorithm identification using input current trajectories including a 1-C CCC trajectory and a UDDS trajectory (GA_{1+U,1} and GA_{1+U,2}), and a run of genetic algorithm identification using input current trajectories including a 10-C charge trajectory and a UDDS trajectory (GA_{10+U}).

(2.41), which yields

$$\hat{n}_{Li} = \hat{\epsilon}_{s,n} \hat{L}_n \hat{A} \hat{c}_{s,\max,n} \left(\frac{\theta_n(N_1) - \theta_n(0)}{\theta_p(0) - \theta_p(N_1)} \theta_p(0) + \theta_n(0) \right). \quad (5.21)$$

Therefore, for each identified parameter set, it is possible to deduce the value of the number of cyclable Li-ions associated with this parameter set. During estimation, this value for the number of cyclable Li-ions is the value that is being estimated.

In this section, the following two questions are addressed regarding deducing the number of cyclable Li-ions from identified parameter sets as shown in (5.21):

- (1) Does the deduced number of cyclable Li-ions change with respect to different runs of parameterization?
- (2) With this deduced value for the number of cyclable Li-ions, why is it still needed to estimate the number of cyclable Li-ions using the EKF?

A well-known feature with genetic-algorithm-based parameterization is that the parameter sets that the algorithm converges to can vary even using the same data, initial conditions, algorithm settings, and fitness function [75]. This feature can be seen from GA_{1+U,1} and GA_{1+U,2} in Table 5.1, which gives different identified parameter sets from two independent runs of genetic algorithm identification under the same conditions. This feature gives a certain level of randomness as to the precise value of each individual parameter. A natural question to ask under this situation is whether this “randomness” in the value of identified parameter set affects the deduced value of the number of cyclable Li-ions. It is presented below that the deduced number

of cyclable Li-ions is unchanged as long as the identified parameter set can yield well-matched voltage responses between the true system and the SPM.

The parameterization results support the previous argument that the deduced \hat{n}_{Li} remains unchanged among different parameterization runs. Table 5.2 presents the deduced $\hat{c}_{s,\max,p}$ and \hat{n}_{Li} for Originial, GA_{1+U,1}, and GA_{1+U,2}. It can be observed that even though the values of $\hat{c}_{s,\max,p}$ are different (difference can be as high as 300% of the Originial value) between GA_{1+U,1} and GA_{1+U,2}, the values of \hat{n}_{Li} are very close (vary within 0.2% of the Originial value) for the two cases.

To explain why the deduced n_{Li} remains the same, first note that under the previous assumptions, $\hat{\theta}_p$ and $\hat{\theta}_n$ have a one-to-one relationship. Based on (5.20) and (5.21), for the SPM,

$$\begin{aligned}\hat{\theta}_p(k) &= \left(\hat{\theta}_p(0) + \frac{\hat{\theta}_p(0) - \hat{\theta}_p(N_1)}{\hat{\theta}_n(N_1) - \hat{\theta}_n(0)} \hat{\theta}_n(0) \right) \\ &\quad - \frac{\hat{\theta}_p(0) - \hat{\theta}_p(N_1)}{\hat{\theta}_n(N_1) - \hat{\theta}_n(0)} \hat{\theta}_n(k).\end{aligned}\tag{5.22}$$

Because $\hat{\theta}_n(0)$, $\hat{\theta}_n(N_1)$, $\hat{\theta}_p(0)$, and $\hat{\theta}_p(N_1)$ are known from [3], $\hat{\theta}_p(k)$ and $\hat{\theta}_n(k)$ have a one-to-one relationship.

Then, it can be shown that the objective of matching the voltage response of the SPM to a certain trajectory forces $\hat{\theta}_n$ to evolve according to certain dynamics. Because $\hat{\theta}_p$ and $\hat{\theta}_n$ have a one-to-one relationship, $\hat{U}_{\text{ref},p}$ and $\hat{U}_{\text{ref},n}$ are both functions of $\hat{\theta}_n$. Therefore, $\hat{U}_{\text{ref},p} - \hat{U}_{\text{ref},n}$ is a function of only $\hat{\theta}_n$. The voltage is primarily dominated by the reference potentials, namely, $\hat{U}_{\text{ref},p} - \hat{U}_{\text{ref},n}$: within the operating stoichiometry, $\hat{U}_{\text{ref},p} - \hat{U}_{\text{ref},n}$ ranges between [3.38, 3.89] V while the other voltage components only amount to about 2.5×10^{-3} V. Therefore, regulating the voltage response of the SPM, which is essentially the objective of genetic algorithm identification, results in regulating $\hat{U}_{\text{ref},p} - \hat{U}_{\text{ref},n}$, which results in the regulating $\hat{\theta}_n$ at every sampling instant. This enforces certain dynamics on $\hat{\theta}_n$ to match this $\hat{\theta}_n$ trajectory.

Next, it can be shown that this requirement on the dynamics of $\hat{\theta}_n$ enforces \hat{n}_{Li} to be deduced to a certain value, regardless of the values of other parameters. Sub-

stituting (2.26) and (2.39) into (2.30) yields the transfer function between $\hat{\theta}_n$ and \tilde{I} , namely,

$$\frac{\hat{\theta}_n}{\tilde{I}} = \frac{5}{3F(\hat{A}\hat{L}_n\hat{\epsilon}_{s,n}\hat{c}_{s,max,n})} \frac{2\hat{R}_n^2 s + 21\hat{D}_{s,n}}{\hat{R}_n^2 s^2 + 35\hat{D}_{s,n}s}. \quad (5.23)$$

This transfer function governs the dynamics of $\hat{\theta}_n$. Because the trajectory for current \tilde{I} is predetermined, a fixed $\hat{\theta}_n$ trajectory means a fixed transfer function, with respect to different parameter set. Because the radius \hat{R}_n is fixed and F is a constant, the fixed transfer function requires $\hat{A}\hat{L}_n\hat{\epsilon}_{s,n}\hat{c}_{s,max,n}$ to be fixed, too. Therefore, according to (5.21), the value of the deduced \hat{n}_{Li} is also fixed, which agrees with the identification results in GA_{1+U,1} and GA_{1+U,2}.

Notice that this fixed \hat{n}_{Li} only comes with genetic algorithm identification that uses current trajectories mainly composed of low C-rate current. Because the SPM ignores the concentration distribution along the thickness of the anode-separator-cathode and is accurate only when the C-rate is low, the genetic algorithm is unable to match the trajectory of $\hat{\theta}_n$ with that of the DFN model when the current trajectories are mainly composed of high C-rate current. Therefore, the deduced \hat{n}_{Li} is not accurate and is not the same among different runs of the genetic algorithm in the high C-rate case. Indeed, the current trajectories used in GA_{1+U,1} and GA_{1+U,2} consist mostly of the 1-C CCC trajectory. Therefore, the deduced \hat{n}_{Li} is accurately matching n_{Li} deduced from the originial parameter set and the same between GA_{1+U,1} and GA_{1+U,2}. On the other hand, GA_{10+U} in Table 5.1 is identified with current trajectories including a 10-C CCC trajectory and a UDDS trajectory. As a result of the high C-rates, the deduced \hat{n}_{Li} in GA_{10+U} is different from the deduced \hat{n}_{Li} in the other three cases. The voltage is also not as accurately matched when the C-rate is high, which can be observed from the higher fitness value of the genetic algorithm. The fitness value for GA_{1+U,1} and GA_{1+U,2} are both 0.0053, while the fitness value for GA_{10+U} is 0.0089, which is almost twice as high as GA_{1+U,1} and GA_{1+U,2}. Therefore, in order for parameterization of the SPM to facilitate the estimation stage, the current trajectories should be designed so that they are at low C-rates at most of the time.

From this point on, this section answers the second question: with this deduced \hat{n}_{Li} , why is it needed to estimate n_{Li} using the EKF? Although parameterization and the EKF-based estimation can both serve the purpose of providing an estimate for n_{Li} , the two methods differ dramatically in efficiency. Parameterization is time consuming. Collecting the data including the necessary battery resting periods and running the genetic algorithm need to take the battery off-line and can easily take a time on the order of a day. Meanwhile, the EKF-based estimation can be conducted on-line within seconds (as can be seen in Section 5.5). In order to monitor loss of cyclable Li-ions, n_{Li} is required to be estimated as frequently as the change of n_{Li} throughout the service life. Therefore, it is more efficient to use the EKF-based algorithm that estimates n_{Li} with much fewer resources than to go through parameterization every time a new estimate of n_{Li} is required.

However, it can still be beneficial if parameterization is not conducted only once at the beginning of the service life, but a few times throughout the life time, though less frequently than estimation of n_{Li} . Re-parameterizations influence the performance of the EKF-based estimation of n_{Li} by regulating the errors in model parameters caused by other degradation mechanisms (e.g., loss of active material, structural change). The influence of re-parameterization on the accuracy of estimation of n_{Li} is investigated in detail in Section 5.6.2. The fact that it can be performed less frequently than estimation of n_{Li} is a result of the assumption that the dominant degradation mechanism is the consumption of cyclable Li-ions and thus n_{Li} has a faster dynamics than other parameters of the battery. Therefore, a preferred model of operation is to perform parameterization just enough times throughout the battery service life to capture the changes of the values of parameters caused by other degradation mechanisms, and to use more efficient estimation algorithms such as the EKF-based algorithm herein to track the changes in the cyclable Li-ions between the times of parameterization.

5.5 The Estimation Stage: Estimation under Ideal Conditions

In this section, simulation results are provided to estimate the number of cyclable Li-ions using the EKF under the ideal conditions. The ideal conditions are defined as follows.

1. No noise in input and output measurements, which means $\tilde{I}(k) = I(k)$ and $\tilde{V}(k) = V(k)$.
2. No additional errors in modeling. Notice that by using the SPM in the EKF as a model for the true system that is either a real battery or the DFN model, and by using the parameter set identified by the genetic algorithm in the SPM, there are already differences in model structure and parameters under this problem formulation. Here, under ideal conditions, this chapter assumes that these differences are present, but there are no additional differences between the structure and parameters of the True System and System Model blocks in Figure 5.1.
3. No error in the initial estimation of the SOC. Here the SOC refers to θ_n defined in (2.26). Therefore, no initial SOC estimation error implies $\hat{\theta}_n(0) = \theta_n(0)$. When there is no modeling error, $\hat{c}_{s,\max,n} = c_{s,\max,n}$. Then $\hat{c}_{se,n}(0) = c_{se,n}(0)$.

The parameters of the true system are obtained from [3] (listed as Original in Table 5.1) while the parameters of the system model is GA_{1+U,2} in Table 5.1, which is obtained from parameterization. The parameters for the EKF are set as follows. The noise covariance matrices are $P_\omega = 1$ and $P_\nu = 10$. The initial estimate of the extended state is $\hat{X}^+(0) = (\hat{x}(0)^T, \hat{n}_{Li}(0))^T$, where $\hat{x}(0)$ yields the same initial SOC as in the true system given by $x(0)$ and $\hat{n}_{Li}(0) = 0$. The initial estimate for the error covariance matrix is $\hat{P}^+(0) = 10^4 I_{l_x+1}$.

Both the 1-C CCC trajectory and the UDDS trajectory used in parameterization are used as the excitation in this section. The 1-C CCC trajectory simulates

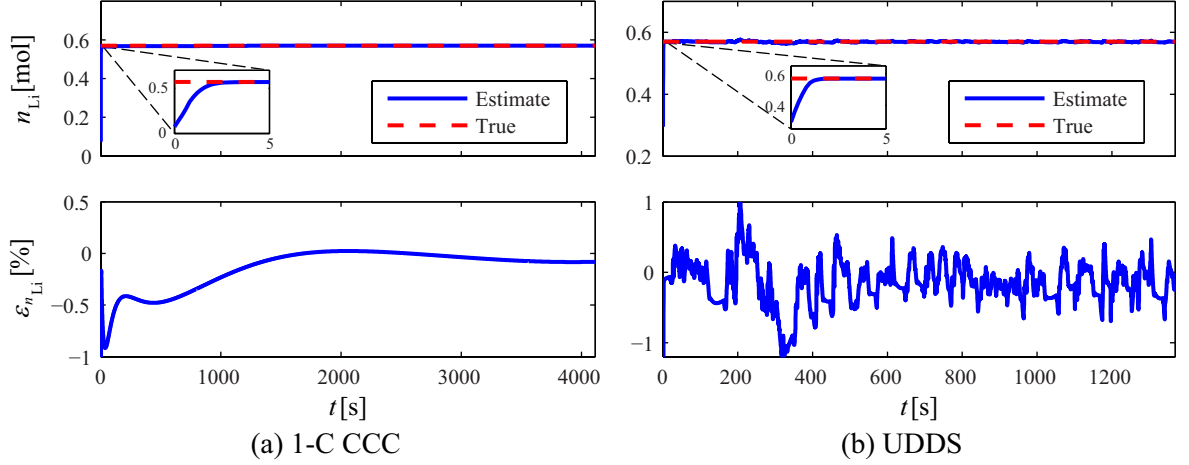


Figure 5.3: The estimate \hat{n}_{Li} and relative estimation error $\epsilon_{n_{\text{Li}}}$ of the number of cyclable Li-ions n_{Li} under the ideal conditions for two current trajectories: (a) 1-C constant current charge (CCC) trajectory and (b) an EV current trajectory for the Urban Dynamometer Driving Schedule (UDDS).

the fast charge of HEV/EV batteries. The UDDS trajectory evaluates the effectiveness of the algorithm under dynamic battery loading conditions typical for HEV/EV applications.

The performance of the algorithm is indicated by the accuracy of estimating the number of cyclable Li-ions. This accuracy is measured by the relative estimation error $\epsilon_{n_{\text{Li}}}(k)$.

$$\epsilon_{n_{\text{Li}}}(k) \triangleq \frac{\hat{n}_{\text{Li}}(k) - n_{\text{Li}}}{n_{\text{Li}}} \times 100\%. \quad (5.24)$$

Figure 5.3 (a) and (b) present the estimation results under the ideal conditions for 1-C CCC trajectory and the UDDS trajectory, respectively. In both Figure 5.3 (a) and (b), $\hat{n}_{\text{Li}}(k)$ converges close to n_{Li} in 5 seconds after initializing at 0. Under the 1-C CCC trajectory, the relative estimation error $\epsilon_{n_{\text{Li}}}$ is bounded within $[-1, 0.2]\%$ during the overall simulation, and converges to a bound within $\pm 0.2\%$ after half of the total simulation time. Under the UDDS trajectory, the relative estimation error is bounded within $[-1.2, 1]\%$. The fact that the estimate \hat{n}_{Li} does not converge to the true value n_{Li} is due to the difference between the voltage responses of the DFN model

and the SPM with different parameters. The small bounds of the relative estimation error $\epsilon_{n_{\text{Li}}}$ indicate that the level of this difference in the voltage response is small enough to have limited impact on estimation of the number of cyclable Li-ions. The results in Figure 5.3 show that the number of cyclable Li-ions can be accurately and quickly estimated under both 1-C CCC and UDDS current trajectories using the EKF under the ideal conditions.

The overall time taken to simulate the SPM, compute $\hat{C}(k)$, and conduct estimation using the EKF at each step, which corresponds to 0.2 s in the true system, is 0.01 s in this simulation. This time difference indicates that the computation required by the estimation algorithm designed in this chapter can be done within a much shorter time than required for on-line estimation. Although this simulation is conducted using Matlab 2014a on a 64-bit computer with 2.7-GHz processor while the estimation in vehicles is conducted using C or assembly language on 8- to 32-bit, 1- to 80-MHz micro-processors, this result still shows that the proposed method is potentially suitable for on-line applications.

5.6 The Estimation Stage: Robustness to Non-Ideal Conditions

In this section, robustness of the algorithm is examined using simulations by investigating the effects of three types of non-ideal conditions; namely, SOC estimation error, additional modeling error, and measurement noise. Only the 1-C CCC trajectory is used as an example for the current excitation. Similar results can be obtained from performing these robustness exams using the UDDS trajectory. Except Section 5.6.2, the parameters of the true system are the parameters listed as Original in Table 5.1, while the parameters of the system model are from GA_{1+U,2} in Table 5.1.

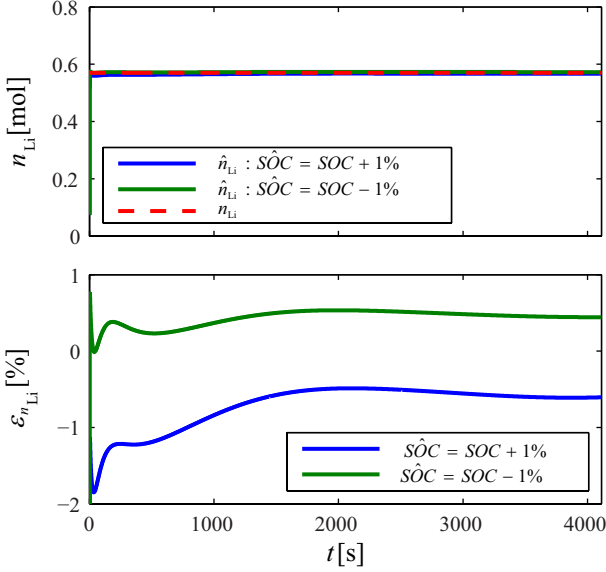


Figure 5.4: (a) The estimate and (b) relative estimation error $\epsilon_{n_{\text{Li}}}$ of the number of cyclable Li-ions n_{Li} under the presence of SOC estimation error.

5.6.1 Robustness to SOC Estimation Error

In this section, the effect of SOC estimation error on the performance of the algorithm is investigated. Here the initial SOC estimation error is set at $\pm 1\%$, because an error on this level is often expected in SOC estimation [34, 54, 40]. Because the stoichiometry θ_n is between 0.126 to 0.676, corresponding to 0% to 100% SOC [3], a difference of 1% in SOC corresponds to a difference of $(0.676 - 0.126) \times 1\% = 0.0055$ in θ_n . Therefore, the initial estimation of the state $\hat{x}(0)$ is set so that

$$\hat{\theta}_n(0) = \theta_n(0) \pm 0.0055, \quad (5.25)$$

where $\hat{\theta}_n(0)$ and $\theta_n(0)$ are computed from $\hat{x}(0)$ and $x(0)$, respectively. Then, in the EKF, $\hat{X}^+(0) = (\hat{x}(0)^T, 0)^T$, where $\hat{x}(0)$ yields a $\hat{\theta}_n(0)$ that satisfies (5.25). All the other parameters for the battery model and the EKF are the same as in Section 5.5.

Figure 5.4 presents the estimation results under the initial SOC estimation error as in (5.25). The relative estimation error $\epsilon_{n_{\text{Li}}}$ is bounded within $[-1.9, -0.5]\%$ and $[0, 0.4]\%$ for the cases $\hat{\text{SOC}}(0) = \text{SOC}(0) + 1\%$ (i.e., $\hat{\theta}_n(0) = \theta_n(0) + 0.0055$) and $\hat{\text{SOC}}(0) = \text{SOC}(0) - 1\%$ (i.e., $\hat{\theta}_n(0) = \theta_n(0) - 0.0055$), respectively. These bounds

for $\epsilon_{n_{Li}}$ suggest that an SOC estimation error on the level of $\pm 1\%$ has limited impact on the estimation accuracy of the number of cyclable Li-ions. The results in Figure 5.4 show that even under an SOC estimation error of $\pm 1\%$, the number of cyclable Li-ions can still be estimated accurately.

5.6.2 Robustness to Additional Modeling Error

This section investigates additional modeling error that results from parameter changes caused by battery degradation. As the number of cyclable Li-ions decreases after battery degradation caused by consumption of Li-ions, other battery parameters might also change due to various other degradation mechanisms. These changes in other parameters impact the voltage response of the battery, and thus impact the estimation accuracy of the number of cyclable Li-ions.

Besides the loss of cyclable Li-ions, another common degradation mechanism in batteries with LMO-mixture cathode material is the loss of active materials, which results in a decrease in the parameters $c_{s,\max,n}$ and $c_{s,\max,p}$. [73] reports that after 2000 constant current constant voltage cycles with 0.5 C current under 34°C, 8% and 4% active material loss are measured in the cathode and anode, respectively. Therefore, in this section, $c_{s,\max,n}$ and $c_{s,\max,p}$ are set at 96% and 92% of the values in the previous sections, while $\hat{c}_{s,\max,n}$ and $\hat{c}_{s,\max,p}$ remain at their previous levels. This setting simulates the situation where the estimation algorithm uses the parameters of a fresh battery to estimate the number of cyclable Li-ions in a used battery. Therefore, the modeling error considered herein is the error in model parameters, i.e., $c_{s,\max,n} = 0.96\hat{c}_{s,\max,n}$ and $c_{s,\max,p} = 0.92\hat{c}_{s,\max,p}$.

Figure 5.5 presents the estimation results with parameter errors in $c_{s,\max,n}$ and $c_{s,\max,p}$. It can be observed that under the modeling error considered in this chapter, $\epsilon_{n_{Li}}(k)$ is bounded within [2.7, 6.2]%. It can be concluded that other battery degradation mechanisms such as loss of active materials present a challenge to the estimation accuracy of the number of cyclable Li-ions. Therefore, it is beneficial to perform several re-parameterizations during the service life of the battery to capture the parameter changes caused by battery degradation and reduce its impact on estimation

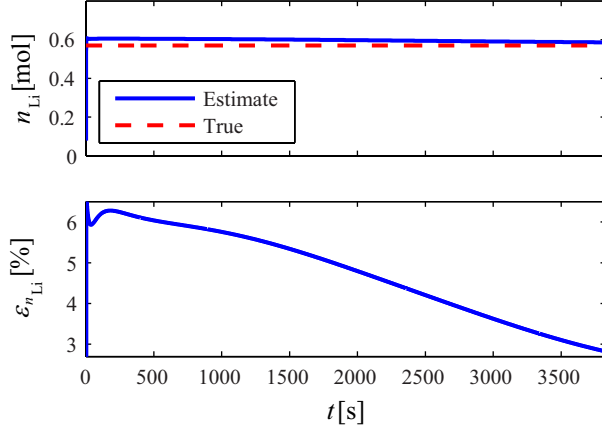


Figure 5.5: (a) The estimate and (b) relative estimation error $\epsilon_{n_{\text{Li}}}$ of the number of cyclable Li-ions n_{Li} under additional modeling error caused by loss of 4% anode active material and 8% cathode active material.

of the number of cyclable Li-ions.

Figure 5.6 shows the effect of re-parameterizations on the estimation accuracy of the number of cyclable Li-ions. The relative estimation errors $\epsilon_{n_{\text{Li}}}$ in Figure 5.6 are obtained under the same level of additional modeling error caused by loss of active materials in the DFN model as in Figure 5.5. However, the parameter set in the SPM in Figure 5.6 is obtained from re-parameterizations, either when the active material loss is at the same level or half of the level as in the DFN model; i.e., the result labelled with 96%n, 92%p in Figure 5.6 uses a parameter set identified from the current and voltage trajectories of the DFN model with 8% and 4% active material loss in the cathode and anode, and the result labelled with 98%n, 96%p uses a parameter set identified with 4% and 2% active material loss in the cathode and anode. $\epsilon_{n_{\text{Li}}}$ are bounded within $[0, 2]\%$ and $[-1.7, -0.9]\%$ for re-parameterization at half of the level (98%n, 96%p) and the same level (96%n, 92%p) as in the DFN model, respectively. Both these relative estimation errors are lower than (approximately 1/3 of) the relative estimation errors in Figure 5.5, which is $[2.7, 6.2]\%$. This result confirms that re-parameterization can improve the estimation accuracy of the number of cyclable Li-ions.

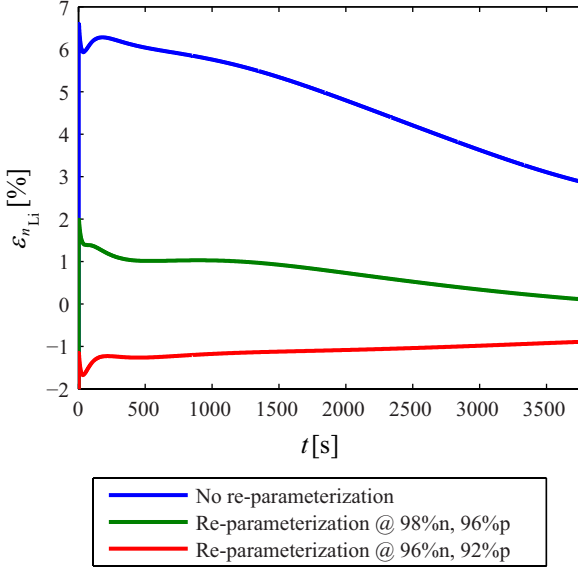


Figure 5.6: The relative estimation errors $\epsilon_{n_{Li}}$ under additional modeling error caused by loss of 4% anode active material and 8% cathode active material using the parameter set identified i) at the beginning of the service life (no re-parameterization), ii) when loss of active material is at half of the level of the modeling error (98% n , 96% p), and iii) when loss of active material is at the same level as the modeling error (96% n , 92% p).

5.6.3 Robustness to Measurement Noise

In this section, the impact of measurement noise on the estimation accuracy is investigated by adding noise to the input and output measurements separately.

This chapter assumes that the measurement noise follows a zero-mean Gaussian distribution,

$$I_{\text{noise}} \sim N(0, \sigma_I^2), \quad (5.26)$$

$$V_{\text{noise}} \sim N(0, \sigma_V^2), \quad (5.27)$$

where I_{noise} and V_{noise} are noise added to the input and output measurements, respectively. In this chapter, it is assumed that the standard deviations satisfy $\sigma_I = 1$ A and $\sigma_V = 0.1$ V. These standard deviations are chosen to test the algorithm with noise levels that exceed what is actually present in most of the equipment available in the market today; i.e., most equipment available in the market can provide more

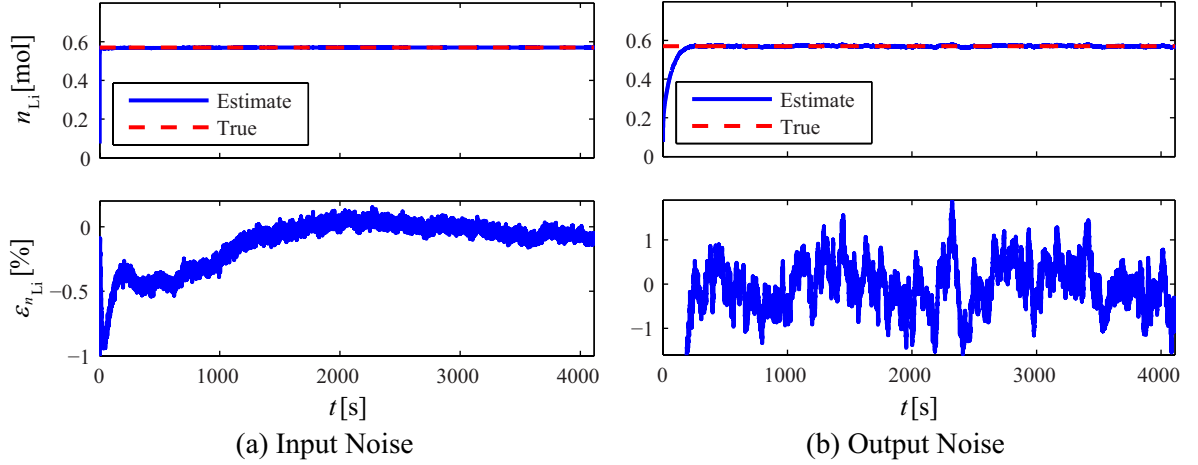


Figure 5.7: The estimate \hat{n}_{Li} and relative estimation error $\epsilon_{n_{\text{Li}}}$ of the number of cyclable Li-ions n_{Li} under the presence of (a) input and (b) output measurement noise.

accurate current and voltage measurements than this level [76]. For the case with output measurement noise, the measurement noise covariance matrix P_ν is increased to 10^5 ; thus the estimation algorithm takes into account that the measurements are not accurate and gives less trust to the measurement.

Figure 5.7 (a) and (b) show the simulation results under only input and output measurement noise, respectively. The relative estimation error $\epsilon_{n_{\text{Li}}}$ is bounded within $[-1, 0.5]\%$ and $[-1.6, 2]\%$ under (a) input and (b) output measurement noise, respectively. These results demonstrate that the number of cyclable Li-ions can be accurately estimated even under the presence of very high measurement noise. To this end, the measurement noise covariance matrix P_ν in the EKF might need to be set to a larger value in the case with output measurement noise.

5.6.4 Combination of Non-Ideal Conditions

This section examines the effect of a combination of the three kinds of non-ideal conditions considered above on estimation of the number of cyclable Li-ions. In this section, estimation results are obtained with i) +1% SOC estimation error, ii) additional modeling error caused by loss of 4% anode active material and 8% cathode

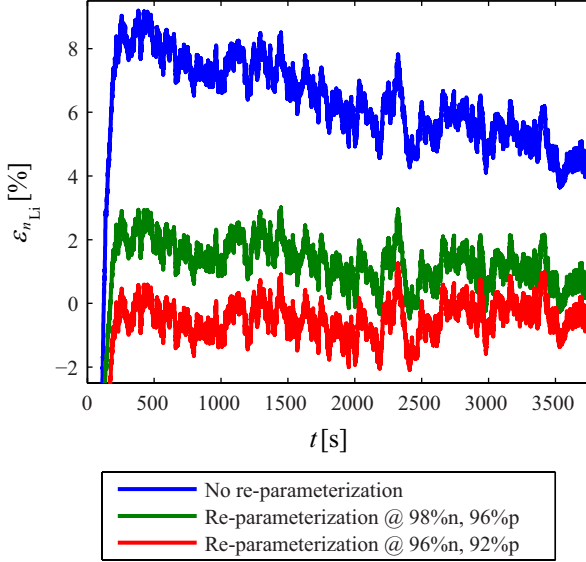


Figure 5.8: The relative estimation errors $\epsilon_{n_{Li}}$ under a combination of non-ideal conditions in Figure 5.4, 5.5, and 5.7 using the parameter set identified i) at the beginning of the service life (no re-parameterization), ii) when loss of active material is at half of the level of the modeling error (98% n , 96% p), and iii) when loss of active material is at the same level as the modeling error (96% n , 92% p).

active material, and iii) input and output noise with standard deviations of 1 A and 0.1 V included into the simulations simultaneously.

Figure 5.8 shows the relative estimation errors $\epsilon_{n_{Li}}$ under the combination of non-ideal conditions using the parameter set identified i) at the beginning of the service life (no re-parameterization), ii) when loss of active material is at half of the level of the modeling error (98% n , 96% p), and iii) when loss of active material is at the same level as the modeling error (96% n , 92% p). Without re-parameterization, $\epsilon_{n_{Li}}$ is bounded within [3.8, 9.5]%. With re-parameterizations, $\epsilon_{n_{Li}}$ is decreased to [-0.2, 3.6]% and [-2, 1.8]% for re-parameterizations at {98% n , 96% p } and {96% n , 92% p }, respectively. The results show that estimation of the number of cyclable Li-ions is robust even when the three non-ideal conditions are present at the same time, and the estimation accuracy can be further improved with re-parameterizations.

5.7 Lower Bounds on Relative Estimation Error and Covariance of Estimates

This section extends the framework developed in Section 3.5 that obtains the lower bounds of the relative estimation error and of the covariance of the estimates of the side reaction current density to estimation of the number of cyclable Li-ions. This extension is possible because estimation of the number of cyclable Li-ions is also achieved by minimizing the error between the voltage measurement and the estimated voltage. Using similar analyses as in Section 3.5, the lower bound of the relative estimation error of the number of cyclable Li-ions is

$$|\epsilon_{n_{\text{Li}}}| = \left| \frac{\hat{n}_{\text{Li}} - n_{\text{Li}}}{n_{\text{Li}}} \right| = \left| \frac{V_{\text{as}}}{s(V|n_{\text{Li}})n_{\text{Li}}} \right|, \quad (5.28)$$

and the lower bound of the covariance of an unbiased estimate of the number of cyclable Li-ions is

$$\text{cov}(\hat{n}_{\text{Li}}) = \frac{\text{cov}(V_{\text{as}})}{s(V|n_{\text{Li}})^2} = \frac{\mathbb{E}(V_{\text{as}}^2)}{s(V|n_{\text{Li}})^2}. \quad (5.29)$$

for unbiased \hat{n}_{Li} and zero mean V_{as} . $s(V|n_{\text{Li}})$ is the sensitivity of the voltage to the number of cyclable Li-ions, which is defined as

$$s(V|n_{\text{Li}}) \triangleq \frac{\partial V}{\partial n_{\text{Li}}}. \quad (5.30)$$

The rest of this section compares the robustness to the same non-ideal conditions of the number of cyclable Li-ions and the side reaction current density by comparing the lower bounds of the relative estimation error and of the covariance of the estimate under the same non-ideal conditions. According to (3.63) and (5.28),

$$\frac{|\epsilon_{n_{\text{Li}}}|}{|\epsilon_{J_{\text{sd}}}|} = \frac{s(V|J_{\text{sd}})J_{\text{sd}}}{s(V|n_{\text{Li}})n_{\text{Li}}} \quad (5.31)$$

under the same V_{as} . $|\epsilon_{n_{\text{Li}}}|$ and $|\epsilon_{J_{\text{sd}}}|$ are the lower bounds for the relative estima-

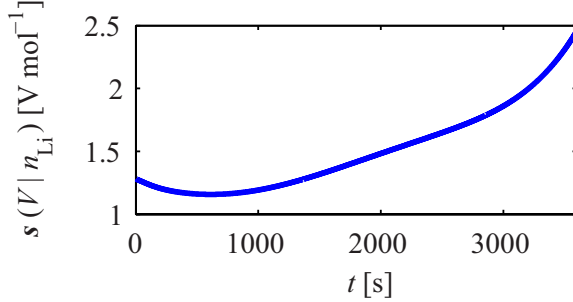


Figure 5.9: The sensitivity of the voltage to the number of cyclable Li-ions, $s(V|n_{\text{Li}})$.

tion errors of the number of cyclable Li-ions and the side reaction current density, respectively. Similarly, according to (3.68) and (5.29),

$$\frac{\text{cov}(\hat{n}_{\text{Li}})}{\text{cov}(\hat{J}_{\text{sd}})} = \frac{s(V|J_{\text{sd}})^2}{s(V|n_{\text{Li}})^2} \quad (5.32)$$

under the same $\text{cov}(V_{\text{as}})$ for unbiased estimates \hat{n}_{Li} and \hat{J}_{sd} .

Both (5.31) and (5.32) requires evaluation of $s(V|n_{\text{Li}})$ and $s(V|J_{\text{sd}})$. Similar to the method used in Section 3.6, the SPM is simulated three times using 1-C constant current charge to obtain the sensitivity of the voltage to the number of cyclable Li-ions. The first time is with the value of all parameters being the same as in the LMO-mixture parameter set used in the true system. The voltage simulated from the first time is denoted as $V_{100\%n_{\text{Li}}}$. Then the SPM is simulated with $\pm 1\%$ perturbation in the value of n_{Li} , and the voltage responses are denoted with $V_{99\%n_{\text{Li}}}$ and $V_{101\%n_{\text{Li}}}$. The SPM is used here instead of the DFN model to keep the distribution of the Li-ion concentration comparable among the three simulations. This is because the same n_{Li} level in the DFN model corresponds to various distributions of the Li-ion concentration inside the battery. This approximation is valid because the voltage response of the DFN model and the SPM is close under 1-C constant current. Then, the sensitivity of the voltage to the number of cyclable Li-ions is approximated by

$$s(V|n_{\text{Li}}) \approx \frac{|V_{100\%n_{\text{Li}}} - V_{99\%n_{\text{Li}}}| + |V_{100\%n_{\text{Li}}} - V_{101\%n_{\text{Li}}}|}{2 \times 1\%n_{\text{Li}}}. \quad (5.33)$$

Figure 5.9 shows the sensitivity of the voltage to the number of cyclable Li-ions.

It can be observed that $s(V|n_{\text{Li}}) = O(10^0)$ V mol $^{-1}$. It can be further observed from Figure 3.11 (a), Figure 5.3, and Figure 3.9 that $s(V|J_{\text{sd}}) = O(10^{-7})$ V m 3 A $^{-1}$, $n_{\text{Li}} = O(10^{-1})$ mol, and $J_{\text{sd}} = O(10^3)$ A m $^{-3}$, respectively. Therefore,

$$\frac{|\epsilon_{n_{\text{Li}}}|}{|\epsilon_{J_{\text{sd}}}|} = \frac{s(V|J_{\text{sd}})J_{\text{sd}}}{s(V|n_{\text{Li}})n_{\text{Li}}} = O(10^{-3}), \quad (5.34)$$

$$\frac{\text{cov}(\hat{n}_{\text{Li}})}{\text{cov}(\hat{J}_{\text{sd}})} = \frac{s(V|J_{\text{sd}})^2}{s(V|n_{\text{Li}})^2} = O(10^{-14}). \quad (5.35)$$

The result shows that the lower bound of the relative estimation error of the number of cyclable Li-ions is three orders of magnitude smaller than the lower bound of the relative estimation error of the side reaction current density, and the lower bound of the covariance of unbiased estimate of the number of cyclable Li-ions is 14 orders of magnitude smaller than the lower bound of the covariance of unbiased estimate of the side reaction current density. This result agrees with the observation that the number of cyclable Li-ions is significantly more robust than the side reaction current density to non-ideal conditions.

5.8 Summary and Conclusions

This chapter presents a method to monitor battery SOH by estimating the number of cyclable Li-ions. The number of cyclable Li-ions is formulated as a battery parameter that affects the voltage response. This parameter is then estimated using the EKF. In this chapter, the battery is modeled with the DFN model with 50 particles per electrode, while the EKF algorithm is designed with the SPM as the model for the battery. As a preparation stage, parameterization of the SPM is performed before estimation of the number of cyclable Li-ions.

The effectiveness of the method is demonstrated through simulation. Two current trajectories for a typical HEV/EV operation cycle is considered in the simulations. The charge trajectory is 1-C CCC, which simulates the fast charging of EVs. The second current trajectory is generated by an EV subject to the UDDS cycle, which simulates the dynamic load condition of HEV/EVs.

First, the number of cyclable Li-ions is estimated under the ideal conditions, i.e., no SOC estimation error, no additional modeling error besides the structural and parameter discrepancies between the DFN model and the SPM, and no measurement noise. Simulations show promising results in estimating the number of cyclable Li-ions for both the charge and discharge modes under the ideal condition; the estimated number of cyclable Li-ions converges to the true value quickly and accurately with relative estimation errors bounded within $[-1, 0.2]\%$ and $[-1.2, 1]\%$ for the two current trajectories.

Then, robustness of the method is tested by estimating the number of cyclable Li-ions under various non-ideal conditions. The performance of the algorithm is tested under the presence of SOC estimation error, additional modeling error, and measurement noise, both individually and combined. In all the cases tested in this chapter, the bounds for the relative estimation error $\epsilon_{n_{\text{Li}}}$ of the number of cyclable Li-ions are within $\pm 10\%$. These results show that estimation of the number of cyclable Li-ions has high robustness against the three considered non-ideal conditions. The result regarding additional modeling error also sheds light on the frequency of parameterization throughout the service life of the battery. Using parameter sets obtained from re-parameterizations performed during the service life of the battery can improve the estimation accuracy of the number of cyclable Li-ions when additional modeling error is introduced by other degradation mechanisms.

Finally, a framework is developed to obtain the lower bounds of the relative estimation error and of the covariance of the estimate of the number of cyclable Li-ions under non-ideal conditions using the same approach as in Chapter 3. This framework is used to compare the lower bounds of the relative estimation error and of the covariance of the estimate of the side reaction current density and the number of cyclable Li-ions under the same non-ideal conditions. This comparison confirms the observation obtained from simulation results that the estimation of number of cyclable Li-ions is significantly more robust than the estimation of side reaction current density to non-ideal conditions.

This chapter makes the following four contributions. First, the number of cyclable

Li-ions is estimated using the EKF to monitor the battery SOH. Specifically, the SPM is used as the system model to simplify the design of the EKF and to balance the trade-off between the requirement for an electrochemical model and the computational complexity suitable for on-line estimation. Second, to make the simulation closer to practice, parameterization of the SPM is performed using the simulation data from the DFN model as a preparation stage. Third, robustness of estimating the number of cyclable Li-ions is tested under various non-ideal conditions such as SOC estimation errors, additional modeling errors, and measurement noise. Finally, a framework is developed to obtain the lower bounds of the relative estimation error and the covariance of the estimate of the number of cyclable Li-ions under non-ideal conditions. Robustness of estimation of the side reaction current density and the number of cyclable Li-ions to the same non-ideal conditions is also compared using this framework. The main conclusion of this chapter is that the number of cyclable Li-ions can be an effective indicator of the battery SOH, because it can i) uniquely indicate the remaining capacity of the battery regardless of the environmental condition and use pattern of the battery, and ii) be accurately estimated even under non-ideal conditions.

Chapter 6

Comparison of the Effectiveness of Estimating Side Reaction Current Density and the Number of Cyclable Li-ions as SOH Indicators

This chapter compares and comments on the effectiveness of estimating the two electrochemical variables, namely the side reaction current density and the number of cyclable Li-ions, as the SOH indicators for EV and HEV batteries. The comparison is first made between the two electrochemical variables. Then the electrochemical-based SOH indicators are compared to the effects-based SOH indicators. The effectiveness explored herein concerns i) the information provided regarding the SOH, ii) the availability via estimation, and iii) the robustness of the estimation under non-ideal conditions. In this section, the effectiveness of the two electrochemical variables are discussed and compared. Then, a recommendation for the more effective electrochemical SOH indicator is made based on the comparison.

6.1 Comparison between Side Reaction Current Density and the Number of Cyclable Li-ions as SOH Indicators

As argued in Chapter 3, the side reaction current density and the number of cyclable Li-ions are correlated because the integral of the side reaction current density over time and across the width of battery anode-separator-cathode sandwich is the loss of the number of cyclable Li-ions. However, this does not mean that the side reaction current density and the number of cyclable Li-ions are interchangeable in practice. Admittedly, if the continuous trajectories of the side reaction current density and the number of cyclable Li-ions are available, the number of cyclable Li-ions can be computed from the side reaction current density and vice versa. However, the continuous trajectories of the side reaction current density and the number of cyclable Li-ions are difficult to obtain, even without considering non-ideal conditions present in practice. Chapter 3 shows that the side reaction current density cannot be estimated accurately during discharge modes. The instantaneous changes of the number of cyclable Li-ions is also too insignificant to capture using a reasonable resolution. Therefore, it is assumed that the side reaction current density cannot be obtained indirectly from the number of cyclable Li-ions, or vice versa.

1. The Information Provided Regarding the SOH

Both the side reaction current density and the number of cyclable Li-ions are generally applicable to capture the SOH changes caused by electrochemical degradation mechanisms that consume cyclable Li-ions, which are the primary degradation mechanisms for EV/HEV batteries such as the LiFePO₄ and LMO-mixture chemistries [31, 27, 28, 73].

The side reaction current density provides more instantaneous information regarding the SOH changes than the number of cyclable Li-ions. The side reaction current density measures the rate of Li-ion consumption, thus giving an instantaneous sense of how fast a battery is degrading at each instant in time.

Therefore, with the information provided by the side reaction current density, damages to batteries can be prevented immediately by stopping the abuse of the batteries as soon as a large side reaction current density is observed. In contrast, the number of cyclable Li-ions, being the integral of the side reaction current density, provides only the total level of degradation over a period of time. As an accumulative quantity, the information provided by the number of cyclable Li-ions does not provide as immediate a warning of fast degradation as the side reaction current density.

Therefore, in terms of the information provided regarding the SOH, the side reaction current density is more effective than the number of cyclable Li-ions because it provides more instantaneous information on the battery SOH changes.

2. The Availability via Estimation

The simulation results in Chapter 3 – 5 show that both the side reaction current density and the number of cyclable Li-ions can be estimated accurately under ideal conditions. Therefore, there is no difference in the effectiveness the side reaction current density and the number of cyclable Li-ions as the SOH indicators from the perspective of the availability via estimation.

3. The Robustness to Non-Ideal Conditions

The number of cyclable Li-ions show large advantage in terms of the robustness to non-ideal conditions over the side reaction current density. Estimation of the side reaction current density is shown to be sensitive to non-ideal conditions that cause errors in the measurement or estimation of the battery voltage. Using the numerical values of the parameters and the battery use patterns herein, to bound the relative estimation errors of the side reaction current density within $\pm 10\%$, the voltage difference caused by non-ideal conditions needs to be less than 0.01 mV for the example LiFePO₄ battery and 10^{-5} mV for the example LMO-mixture battery. These required levels of accuracy for the voltage is three to six orders of magnitude less than what is available in practice. In contrast, the bound for the relative estimation errors of the number of cyclable Li-ions

is at most $\pm 10\%$ even under the presence of all practical non-ideal conditions considered herein. The analysis in Section 5.7 also shows that the lower bound of the relative estimation error of the number of cyclable Li-ions is three orders of magnitude smaller than the lower bound of the relative estimation error of the side reaction current density, and the lower bound of the covariance of unbiased estimate of the number of cyclable Li-ions is 14 orders of magnitude smaller than the lower bound of the covariance of unbiased estimate of the side reaction current density. Moreover, techniques such as re-parameterization can further improve the estimation accuracy of the number of cyclable Li-ions. Therefore, the number of cyclable Li-ions is more effective than the side reaction current density in terms of the robustness to non-ideal conditions.

In conclusion, when only the information provided regarding the SOH and the availability via estimation are considered, the side reaction current density is the more ideal SOH indicator because it provides more instantaneous information regarding the SOH changes and serves as an instant warning for fast degradation, and can be estimated accurately under ideal conditions. However, the number of cyclable Li-ions is the more effective SOH indicator in practice because it can be estimated with reasonable accuracy under practical non-ideal conditions.

6.2 Comparison to Effects-Based SOH Indicators

The electrochemical variables have several benefits when used as SOH indicators compared to the traditional effects-based SOH indicators including providing insights on degradation from the first principles and being less sensitive to changes in environmental conditions and use patterns as discussed in Section 1.1.4. The discoveries in this dissertation also demonstrate that the electrochemical variables not only have the previous discussed benefits but can also be more effective SOH indicators under certain conditions.

The side reaction current density has the following two advantages over effects-based SOH indicators if estimated accurately. First, the side reaction current density

provides indication of instantaneous degradation rate, which is a piece of information that cannot be provided by either the number of cyclable Li-ions or effects-based SOH indicators. Second, the estimation technique developed in this dissertation can also identify the battery health subsystem that produces the side reaction current density. This identified subsystem model can be further used to predict future degradation rate. This model can also be used in predictive control algorithms to assist other battery management functionalities.

The number of cyclable Li-ions is a promising SOH indicator compared to effects-based SOH indicators. First, the number of cyclable Li-ions indicates the capacity of the battery from the first principles. Secondly, the number of cyclable Li-ions can be estimated with reasonable accuracy under non-ideal conditions. Finally, the number of cyclable Li-ions can be estimated using standard algorithms such as the EKF and using simple electrochemical models such as the SPM. The SPM used in this dissertation has only three states. The simplicity of the model and the algorithm alleviates the common concern regarding electrochemical-based SOH indicators that the computational complexity of the electrochemical battery model makes on-line estimation difficult. In particular, the simulations performed in Chapter 5 runs 1000 times faster than real time. Although these simulations is performed with Matlab R2014a in a laptop with a 2.70 GHz CPU and 16.0 GB RAM, the demonstrated computational speed is still very promising for on-board applications.

Chapter 7

Conclusions and Future Work

7.1 Dissertation Summary

This dissertation considers two electrochemical variables, namely the side reaction current density and the number of cyclable Li-ions, and explores their effectiveness as the SOH indicators for EV and HEV batteries. Formulations are provided to estimate these two electrochemical variables from measurements of battery terminal voltage and current. A framework is also developed to obtain the lower bound of relative estimation error and the lower bound of the covariance of unbiased estimates for each of the two variables under non-ideal condition for algorithms that estimate the variable by minimizing the error between measured voltage and estimated voltage. Finally, the two electrochemical variables are compared in terms of their effectiveness both between each other and with effects-based SOH indicators from the aspect of the information the variables provide regarding the SOH, the availability through estimation, and the robustness to non-ideal conditions.

Chapter 2 presents three electrochemical battery models in the literature to prepare for the development of estimation algorithms in Chapter 3 – 5. The three models are categorized into i) the SOC models including the DFN model [51, 52] and the SPM [56, 54] and ii) the SOH model including the Arora model [31]. The three models are selected, combined, and modified differently in Chapter 3 – 5 based on the different requirements of the applications.

Chapter 3 presents a formulation to estimate side reaction current density and identify the health subsystem that produces the side reaction current density using RCSI. The estimation of the side reaction current density is formulated as an inaccessible subsystem identification problem, where the battery health subsystem is treated as an inaccessible subsystem with the side reaction current density as the output. This subsystem is identified using RCSI, and the output of the identified battery health subsystem provides an estimate for the side reaction current density. In this chapter, the True System is modeled with the DFN model with 50 particles per electrode integrated with the Arora model, while the System Model is represented by either the DFN model with 50 or less particles per electrode or the SPM, all integrated with the Arora model. Simulations are performed to obtain estimates under various current profiles. These simulations show that both the battery health subsystem and the side reaction current density can be estimated accurately using RCSI under ideal conditions. Robustness of the algorithm under non-ideal conditions is then analyzed. A framework is developed to obtain the lower bound of the relative estimation error and the lower bound of the covariance of unbiased estimate of the side reaction current density. Estimation of the side reaction current density under non-ideal conditions that cause errors in the measurement or estimation of the battery voltage is shown to be fundamentally difficult because of the limited impact of the side reaction current density to the voltage. Simulation results show that the estimate of the side reaction current density given by RCSI has achieved the established lower bounds for the relative estimation error in all tested situations with parameters of both LiFePO₄ and LMO-mixture batteries.

Chapter 4 develops a new subsystem identification algorithm, the TSF, under the motivation of improving the accuracy of estimating the side reaction current density when SOC estimation errors are present. The TSF can estimate both the subsystem parameter and the persistent main system state estimation error simultaneously for systems that are marginally stable and have weak feedback of the subsystem output. The battery model used in this chapter is a modified SPM integrated with the Arora model. The TSF is first applied to a linear time varying model that is obtained via

linearization of the battery model, and then applied to the nonlinear battery model. All the matrices in the TSF except the matrix E_1 that represents the sensitivity of the voltage to the states are obtained through linearization around the estimates. The simulation results show that the side reaction current density, SOH subsystem model, and the SOC estimation error can be estimated when E_1 is accurately evaluated. Finally, the method for evaluating E_1 for the nonlinear voltage response is presented, along with a discussion of the potential challenges for accurately evaluating E_1 in practice. When the evaluation of E_1 is not accurate, the improvement on the estimation accuracy of the side reaction current density when SOC estimation errors are present is limited. The requirement for accurate evaluation of E_1 presented in Chapter 4 is due to the same reason that an accurate SOC estimation is required in Chapter 3. This chapter shows that the sensitivity of the estimate of the side reaction current density to non-ideal conditions cannot be reduced by modifying the estimation algorithm.

Chapter 5 investigates the estimation of the number of cyclable Li-ions using the EKF. The number of cyclable Li-ions is formulated as a battery parameter that affects the voltage response. This parameter is then estimated using the EKF. In this chapter, the battery is modeled with the DFN model with 50 particles per electrode, while the EKF algorithm is designed with the SPM as the model for the battery. As a preparation stage, parameterization of the SPM is performed before estimation of the number of cyclable Li-ions. During the estimation stage, the number of cyclable Li-ions is first estimated under the ideal conditions, i.e., no SOC estimation error, no additional modeling error besides the structural and parameter discrepancies between the DFN model and the SPM, and no measurement noise. Simulations show promising results in estimating the number of cyclable Li-ions for both the charge and discharge modes under the ideal condition. Then, robustness of the method is tested by estimating the number of cyclable Li-ions under various non-ideal conditions, both individually and combined. The bounds of the relative estimation errors of the number of cyclable Li-ions obtained in simulations under all combinations of non-ideal conditions are smaller than $\pm 10\%$. The results indicate that the number of cyclable

Li-ions can be estimated accurately even under non-ideal conditions. A framework that obtains the lower bound of the relative estimation error and the lower bound of the covariance of unbiased estimate of the number of cyclable Li-ions is developed using the same method as in Chapter 3. This framework is also used to compare the robustness of the number of cyclable Li-ions and the side reaction current density to the same non-ideal conditions. Using a parameter set of an LMO-mixture battery, the lower bound of the relative estimation error of the number of cyclable Li-ions is three orders of magnitude smaller than the lower bound of the relative estimation error of the side reaction current density, and the lower bound of the covariance of unbiased estimate of the number of cyclable Li-ions is 14 orders of magnitude smaller than the lower bound of the covariance of unbiased estimate of the side reaction current density. This result agrees with the observation from simulations that the estimation of number of cyclable Li-ions is more robust to non-ideal conditions than the estimation of side reaction current density.

Chapter 6 compares and discusses the effectiveness of the side reaction current density and the number of cyclable Li-ions as SOH indicators. The comparison is first made between the side reaction current density and the number of cyclable Li-ions. Then, the advantages of using the two electrochemical-based SOH indicators are discussed compared to effects-based SOH indicators such as the capacity and the internal resistance.

7.2 Conclusions and Contributions

The side reaction current density is an ideal SOH indicator if estimated accurately because it provides indication of instantaneous degradation rate that cannot be indicated by other SOH indicators. The estimation technique developed in this dissertation can also identify the battery health subsystem that produces the side reaction current density, which can be used to predict and control future degradation rate. However, estimation of the side reaction current density under practical non-ideal conditions is fundamentally difficult due to the fact that the sensitivity of the voltage

to the side reaction current density and the magnitude of the side reaction current density are both low.

The number of cyclable Li-ions is a promising SOH indicator for battery management systems in practice because it provides an indication of the remaining capacity from the first principles and demonstrates high robustness to non-ideal conditions. The estimation formulation developed herein also demonstrates that number of cyclable Li-ions can be estimated using a standard algorithm and simple models. The simplicity of the model and the estimation algorithm is beneficial for on-line estimation due to the low computational load.

Nevertheless, note that the numerical results in this dissertation are all based on the particular parameter sets and current trajectories used herein. Therefore, the lower bounds of relative estimation errors and of the covariance of unbiased estimate can change with different parameter sets and current trajectories. In practice, the framework developed in Section 3.5 and 5.7 needs to be followed to obtain the lower bound of relative estimation errors and of the covariance of unbiased estimate under the particular parameter set and current trajectory.

This dissertation makes the following contributions.

1. Two original modifications to the existing battery models are presented. (Chapter 2)
 - (a) The Arora model is modified to one linear static equation with all parameters lumped into one. This formulation provides a simple representation of the complicated SOH process. The linearity of the subsystem model also allows easy combination of several degradation mechanisms [77, 65].
 - (b) An analytical solution of the current densities in the SPM integrated with the Arora model is provided [65].
2. Estimation problems of two health-relevant electrochemical variables, the side reaction current density and the number of cyclable Li-ions, are formulated and estimation algorithms are designed [77, 65, 78, 79]. (Chapter 3 and 5)

- (a) The side reaction current density is estimated as a direct SOH indicator for the first time.
 - (b) The side reaction current density is estimated and the subsystem the produces the side reaction current density is identified using RCSI.
 - (c) The number of cyclable Li-ions is estimated using the EKF to monitor the battery SOH.
 - (d) To make the simulation closer to practice, parameterization of the SPM is performed using the simulation data from the DFN model, instead of using the same parameter values in both the DFN model and the SPM.
3. A new subsystem identification algorithm, the TSF, is developed and applied to estimation of the side reaction current density under the presence of SOC estimation errors [80]. (Chapter 4)
- (a) The TSF is developed based on RCSI and can be applied to estimate the subsystem parameter and output, as well as the persistent main system state estimation error in any system that is marginally stable and with weak feedback of the subsystem output.
 - (b) The TSF is applied to estimate the side reaction current density in the battery under the presence of the SOC estimation error when the sensitivity of the voltage to the state can be accurately approximated.
 - (c) The method for obtaining approximation of the sensitivity of the voltage to the state through voltage responses is presented.
 - (d) The challenges for applying the TSF in practice to estimate the side reaction current density with E_1 evaluated using this method are identified. These challenges verify that the high sensitivity of the estimate of the side reaction current density to SOC estimation error is a fundamental problem caused by the fact that the side reaction current density has low impact on the voltage, and cannot be solved by changing estimation algorithms.

4. A framework is developed to analyze the robustness of estimation of the two electrochemical variables by obtaining the lower bound of relative estimation error and the lower bound of the covariance of unbiased estimates under non-ideal condition for algorithms that estimate the variable by minimizing the error between measured voltage and estimated voltage. [77, 78, 79]. (Chapter 3 and 5)
 - (a) The lower bound of the relative estimation error of a variable is determined to be proportional to the voltage error caused by non-ideal conditions, and inversely proportional to the sensitivity of the voltage to the variable and the magnitude of the variable itself.
 - (b) The framework is shown to provide the same lower bound of the covariance of unbiased estimate as the bound given by the Fisher information.
 - (c) Estimation of the side reaction current density under non-ideal conditions is identified to be fundamentally difficult using this framework because of the sensitivity of the voltage to the side reaction current density and the magnitude of the side reaction current density are both low.
 - (d) The number of cyclable Li-ions is shown to be more robust to the same non-ideal conditions than the side reaction current density because the lower bounds of the relative estimation error and the covariance of unbiased estimates of the number of cyclable Li-ions are significantly lower than the side reaction current density under the same non-ideal conditions.
5. The effectiveness of estimating the side reaction current density and the number of cyclable Li-ions as SOH indicators is discussed through comparison. (Chapter 6)
 - (a) The side reaction current density is identified to be an ideal SOH indicator when it can be estimated accurately, because it can instantaneously indicate battery degradation rate that cannot be captured by other SOH indicators.

- (b) The number of cyclable Li-ions is identified to be a promising SOH indicator for battery management systems in practice because it provides an indication of remaining capacity from the first principles, can be estimated using a standard algorithm and simple models, as well as demonstrates high robustness to non-ideal conditions.

7.3 List of Publications

The following list provides the papers published based on the work present in this dissertation, and the awards received for each paper if applicable.

1. **X. Zhou**, J. L. Stein, and T. Ersal, "Battery State of Health Monitoring by Estimation of the Number of Cyclable Li-ions," *Control Engineering Practice* (in review). [78]
2. **X. Zhou**, D. S. Bernstein, J. L. Stein, and T. Ersal, "Battery State of Health Monitoring by Side Reaction Current Density Estimation via Retrospective - Cost Subsystem Identification," *Journal of Dynamic Systems, Measurement, and Control* (to appear). doi: 10.1115/1.4036030. [77]
3. **X. Zhou**, J. L. Stein, and T. Ersal, "Battery State of Health Monitoring by Estimation of the Number of Cyclable Li-ions," *Proceedings of ASME Dynamic Systems and Control Conference*, Minneapolis, MN, 2016. **[Best Student Paper Award Finalist, ASME Energy Systems Technical Committee Best Paper Award Finalist]** [79]
4. **X. Zhou**, T. Ersal, J. L. Stein, and D. S. Bernstein, "A Subsystem Identification Technique towards Battery State of Health Monitoring under State of Charge Estimation Errors," *Proceedings of American Control Conference*, pp. 1812-1817, Chicago, IL, 2015. [80]
5. **X. Zhou**, T. Ersal, J. L. Stein, and D. S. Bernstein, "Battery State of Health Monitoring by Side Reaction Current Density Estimation via Retrospective -

Cost Subsystem Identification," *Proceedings of ASME Dynamic Systems and Control Conference*, pp. V001T19A002 (10 pages), San Antonio, TX, 2014.
[Best Student Paper Award Finalist] [65]

6. X. Zhou, T. Ersal, J. L. Stein, and D. S. Bernstein, "Battery Health Diagnostics using Retrospective-Cost System Identification: Sensitivity to Noise and Initialization Errors," *Proceedings of ASME Dynamic Systems and Control Conference*, pp. V003T42A004 (10 pages), Palo Alto, CA, 2013. [Best Student Paper Award Finalist] [43]

7.4 Future Extensions

7.4.1 Inclusion of Thermal Impact

A potential limitation regarding the results herein is that the simulations are performed under the isothermal condition. In reality, temperature varies as the battery charges and discharges [81, 82, 83]. Temperature affects the diffusion of Li-ions as well as intercalation reactions in battery as shown in the DFN model and the SPM, which further determines the voltage response of the battery. The difference in voltage response can affect the estimates of the side reaction current density and the number of cyclable Li-ions. On the other hand, changes in operating temperature also affect the degradation process [27, 84, 21, 30], and thus a changing temperature may result in a changing health subsystem parameter θ in estimation of the side reaction current density, which can affect the accuracy of the estimation of the side reaction current density, although given the very fast convergence shown in the results herein it is expected that the challenge presented by this changing parameter to the estimation of the side reaction current density is limited. A more complete study can be performed incorporating thermal dynamics and cooling conditions by applying similar methods to electrochemical-thermal models [85, 86]. Because of the explicit inclusion of temperature in electrochemical-thermal models, the estimates of electrochemical variables can take into account distribution and changes of the temperature, and

achieve better accuracy in indicating battery SOH.

7.4.2 Estimation of Current Densities in Other Battery Degradation and Safety Problems

Some other battery degradation and safety problems are also caused by reactions in batteries whose rate can also be measured by current densities of corresponding reactions. For example, Lithium plating [87, 88, 47], a degradation mechanism usually caused by over-discharge of the battery, and dendrite formation [89, ?, 90, 91], a serious safety concern of the battery, are both caused by reactions inside the battery. The RCSI-based technique developed in Chapter 3 can be applied to both Lithium plating and dendrite formation to estimate the current density of these reactions. These estimates can be used to instantaneously indicate the rate of the deposition of Lithium on electrodes and the formation of dendrites inside the battery, which can be used as an immediate warning to prevent significant or even disastrous damage to the battery.

7.4.3 Experimental Validation

This dissertation established that the number of cyclable Li-ions is the more effective electrochemical SOH indicator that can be accurately estimated under both ideal and non-ideal conditions. An on-going effort that follows the work presented in this dissertation is to experimentally validate the technique developed in this dissertation that estimates the number of cyclable Li-ions. This section lays out the procedures for the experiments conducted to validate the techniques presented in Chapter 5.

Six batteries made by Dr. Greg Less in the Energy Institute at the University of Michigan are obtained for the experiments.

The experiments are divided into two parts. The first part uses electrochemical methods to obtain necessary electrochemical information for the parameterization of the batteries. The second part conducts the battery cycling experiments to obtain i) dynamic charge and discharge trajectories of the current and voltage for parame-

terization and ii) charge and discharge trajectories of the current and voltage after the batteries degrade to different levels to estimate the number of cyclable Li-ions in different degradation levels.

7.4.3.1 Electrochemical Parts

In order for the parameterization in Section 5.4 to succeed, the two assumptions in Section 5.4.1 needs to be satisfied; i.e., i) the functions $U_{\text{ref},j}(\theta_j)$ and ii) θ_j at the beginning and end of the 1-C CCC and UDDS modes are known. If the functions $U_{\text{ref},j}(\theta_j)$ and the capacity match of the electrodes are known, θ_j at the beginning and end of the 1-C CCC and UDDS modes can be obtained by resting the batteries at the beginning and end of the cycle for a prolonged period of time and measure the open circuit voltage (OCV) [92]. Therefore, the electrochemical part of the experiments focuses on obtaining the functions $U_{\text{ref},j}(\theta_j)$ and the capacity match of the electrodes. Because $c_{s,\text{max},j}$ can be calculated theoretically, obtaining $U_{\text{ref},j}(\theta_j)$ is equivalent to obtaining $U_{\text{ref},j}(c_{s,j})$.

- Method 1: Inductively Coupled Plasma

This method obtains $U_{\text{ref},j}(c_{s,j})$ in two steps. The first step obtains the pointwise relationship between $c_{s,j}$ and the SOC using the inductively coupled plasma (ICP) [93, 94, 95]. Six batteries are charged to 0%, 20%, 40%, 60%, 80%, and 100% SOC levels, respectively. Then, the materials anode and cathode of the six batteries are harvested and the Li-ion concentrations of the harvested electrode samples are measured using the ICP. These measurements yields a map between the Li-ion concentration and the SOC at 0%, 20%, 40%, 60%, 80%, and 100% SOC levels. A continuous function between the Li-ion concentration and the SOC in the range of [0%, 100%] SOC can be fit from these six points.

The second step discharges the battery using 1/20 C current and measures the OCV of the battery [36, 92]. Then with $U_{\text{ref},n}(\theta_n)$ for the graphite anode from the literature [30, 3], $U_{\text{ref},p}(\theta_p)$ can be computed by subtracting $U_{\text{ref},n}(\theta_n)$ from the OCV.

This method has the following disadvantages. First, the capacity match of the battery cannot be measured, but only estimated empirically or obtained from the literature. However, different batteries have different capacity match to the discretion of manufactures, and thus it is difficult to estimate capacity match from other batteries even if the battery chemistry is the same. Second, the Li-ion concentrations measured by the ICP using this method can be inaccurate because the samples contain the Li-ion residue from the electrolyte and the SEI film that give a bias to the measured Li-ion concentration. Because of these disadvantages, the second method is introduced.

- Method 2: Three-Electrode T-Type Cell

A three-electrode T-Type cell [96] can be constructed with uncycled battery anode and cathode samples that are capacity matched and a reference electrode. The Li-ion concentration and the potential of the two electrodes can be measured simultaneously when this three-electrode cell is discharged with Galvanostatic Intermittent Titration Technique (GITT) [96] or 1/20 C constant current. These measurements can provide i) the continuous functions $U_{\text{ref},j}(c_{s,j})$ and ii) capacity match at the same time. Because the electrode samples are obtained directly from uncycled sheets but not from cycled cells, the samples are free from the electrolyte residue and SEI film, and thus gives more accurate measurements. Moreover, the actual capacity match is measured in this method, unlike the first method where the capacity match is estimated empirically or obtained from the literature.

7.4.3.2 Cycling Part

The second part cycles the batteries to obtain the trajectories of the current and voltage for parameterization and estimation of the number of cyclable Li-ions. The trajectories for parameterization is obtained with fresh batteries using 1-C CCC, pulse series, and UDDS cycles. The batteries are then degraded using CCCV cycles or cycles designed in [97] to different capacity levels. The number of cyclable Li-ions is

estimated using trajectories of the current and voltage under different capacity levels.

7.4.3.3 Validation

This study assumes that the electrochemical degradation mechanism that consumes the cyclable Li-ions is the primary degradation mechanism in the battery. Therefore, the decrease in the capacity of the battery should follow the same trend as the decrease of the number of the cyclable Li-ions. Hence, the algorithm is validated when the capacity and the estimate of the number of the cyclable Li-ions follow the same trend.

Another validation method can be the in-situ measurement of the bulk Li-ion concentration using the neutron imaging [48]. The measured bulk Li-ion concentration can then be converted into the number of cyclable Li-ions by multiplying with the total volume of the battery. However, this method requires a lot of resources and may not always be applicable in practice.

Appendix A

The Values of the Electrochemical Parameters and Functions Used in the Simulations

The numerical values of the electrochemical parameters and functions in the battery models are essential for the simulation results and numerical analysis presented in this dissertation, and are thus included in this Appendix.

A.1 Battery Parameters

The numerical values of the parameters of the SOC model for the LiFePO₄ battery used in Chapter 3 are obtained from [63, 64], while the values for the LMO-mixture battery used in Chapter 4 and 5 are obtained from [3]. These numerical values are all obtained through system identification using experimental data for cycling batteries of the respective chemistry. The parameters of the SOH model is obtained from [28] for both the LiFePO₄ and LMO-mixture batteries. Although the parameters in [28] are designed for the LiFePO₄ battery only, the numerical values of $i_{0,\text{sd}}$ and $U_{\text{ref},\text{sd}}$ for the LMO-mixture battery are set the same as the LiFePO₄ battery herein because [3] does not consider the side reactions.

Variable	LiFePO ₄ [63, 64, 28]	LMO-mixture [3]
A [m ²]	0.3108	1.0452
L_n [m]	2.8853E-5	5.00E-5
L_p [m]	6.5205E-5	2.54E-5
L_{sep} [m]	1.6971E-5	3.64E-5
R_n [m]	3.5961E-6	1.00E-6
R_p [m]	1.6371E-5	1.00E-6
$\epsilon_{s,n}$	0.381	0.58
$\epsilon_{s,p}$	0.48	0.50
$\epsilon_{e,n}$	0.619	0.332
$\epsilon_{e,p}$	0.52	0.33
$\epsilon_{e,sep}$	0.3041	0.50
$D_{s,n}$ [m ² s ⁻¹]	8.2557E-14	2.00E-16
$D_{s,p}$ [m ² s ⁻¹]	1.7362E-14	3.7E-16
t^+	0.2495	0.363
$c_{s,max,n}$ [mol m ⁻³]	2.9482E4	1.61E+4
$c_{s,max,p}$ [mol m ⁻³]	1.0355E4	4.1E+4
R_{film} [Ω m ²]	2E-10	0.002
c_e [mol m ⁻³]	1.2669E3	1.20E+3
$i_{0,n}$ [A m ⁻²]	- ^a	36
$i_{0,p}$ [A m ⁻²]	- ^a	26
k_n [A m ⁴ mol ⁻²]	8.6963E-7	- ^b
k_p [A m ⁴ mol ⁻²]	1.1267E-7	- ^b
$i_{0,sd}$ [A m ⁻²]	1.5E-6	1.5E-6 ^c
$U_{ref,sd}$ [V]	0.4	0.4 ^c
F [C mol ⁻¹]	96487	96487
R [J mol ⁻¹ K ⁻¹]	8.314	8.314
α	0.5	0.5

^a For the LiFePO₄ battery, $i_{0,j} = k_j[(c_{s,max,j} - c_{se,j})c_{se,j}c_{e,j}]^\alpha$.

^b Because $i_{0,j}$ in the LMO-mixture battery is given, there is no need for k_j .

^c [3] does not consider the side reactions, so the numerical values of $i_{0,sd}$ and $U_{ref,sd}$ for the LMO-mixture battery are set the same as the LiFePO₄ battery herein.

Table A.1: The numerical values of the parameters for the LiFePO₄ battery used in Chapter 3 and the LMO-mixture battery used in Chapter 4 and 5.

A.2 Functions for Reference Potential

The reference potential functions $U_{\text{ref},p}(\theta_p)$ and $U_{\text{ref},n}(\theta_n)$ depend on the materials of the electrodes. For the LiFePO₄ battery used in Chapter 3, the reference potentials are [30]

$$U_{\text{ref},p}(\theta_p) = 3.4323 - 0.8428e^{-80.2493(1-\theta_p)^{1.3198}} - 3.2474 \times 10^{-6}e^{20.2645(1-\theta_p)^{3.8003}} + 3.2482 \times 10^{-6}e^{20.2646(1-\theta_p)^{3.7995}}; \quad (\text{A.1})$$

$$\begin{aligned} U_{\text{ref},n}(\theta_n) = & 0.6379 + 0.5416e^{-305.5309\theta_n} + 0.044 \tanh \frac{\theta_n - 0.1958}{-0.1088} \\ & - 0.1978 \tanh \frac{\theta_n - 1.0571}{0.0854} - 0.6875 \tanh \frac{\theta_n + 0.0117}{0.0529} \\ & - 0.0175 \tanh \frac{\theta_n - 0.5692}{0.0875}. \end{aligned} \quad (\text{A.2})$$

For the LMO-mixture battery used in Chapter 4 and 5 are [3]

$$\begin{aligned} U_{\text{ref},p}(\theta_p) = & 85.681\theta_p^6 - 357.7\theta_p^5 + 613.89\theta_p^4 - 555.65\theta_p^3 + 281.06\theta_p^2 - 76.648\theta_p \\ & - 0.30987 \exp(5.657\theta_p^{115.0}) + 13.1983; \end{aligned} \quad (\text{A.3})$$

$$\begin{aligned} U_{\text{ref},n}(\theta_n) = & 8.00229 + 5.0647\theta_n - 12.578\theta_n^{1/2} - 8.6322 \times 10^{-4}\theta_n^{-1} + 2.1765 \times 10^{-5}\theta_n^{3/2} \\ & - 0.46016 \exp[15.0(0.06 - \theta_n)] - 0.55364 \exp[-2.4326(\theta_n - 0.92)]. \end{aligned} \quad (\text{A.4})$$

Appendix B

Robustness of Estimation of SEI Film Resistance using RCSI

B.1 Introduction

This appendix presents the contents of [43], which is a part of my battery-health-relevant research but is not included in the main body of this dissertation. This work extends the work in [42] that estimates the SEI film resistance using RCSI by studying via simulations the robustness of estimation of SEI film resistance using the formulation in [42]. In particular, the sensitivity of the estimate to measurement noise and initialization errors is studied. These contents are not included in the main body of this dissertation because the SEI film resistance is not a SOH indicator that is generally applicable to all primary degradation mechanisms as argued in Chapter 1.

SEI film resistance can be considered as a SOH indicator in the degradation mechanism of SEI film formation. Direct measurements of the SEI film growth require invasive methods that destroy the battery and are thus not applicable during the lifetime of the battery. Therefore, similar to the side reaction current density in Chapter 3, the dynamics of SEI film growth constitute an inaccessible subsystem in the battery, and thus RCSI [57, 58, 59, 60] is used as the algorithm to estimate the SEI film resistance and identify the subsystem that produces the SEI film as the output.

The battery model used in this work is the DFN model [51, 52] augmented with the Ramadass battery-health model [28] (DFN+R). The Ramadass model is an extension of the Arora model presented in Section 2.3 to the SEI film formation mechanism. The Ramadass model contains two components: i) the Li-consumption component, which is the Arora model, and ii) the film-growth component. The film-growth component models the creation of the SEI film from the side reaction. First, the side reaction creates the SEI film at a rate proportional to the side reaction current density, that is,

$$\frac{\partial \delta_{\text{film}}}{\partial t} = -\frac{J_{\text{sd}} M_{\text{SEI}}}{a_n \rho_{\text{SEI}} F} \quad (\text{B.1})$$

The SEI film then adds to the internal resistance of the anode, thereby negatively affecting battery performance as modeled by

$$R_{\text{film}} = R_{\text{SEI}} + \frac{\delta_{\text{film}}}{\kappa_p^{\text{eff}}}. \quad (\text{B.2})$$

In the formulation presented in [42], the DFN+R model is considered as the true system, with the DFN model together with the Li-consumption component of the Ramadass model as the main system, and the film-growth component of the Ramadass model as the unknown subsystem. Therefore, J_{sd} is formulated as the input to the subsystem that is computed in the main system, while RCSI's task is to identify a model that represents (B.1) and (B.2) and to estimate the output R_{film} .

[42] has illustrated the applicability of the RCSI method to the film formation problem; however, a seventh order subsystem model structure was used, which is relatively high, and it was assumed that there were no noise or modeling errors. Hence, it is unknown how RCSI will perform with low order subsystem model structures and under the presence of noise and modeling errors. To address this gap, [43] aims to study the performance of RCSI in identifying film growth when a first-order model structure is assumed as the subsystem model, including cases when there is noise in input or output measurements, or when there are initialization errors in the main system model.

B.2 Simulation under Ideal Conditions

This section presents a numerical simulation of the application of RCSI to the film-growth identification problem. The DFN+R model is simulated under repeated Constant-Current, Constant-Voltage (CCCV) cycling from 2 to 3.6 V at a 2.5 C-rate to produce the current and voltage from the true system. The parameters for the DFN model are taken from [63]. For the Ramadass model the parameters are assumed to be $u_{\text{sd},\text{ref}} = 0.4$, $i_{0,\text{sd}} = 4 \times 10^{-9}$, $M_{\text{SEI}} = 7.3 \times 10^4$, $\rho_{\text{SEI}} = 2.1 \times 10^3$, and $\kappa_p^{\text{eff}} = 1$. The film-growth subsystem is then removed from the DFN+R model in accordance with the assumption that it is unknown. RCSI is then tasked with identifying the dynamics of the unknown film-growth subsystem. The controller and tuning parameters are chosen to be $P(0) = 5 \times 10^{-7}$, and $\tilde{\mathcal{H}} = [\hat{H}_1]$, where $\hat{H}_1 = 0.01$. Finally, $\alpha(k) = 1$ at the start of each cycle, that is, $P(k)$ and $\theta(k)$ are re-initialized at the start of each charging cycle. The order of the subsystem model is chosen to be 1, which is the same as the order of the subsystem. Note that this is in contrast to [42], where the order of the subsystem model is 7. In this section, initial conditions in the truth system and the system model are identical, where the concentration in the electrolyte is set at $c_e = 1.2669 \times 10^3 \text{ mol m}^{-3}$ and the concentration in anode and cathode are chosen to be $c_{s,n} = 0.8408 \text{ mol m}^{-3}$ and $c_{s,p} = 0.1592 \text{ mol m}^{-3}$, respectively. The sample time is chosen to be $T = 0.2 \text{ s}$.

Figure B.1 shows the true film resistance as given by DFN+R model and the film resistance as estimated by RCSI. The film resistance estimates show that the film-resistance subsystem dynamics are not identifiable during the discharging and constant voltage charging intervals; i.e., intervals of operation within which the intercalation side current J_{sd} is close to zero. However, in the constant current charging phase when J_{sd} is large, RCSI produces a useful estimate of the film resistance that is close to the true film resistance. This is consistent with the previous work [42] that studied the identifiability of the film growth in different modes in CCCV cycles based on Fisher information and found that the film resistance is identifiable only during constant current charging phase. Physically, overpotential between side reaction and

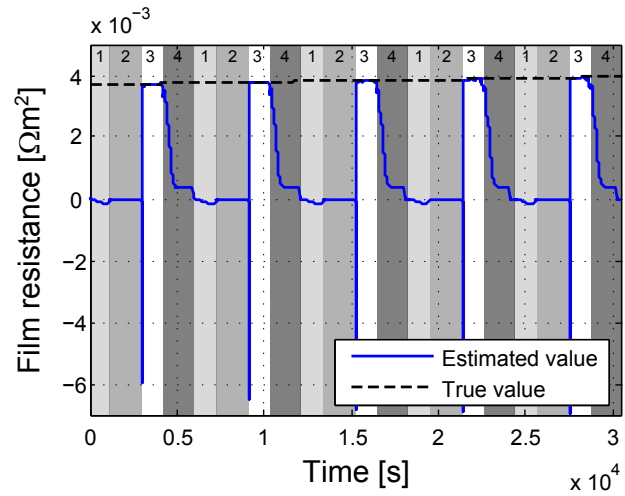


Figure B.1: True film resistance and the film resistance estimated by RCSI. Shaded regions 1–4 indicate the constant current discharging mode, constant voltage discharging mode, constant current charging mode, and constant voltage charging mode, respectively.

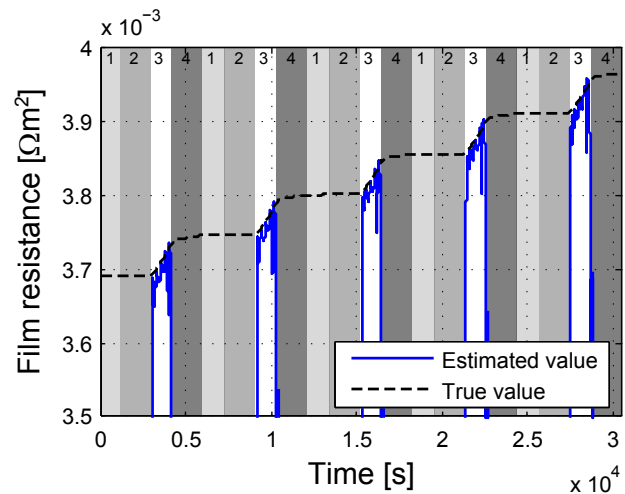


Figure B.2: A magnified view of Figure B.1.

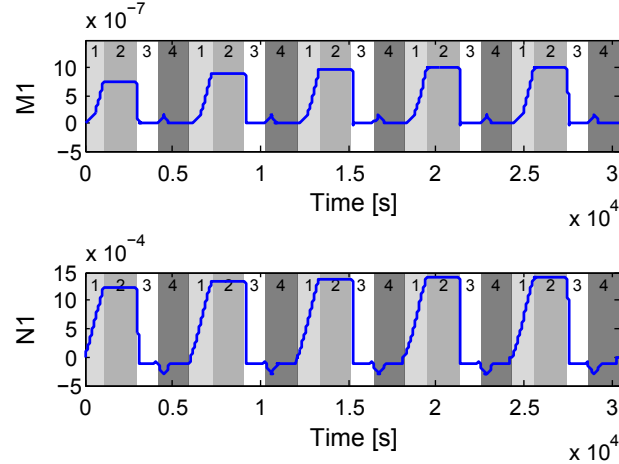


Figure B.3: Identified θ by RCSI.

intercalation reaction is much higher in charging modes, which leads to a much more significant film growth in charging modes than discharging modes. Moreover, the film growth rate in constant voltage charging mode is much smaller than in constant current charging mode. Thus, the film resistance is more identifiable in constant current charging mode. Figure B.2 provides a magnified view of Figure B.1, which shows that the estimates of film resistance provided by RCSI correspond closely to the true film resistance during intervals in which J_{sd} is large. This performance is as good as that of the seventh-order model considered in [42].

Figure B.3 shows the identified θ in simulation. The identified M_1 , i.e., the pole, has an order of magnitude of 10^{-7} , and the identified N_1 , i.e., the gain, has an order of magnitude of 10^{-4} . Note that the differential equations in the Ramadass film-growth model are also describing a first order system, so the true θ can be obtained as $[M_1, N_1]^T = [1, -2.3712 \times 10^{-10}]^T$. Thus, the identified θ is not the same as the true θ in the subsystem, even though the identified model can track the film resistance well.

To investigate this parameter convergence issue further, the film-growth subsystem is isolated from the main system and identified through standard recursive least squares (RLS), which is a special case of the Kalman filter, using the \hat{u} and \hat{y}_0 recorded during the simulations with RCSI and using a range of values for $P(0)$. Fig. B.4 shows

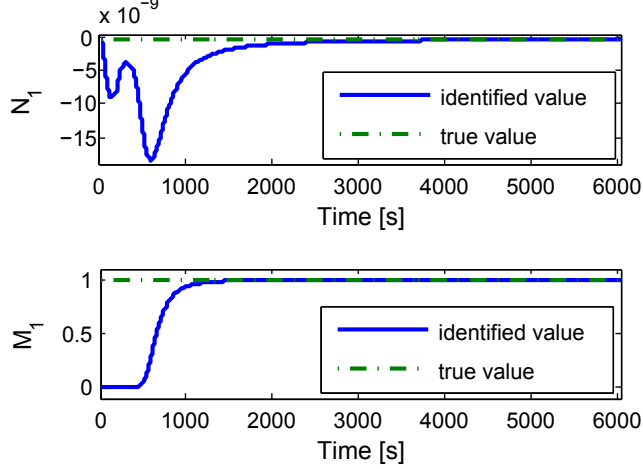


Figure B.4: Identified θ by RLS when $P(0) = 1 \times 10^{10}$.

the identified results using $P(0) = 10^{10}$ as opposed to the $P(0) = 5 \times 10^{-7}$ in RCSI in Figs. B.1 and B.2 . As can be seen in the figure, with $P(0) = 10^{10}$, RLS can identify the true parameters accurately. However, when $P(0) = 10^{10}$ in RCSI, it leads to a singularity in the battery model. The precise cause of this singularity is currently unknown, but is subject to future research. When the singularity issue is resolved, it can be expected that RCSI will also be able to identify the subsystem parameters accurately.

B.3 Sensitivity to Measurement Noise

The previous section showed that film resistance can be estimated accurately during the constant current charging mode, when current is the input and voltage is the output of the Main System. Since the film grows mainly during constant current charging, it is possible to conceive a use scenario in which RCSI is activated only during the constant current charging mode and deactivated during the other modes. Therefore, in this section, the impact of noise is investigated only for the constant current charging mode.

B.3.1 Sensitivity to Output Measurement Noise

The approach used to analyze the effect of output noise can be briefly summa-

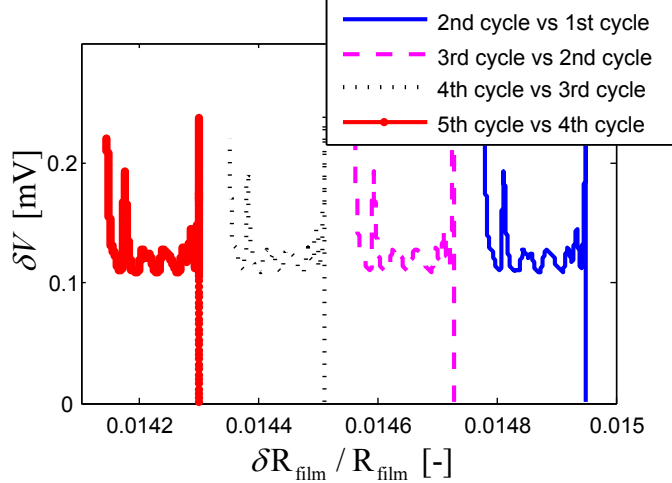


Figure B.5: Voltage change vs. relative film resistance growth between successive cycles.

rized as follows. The truth system is simulated first for five successive CCCV cycles to obtain the relationship between the true voltage change and true film growth. Successive cycles are compared pairwise to identify the change in voltage as a function of the relative change in film resistance. Then, the maximum standard deviation of noise is set to the same order of magnitude as the voltage change and the performance of RCSI is analyzed.

Figure B.5 shows how film resistance grows and voltage changes in successive cycles in the truth system. The film resistance increases by about 1.5%, while the voltage changes by about 0.1-0.2 mV. This result indicates that if we apply a noise with standard deviation in the level of 0.1 mV, the noise level will be comparable to the change in voltage from cycle to cycle that the measurements need to detect. Hence, 0.2 mV is used as an upper limit of the standard deviation of the noise considered in the output of the system model.

Figure B.6 shows the identification result during five successive cycles after applying an output measurement noise with standard deviation of 0.02 mV, one tenth of the upper limit identified above. The conclusion is that an output measurement noise with standard deviation of 0.02 mV is small enough for an accurate identification.

Figure B.7 shows the identification result during five successive cycles after apply-

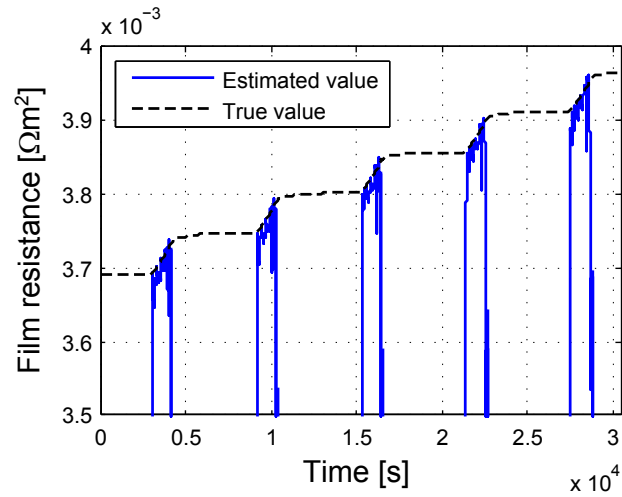


Figure B.6: A magnified view of film resistance identification with output measurement noise when the standard deviation of the noise is 0.02 mV.

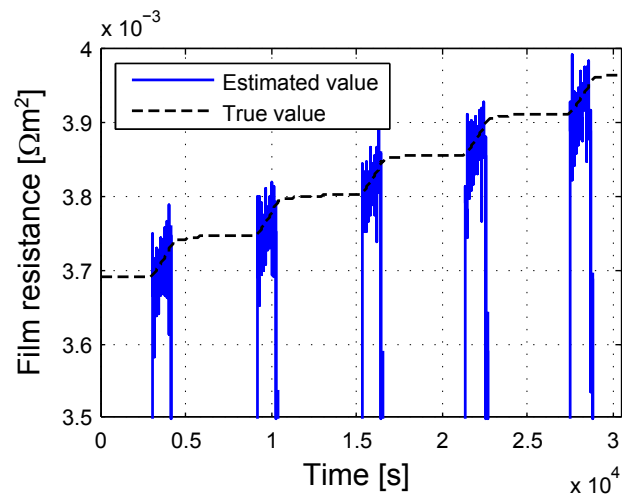


Figure B.7: A magnified view of film resistance identification with output measurement noise when the standard deviation of the noise is 0.2 mV.

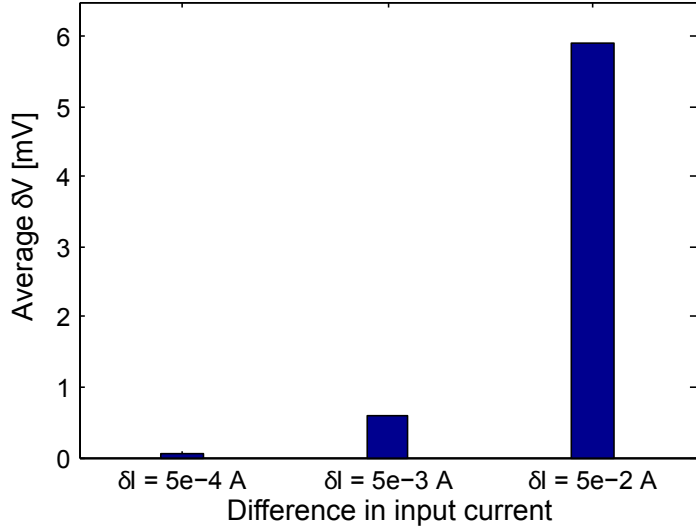


Figure B.8: The difference in output voltage for various differences in input current.

ing output measurement noise with standard deviation of 0.2 mV. The identified film resistance varies between the true film resistance of the previous cycle and the next cycle, with a change that is less than 1.5% of the film resistance of the current cycle. The result indicates that the film resistance estimates degrade as measurement noise approaches the magnitude of the voltage change between successive charging cycles; however, the algorithm can still estimate the film resistance within 1.5% of its true value.

B.3.2 Sensitivity to Input Measurement Noise

In this section, the sensitivity of output voltage to input current is investigated first to identify the difference in current that yields a difference in voltage comparable to the voltage difference in successive cycles found in the previous subsection. This difference in current is then used to define an upper limit for the standard deviation of the input noise when the performance of RCSI is simulated with input noise.

Figure B.8 shows the difference in output voltage when different currents are applied to the truth system. From left to right, the applied currents are 2.4995 A, 2.495 A, and 2.45 A, respectively. The output voltage is compared to the output voltage when applied current is 2.50 A. The difference between output voltage is

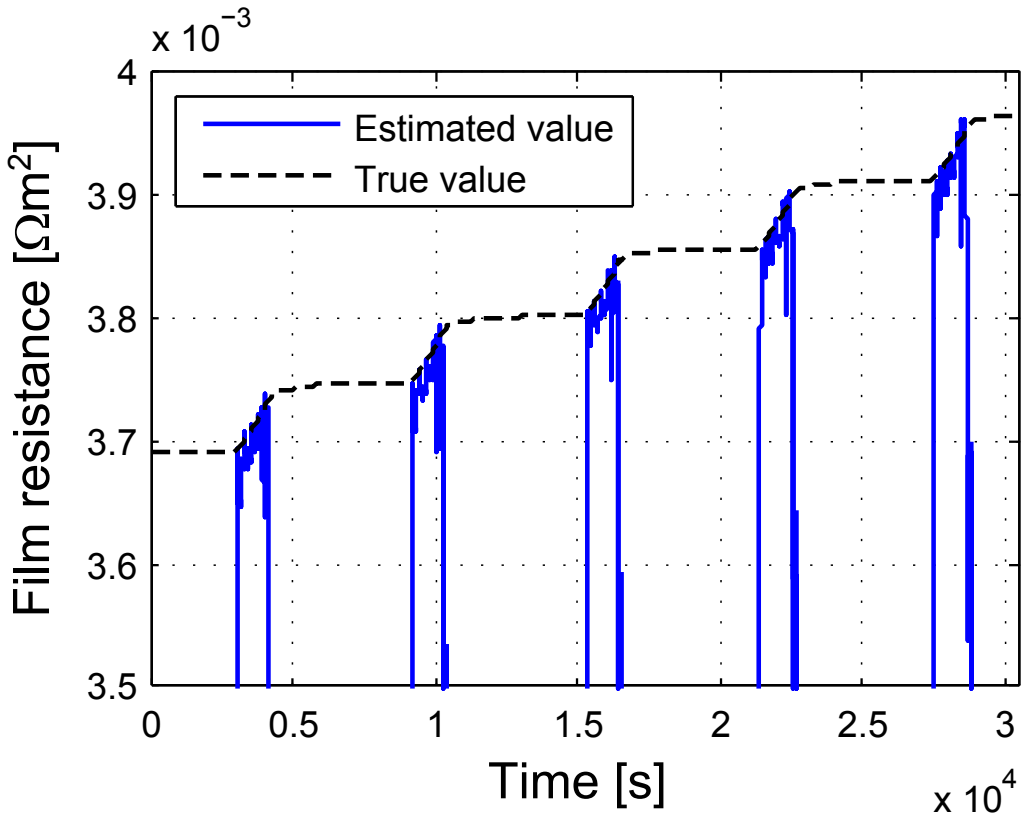


Figure B.9: A magnified view of film resistance identification with input noise when the standard deviation of the noise is 0.5 mA.

growing with the input current decreasing from 2.50 A. When applied current is 2.495 A, whose difference from 2.50 A is 5 mA, the difference of output voltage is on the order of 0.1 mV, which is the same as the output voltage difference between two successive cycles from the previous subsection. Hence, 5 mA is chosen as the upper limit of the standard deviation of the noise considered in the input current.

Figure B.9 shows the identification result during five successive cycles after applying input measurement noise with standard deviation of 0.5 mA, one tenth of the upper limit identified above. The conclusion is that RCSI can provide an accurate identification with this level of input measurement noise.

Figure B.10 shows the identification result during five successive cycles after applying an input measurement noise with standard deviation of 5 mA. The identified film resistance is between the true film resistance of the previous cycle and the next

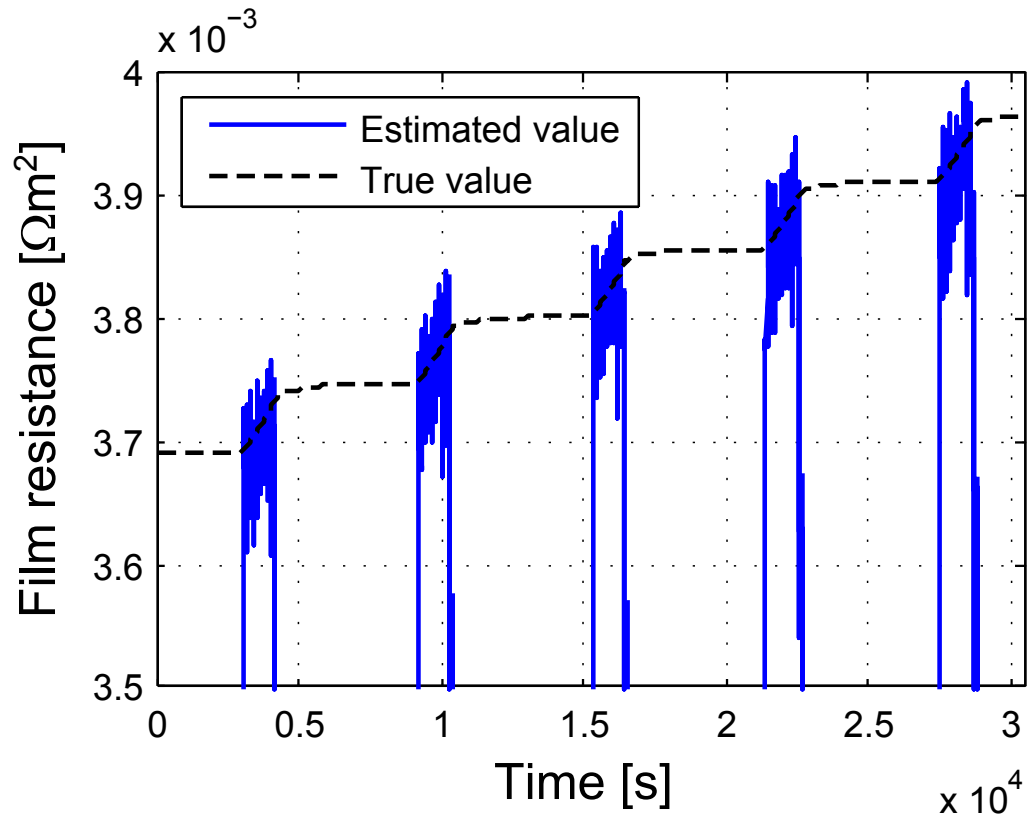


Figure B.10: A magnified view of film resistance identification with input noise when the standard deviation of the noise is 5 mA.

cycle, with a change that is less than 1.5% of the film resistance of current cycle. Hence, to estimate the film resistance within 1.5% of its true value, the standard deviation of the input measurement noise should not exceed 5 mA.

The noise level provided in this section is for capturing the film resistance difference between two successive cycles. In practice, SoH may not need to be tracked that frequently and hence noise levels larger than 5 mA or 0.1 mV may be tolerable.

B.4 Sensitivity to Uncertain Initial Conditions

The initial conditions of the main system comprise the concentration of Li-ions in the cathode, anode and separator. So far, the initial conditions of the truth system and the main system model have been assumed to be the same. This section studies how the identification results are affected if the main system model is not initialized at the same states as the true system. In the true system, the concentration in the electrolyte is chosen to be $c_e = 1.2669 \times 10^3 \text{ mol m}^{-3}$ and the concentration in anode and cathode are chosen to be $c_{s,n} = 0.8408 \text{ mol m}^{-3}$ and $c_{s,p} = 0.1592 \text{ mol m}^{-3}$, respectively. This section considers a $\pm 1\%$ error in the initialization of these states and investigates how the output error and identified film resistance change in the simulation. Specifically, a $+1\%$ initialization error means the initial states are $c_e = 1.2796 \times 10^3 \text{ mol m}^{-3}$, $c_{s,n} = 0.8492 \text{ mol m}^{-3}$ and $c_{s,p} = 0.1608 \text{ mol m}^{-3}$; whereas a -1% initialization error means the initial states are $c_e = 1.2542 \times 10^3 \text{ mol m}^{-3}$, $c_{s,n} = 0.8324 \text{ mol m}^{-3}$ and $c_{s,p} = 0.1576 \text{ mol m}^{-3}$. The value 1% is based on the 95% confidence interval of the estimation of these parameters as reported in the literature [63].

Figure B.11 shows the difference in output error during the constant current charging mode in one cycle for various initial conditions in the Main System Model. This figure shows a slight error in the output voltage when the initial conditions are perturbed by $\pm 1\%$.

Figure B.12 shows the difference in identified film resistance during constant current charging mode in one cycle with initialization errors in the Main System Model. A 1% error in the initialization causes a 7% change in the identified film resistance.

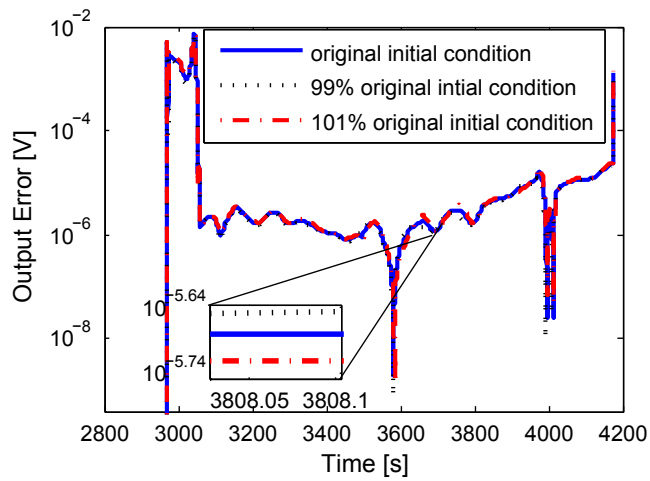


Figure B.11: The output error under various initial conditions.

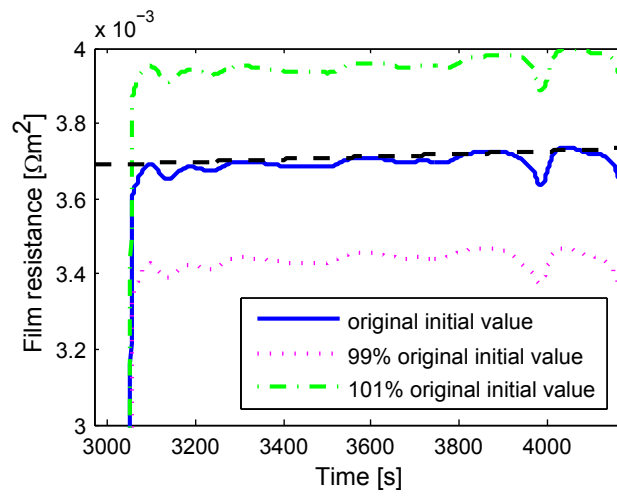


Figure B.12: The identified film resistance under various initial conditions.

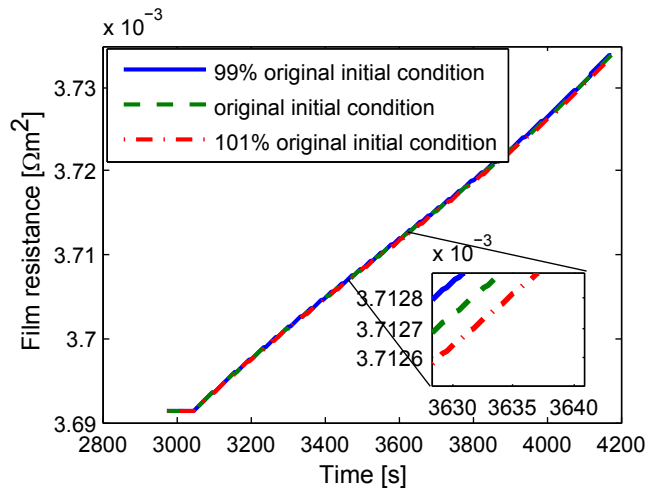


Figure B.13: The true film resistance under various initial conditions.

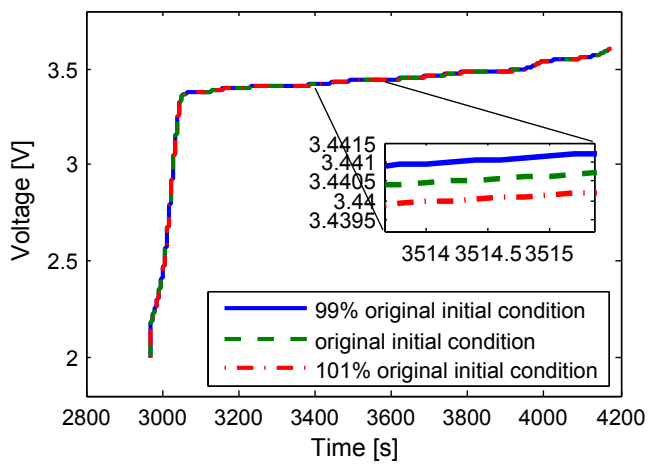


Figure B.14: The true output voltage under various initial conditions.

It is worth noting that in the truth system a $\pm 1\%$ change in the initial conditions does not cause the film resistance to change by 7%. Figure B.13 shows the difference of the film resistance in the truth system under different initial conditions. The true film resistance changes by only 0.004% for a 1% change in the initial conditions. Figure B.14 shows the difference between the output voltage in the truth system under various initial conditions. The order of magnitude of the change in output voltage is 0.1 mV. As mentioned above, the change in the identified film resistance is expected to be on the order of 10^{-2} (1%) when the change in output voltage is on the order of 0.1 mV, which corresponds with the result shown in Figure B.12. Thus, changing the initial conditions affects not only the film resistance but also the output voltage. This explains why RCSI is sensitive to the initialization errors.

B.5 Conclusions

RCSI is applied to the problem of estimating the SEI film-growth subsystem of a battery model for which the main system is the DFN model augmented with a Li consumption model. The method's performance with a first-order ARX model form is investigated. Acceptable noise levels for output voltage and input current measurements are established. RCSI can make a very accurate identification of film resistance with a measurement noise with standard deviation of 0.02 mV or 0.5 mA in the output voltage or input current, respectively. A standard deviation of 0.2 mV in the output or 5 mA in the input leads to about 1.5% error in the identified film resistance. The influence of initialization errors in the Main System Model is also studied. Results show that when the initial conditions of the truth system and the main battery system model used by RCSI differ by 1%, the identified film resistance changes by about 7%, although the true change in film resistance is 0.004%. These results will help with selecting the appropriate sensors for the experiments with the hardware.

Bibliography

- [1] S. Moura, “Doyle-Fuller-Newman electrochemical battery model.” <https://github.com/scott-moura/dfn>, 2014.
- [2] L. B. Nilson, *Teaching at its best: A research-based resource for college instructors*. John Wiley & Sons, 2016.
- [3] K. Smith and C.-Y. Wang, “Solid-state diffusion limitations on pulse operation of a lithium ion cell for hybrid electric vehicles,” *Journal of Power Sources*, vol. 161, no. 1, pp. 628 – 639, 2006.
- [4] E. Meissner and G. Richter, “Battery monitoring and electrical energy management: Precondition for future vehicle electric power systems,” *Journal of Power Sources*, vol. 116, no. 1–2, pp. 79 – 98, 2003. Selected Papers Presented at the Eighth European Lead Battery Conference.
- [5] E. Meissner and G. Richter, “The challenge to the automotive battery industry: the battery has to become an increasingly integrated component within the vehicle electric power system,” *Journal of Power Sources*, vol. 144, no. 2, pp. 438–460, 2005.
- [6] E. Karden, P. Shinn, P. Bostock, J. Cunningham, E. Schoultz, and D. Kok, “Requirements for future automotive batteries – a snapshot,” *Journal of Power Sources*, vol. 144, no. 2, pp. 505 – 512, 2005. Selected papers from the Ninth European Lead Battery ConferenceNinth European Lead Battery Conference.
- [7] S. Moura, J. Forman, S. Bashash, J. Stein, and H. Fathy, “Optimal control of film growth in lithium-ion battery packs via relay switches,” *IEEE Transactions on Industrial Electronics*, vol. 58, pp. 3555–3566, Aug 2011.
- [8] K. B. Hatzell, A. Sharma, and H. K. Fathy, “A survey of long-term health modeling, estimation, and control of lithium-ion batteries: Challenges and opportunities,” in *2012 American Control Conference (ACC)*, pp. 584–591, June 2012.
- [9] V. Pop, H. J. Bergveld, D. Danilov, P. P. Regtien, and P. H. Notten, *Battery management systems: Accurate state-of-charge indication for battery-powered applications*, vol. 9. Springer Science & Business Media, 2008.
- [10] B. Nykvist and M. Nilsson, “Rapidly falling costs of battery packs for electric vehicles,” *Nature Climate Change*, 2015.

- [11] W.-J. Zhang, "Structure and performance of lifepo₄ cathode materials: A review," *Journal of Power Sources*, vol. 196, no. 6, pp. 2962 – 2970, 2011.
- [12] J.-M. Tarascon and M. Armand, "Issues and challenges facing rechargeable lithium batteries," *Nature*, vol. 414, no. 6861, pp. 359–367, 2001.
- [13] B. Scrosati, "Recent advances in lithium ion battery materials," *Electrochimica Acta*, vol. 45, no. 15–16, pp. 2461 – 2466, 2000.
- [14] A. Ritchie and W. Howard, "Recent developments and likely advances in lithium-ion batteries," *Journal of Power Sources*, vol. 162, no. 2, pp. 809 – 812, 2006. Special issue including selected papers from the International Power Sources Symposium 2005 together with regular papers.
- [15] B. Scrosati and J. Garche, "Lithium batteries: Status, prospects and future," *Journal of Power Sources*, vol. 195, no. 9, pp. 2419 – 2430, 2010.
- [16] L. Lu, X. Han, J. Li, J. Hua, and M. Ouyang, "A review on the key issues for lithium-ion battery management in electric vehicles," *Journal of Power Sources*, vol. 226, pp. 272 – 288, 2013.
- [17] S. C. Nagpure, B. Bhushan, and S. Babu, "Multi-scale characterization studies of aged li-ion large format cells for improved performance: an overview," *Journal of The Electrochemical Society*, vol. 160, no. 11, pp. A2111–A2154, 2013.
- [18] M. Wohlfahrt-Mehrens, C. Vogler, and J. Garche, "Aging mechanisms of lithium cathode materials," *Journal of Power Sources*, vol. 127, no. 1–2, pp. 58 – 64, 2004. Eighth Ulmer Electrochemische Tage.
- [19] K. Amine, J. Liu, S. Kang, I. Belharouak, Y. Hyung, D. Vissers, and G. Henriksen, "Improved lithium manganese oxide spinel/graphite li-ion cells for high-power applications," *Journal of power sources*, vol. 129, no. 1, pp. 14–19, 2004.
- [20] P. Albertus, J. Christensen, and J. Newman, "Experiments on and modeling of positive electrodes with multiple active materials for lithium-ion batteries," *Journal of the Electrochemical Society*, vol. 156, no. 7, pp. A606–A618, 2009.
- [21] J. Wang, P. Liu, J. Hicks-Garner, E. Sherman, S. Soukiazian, M. Verbrugge, H. Tataria, J. Musser, and P. Finamore, "Cycle-life model for graphite-lifepo₄ cells," *Journal of Power Sources*, vol. 196, no. 8, pp. 3942 – 3948, 2011.
- [22] K. Amine, C. Chen, J. Liu, M. Hammond, A. Jansen, D. Dees, I. Bloom, D. Vissers, and G. Henriksen, "Factors responsible for impedance rise in high power lithium ion batteries," *Journal of Power Sources*, vol. 97–98, pp. 684 – 687, 2001. Proceedings of the 10th International Meeting on Lithium Batteries.
- [23] P. Verma, P. Maire, and P. Novák, "A review of the features and analyses of the solid electrolyte interphase in li-ion batteries," *Electrochimica Acta*, vol. 55, no. 22, pp. 6332 – 6341, 2010.

- [24] P. Arora, M. Doyle, and R. E. White, "Mathematical modeling of the lithium deposition overcharge reaction in lithium-ion batteries using carbon-based negative electrodes," *Journal of the Electrochemical Society*, vol. 146, no. 10, pp. 3543–3553, 1999.
- [25] S. Hein and A. Latz, "Influence of local lithium metal deposition in 3d microstructures on local and global behavior of lithium-ion batteries," *Electrochimica Acta*, vol. 201, pp. 354–365, 2016.
- [26] T. Tatsuma, M. Taguchi, and N. Oyama, "Inhibition effect of covalently cross-linked gel electrolytes on lithium dendrite formation," *Electrochimica Acta*, vol. 46, no. 8, pp. 1201 – 1205, 2001.
- [27] J. Vetter, P. Novak, M. Wagner, C. Veit, K.-C. Möller, J. Besenhard, M. Winter, M. Wohlfahrt-Mehrens, C. Vogler, and A. Hammouche, "Ageing mechanisms in lithium-ion batteries," *Journal of Power Sources*, vol. 147, no. 1, pp. 269–281, 2005.
- [28] P. Ramadass, B. Haran, P. M. Gomadam, and R. E. White, "Development of first principles capacity fade model for Li-ion cells," *Journal of the Electrochemical Society*, vol. 151, pp. A196–A203, February 2004.
- [29] P. Liu, J. Wang, J. Hicks-Garner, E. Sherman, S. Soukiazian, M. Verbrugge, H. Tataria, J. Musser, and P. Finamore, "Aging mechanisms of LiFePO₄ batteries deduced by electrochemical and structural analyses," *Journal of the Electrochemical Society*, vol. 157, no. 4, pp. A499–A507, 2010.
- [30] M. Safari and C. Delacourt, "Aging of a commercial graphite/LiFePO₄ cell," *Journal of The Electrochemical Society*, vol. 158, no. 10, pp. A1123–A1135, 2011.
- [31] P. Arora, R. E. White, and M. Doyle, "Capacity fade mechanisms and side reactions in lithium-ion batteries," *Journal of the Electrochemical Society*, vol. 145, no. 10, pp. 3647–3667, 1998.
- [32] G. L. Plett, "Extended Kalman filtering for battery management systems of LiPB-based HEV battery packs: Part 1. Background," *Journal of Power Sources*, vol. 134, no. 2, pp. 252–261, 2004.
- [33] G. L. Plett, "Extended Kalman filtering for battery management systems of LiPB-based HEV battery packs: Part 2. Modeling and identification," *Journal of Power Sources*, vol. 134, no. 2, pp. 262–276, 2004.
- [34] G. L. Plett, "Extended Kalman filtering for battery management systems of LiPB-based HEV battery packs: Part 3. State and parameter estimation," *Journal of Power Sources*, vol. 134, no. 2, pp. 277–292, 2004.
- [35] N. A. Samad, Y. Kim, J. B. Siegel, and A. G. Stefanopoulou, "Battery capacity fading estimation using a force-based incremental capacity analysis," *Journal of The Electrochemical Society*, vol. 163, no. 8, pp. A1584–A1594, 2016.

- [36] C. Weng, Y. Cui, J. Sun, and H. Peng, “On-board state of health monitoring of lithium-ion batteries using incremental capacity analysis with support vector regression,” *Journal of Power Sources*, vol. 235, pp. 36–44, 2013.
- [37] M. Safari, M. Morcrette, A. Teyssot, and C. Delacourt, “Life-prediction methods for lithium-ion batteries derived from a fatigue approach: I. introduction: Capacity-loss prediction based on damage accumulation,” *Journal of The Electrochemical Society*, vol. 157, no. 6, pp. A713–A720, 2010.
- [38] M. Safari, M. Morcrette, A. Teyssot, and C. Delacourt, “Life prediction methods for lithium-ion batteries derived from a fatigue approach: II. capacity-loss prediction of batteries subjected to complex current profiles,” *Journal of The Electrochemical Society*, vol. 157, no. 7, pp. A892–A898, 2010.
- [39] J. Remmlinger, M. Buchholz, T. Soczka-Guth, and K. Dietmayer, “On-board state-of-health monitoring of lithium-ion batteries using linear parameter-varying models,” *Journal of Power Sources*, vol. 239, pp. 689 – 695, 2013.
- [40] D. Andre, C. Appel, T. Soczka-Guth, and D. U. Sauer, “Advanced mathematical methods of SOC and SOH estimation for lithium-ion batteries,” *Journal of Power Sources*, vol. 224, pp. 20 – 27, 2013.
- [41] S. J. Moura, M. Krstic, and N. A. Chaturvedi, “Adaptive PDE observer for battery SOC/SOH estimation,” in *ASME 2012 5th Annual Dynamic Systems and Control Conference*, (Fort Lauderdale, FL), pp. 101–110, American Society of Mechanical Engineers, 2012.
- [42] A. M. D’Amato, J. C. Forman, T. Ersal, A. A. Ali, J. L. Stein, H. Peng, and D. S. Bernstein, “Noninvasive battery-health diagnostics using retrospective-cost identification of inaccessible subsystems,” in *ASME 2012 5th Annual Dynamic Systems and Control Conference*, pp. 299–307, American Society of Mechanical Engineers, 2012.
- [43] X. Zhou, T. Ersal, J. L. Stein, and D. S. Bernstein, “Battery health diagnostics using retrospective-cost system identification: Sensitivity to noise and initialization errors,” in *ASME 2013 6th Annual Dynamic Systems and Control Conference*, (Palo Alto, CA), p. V003T42A004 (10 pages), American Society of Mechanical Engineers, 2013.
- [44] S. Dey, B. Ayalew, and P. Pisu, “Nonlinear adaptive observer for a lithium-ion battery cell based on coupled electrochemical-thermal model,” *Journal of Dynamic Systems, Measurement, and Control*, vol. 137, no. 11, p. 111005, 2015.
- [45] T. R. Tanim and C. D. Rahn, “Aging formula for lithium ion batteries with solid electrolyte interphase layer growth,” *Journal of Power Sources*, vol. 294, pp. 239 – 247, 2015.

- [46] G. K. Prasad and C. D. Rahn, “Model based identification of aging parameters in lithium ion batteries,” *Journal of Power Sources*, vol. 232, pp. 79 – 85, 2013.
- [47] R. D. Perkins, A. V. Randall, X. Zhang, and G. L. Plett, “Controls oriented reduced order modeling of lithium deposition on overcharge,” *Journal of Power Sources*, vol. 209, pp. 318 – 325, 2012.
- [48] J. B. Siegel, X. Lin, A. G. Stefanopoulou, D. S. Hussey, D. L. Jacobson, and D. Gorsich, “Neutron imaging of lithium concentration in lfp pouch cell battery,” *Journal of the Electrochemical Society*, vol. 158, no. 5, pp. A523–A529, 2011.
- [49] A123 Systems, *Nanophosphate High Power Lithium Ion Cell ANR26650m1-B Datasheet*.
- [50] H. S. Shin, *Degradation mechanisms of electrode/electrolyte interfaces in Li-ion batteries*. PhD thesis, The University of Michigan, 2015.
- [51] M. Doyle, T. F. Fuller, and J. Newman, “Modeling of galvanostatic charge and discharge of the lithium/polymer/insertion cell,” *Journal of the Electrochemical Society*, vol. 140, no. 6, pp. 1526–1533, 1993.
- [52] T. F. Fuller, M. Doyle, and J. Newman, “Simulation and optimization of the dual lithium ion insertion cell,” *Journal of the Electrochemical Society*, vol. 141, no. 1, pp. 1–10, 1994.
- [53] N. Chaturvedi, R. Klein, J. Christensen, J. Ahmed, and A. Kojic, “Algorithms for advanced battery-management systems,” *Control Systems Magazine, IEEE*, vol. 30, pp. 49–68, June 2010.
- [54] D. Di Domenico, A. Stefanopoulou, and G. Fiengo, “Lithium-ion battery state of charge and critical surface charge estimation using an electrochemical model-based extended Kalman filter,” *Journal of Dynamic Systems, Measurement, and Control*, vol. 132, no. 6, p. 061302 (11 pages), 2010.
- [55] J. C. Forman, S. Bashash, J. L. Stein, and H. K. Fathy, “Reduction of an electrochemistry-based Li-ion battery model via quasi-linearization and Padé approximation,” *Journal of the Electrochemical Society*, vol. 158, pp. A93–A101, February 2011.
- [56] S. Santhanagopalan, Q. Guo, P. Ramadass, and R. E. White, “Review of models for predicting the cycling performance of lithium ion batteries,” *Journal of Power Sources*, vol. 156, pp. 620–628, 2006.
- [57] H. Palanthandlam-Madapusi, E. L. Renk, and D. S. Bernstein, “Data-Based Model Refinement for Linear and Hammerstein Systems Using Subspace Identification and Adaptive Disturbance Rejection,” in *Proc. Conf. Contr. Appl.*, (Toronto, Canada), pp. 1630–1635, August 2005.

- [58] A. M. D'Amato and D. S. Bernstein, "Linear Fractional Transformation Identification Using Retrospective Cost Optimization," in *Proc. SYSID*, (Saint-Malo, France), pp. 450–455, July 2009.
- [59] A. M. D'Amato, A. J. Ridley, and D. S. Bernstein, "Retrospective-cost-based adaptive model refinement for the ionosphere and thermosphere," *Statistical Analysis and Data Mining*, vol. 4, no. 4, pp. 446–458, 2011.
- [60] M. A. Santillo, A. M. D'Amato, and D. S. Bernstein, "System Identification Using a Retrospective Correction Filter for Adaptive Feedback Model Updating," in *Proc. Amer. Contr. Conf.*, (St. Louis, MO), pp. 4392–4397, June 2009.
- [61] A. V. Morozov, A. A. Ali, A. M. D'Amato, A. J. Ridley, S. L. Kukreja, and D. S. Bernstein, "Retrospective-cost-based model refinement for system emulation and subsystem identification," in *2011 50th IEEE Conference on Decision and Control and European Control Conference (CDC-ECC)*, pp. 2142–2147, IEEE, 2011.
- [62] A. Brooker and et al, "Advanced vehicle simulator." <http://adv-vehicle-sim.sourceforge.net>, 2003.
- [63] J. C. Forman, S. J. Moura, J. L. Stein, and H. K. Fathy, "Genetic identification and Fisher identifiability analysis of the Doyle-Fuller-Newman model from experimental cycling of a LiFePO₄ cell," *Journal of Power Sources*, vol. 210, pp. 263–275, July 2012.
- [64] J. C. Forman, *Minimally Invasive Characterization of Lithium Iron Phosphate Battery Electrochemical and Health Models using Fisher Information and Optimal Experimental Design*. PhD thesis, The University of Michigan, 2012.
- [65] X. Zhou, T. Ersal, J. L. Stein, and D. S. Bernstein, "Battery state of health monitoring by side reaction current density estimation via retrospective-cost subsystem identification," in *ASME 2014 7th Annual Dynamic Systems and Control Conference*, (San Antonio, TX), p. V001T19A002 (10 pages), American Society of Mechanical Engineers, 2014.
- [66] L. Cai and R. E. White, "Reduction of model order based on proper orthogonal decomposition for lithium-ion battery simulations," *Journal of The Electrochemical Society*, vol. 156, no. 3, pp. A154–A161, 2009.
- [67] T. M. Cover and J. A. Thomas, *Elements of information theory*. John Wiley & Sons, 2012.
- [68] G. C. Goodwin and R. L. Payne, "Dynamic system identification: experiment design and data analysis," 1977.
- [69] L. Zhang, C. Lyu, G. Hinds, L. Wang, W. Luo, J. Zheng, and K. Ma, "Parameter sensitivity analysis of cylindrical lifepo₄ battery performance using multi-physics modeling," *Journal of The Electrochemical Society*, vol. 161, no. 5, pp. A762–A776, 2014.

- [70] A. Alessandri, M. Cuneo, S. Pagnan, and M. Sanguineti, “A recursive algorithm for nonlinear least-squares problems,” *Computational Optimization and Applications*, vol. 38, no. 2, pp. 195–216, 2007.
- [71] S. J. Julier and J. K. Uhlmann, “A new extension of the Kalman filter to nonlinear systems,” in *Int. Symp. Aerospace/Defense Sensing, Simul. and Aontrols*, vol. 3, pp. 3–2, Orlando, FL, 1997.
- [72] J. Christensen and J. Newman, “Cyclable lithium and capacity loss in li-ion cells,” *Journal of The Electrochemical Society*, vol. 152, no. 4, pp. A818–A829, 2005.
- [73] J. Wang, J. Purewal, P. Liu, J. Hicks-Garner, S. Soukazian, E. Sherman, A. Sorenson, L. Vu, H. Tataria, and M. W. Verbrugge, “Degradation of lithium ion batteries employing graphite negatives and nickel–cobalt–manganese oxide + spinel manganese oxide positives: Part 1, aging mechanisms and life estimation,” *Journal of Power Sources*, vol. 269, pp. 937 – 948, 2014.
- [74] X. Han, M. Ouyang, L. Lu, J. Li, Y. Zheng, and Z. Li, “A comparative study of commercial lithium ion battery cycle life in electrical vehicle: Aging mechanism identification,” *Journal of Power Sources*, vol. 251, pp. 38 – 54, 2014.
- [75] D. E. Goldberg, *Genetic Algorithms in Search, Optimization and Machine Learning*. Boston, MA, USA: Addison-Wesley Longman Publishing Co., Inc., 1st ed., 1989.
- [76] “Arbin Instruments battery test equipment.” <http://www.arbin.com/index.php/products/battery#/range-of-products>.
- [77] X. Zhou, T. Ersal, J. L. Stein, and D. S. Bernstein, “Battery state of health monitoring by side reaction current density estimation via retrospective-cost subsystem identification,” 2017.
- [78] X. Zhou, T. Ersal, J. L. Stein, and D. S. Bernstein, “Battery state of health monitoring by side reaction current density estimation via retrospective-cost subsystem identification,” 2016.
- [79] X. Zhou, J. L. Stein, and T. Ersal, “Battery state of health monitoring by estimation of the number of cyclable li-ions,” in *ASME Dynamic Systems and Control Conference*, (Minneapolis, MN), American Society of Mechanical Engineers, 2016.
- [80] X. Zhou, T. Ersal, J. L. Stein, and D. S. Bernstein, “A subsystem identification technique towards battery state of health monitoring under state of charge estimation errors,” in *2015 American Control Conference*, (Chicago, IL), pp. 1812 – 1817, American Automatic Control Council, 2015.
- [81] D. H. Jeon and S. M. Baek, “Thermal modeling of cylindrical lithium ion battery during discharge cycle,” *Energy Conversion and Management*, vol. 52, no. 8–9, pp. 2973 – 2981, 2011.

- [82] Y. Kim, S. Mohan, J. B. Siegel, A. G. Stefanopoulou, and Y. Ding, "The estimation of temperature distribution in cylindrical battery cells under unknown cooling conditions," *IEEE Transactions on Control Systems Technology*, vol. 22, pp. 2277–2286, Nov 2014.
- [83] C. Forgez, D. V. Do, G. Friedrich, M. Morcrette, and C. Delacourt, "Thermal modeling of a cylindrical lifepo 4/graphite lithium-ion battery," *Journal of Power Sources*, vol. 195, no. 9, pp. 2961–2968, 2010.
- [84] T. R. Tanim, C. D. Rahn, and N. Legnedahl, "Elevated temperatures can extend the life of lithium iron phosphate cells in hybrid electric vehicles," in *ASME 2015 Dynamic Systems and Control Conference*, pp. V002T26A003–V002T26A003, American Society of Mechanical Engineers, 2015.
- [85] W. Gu and C. Wang, "Thermal-electrochemical modeling of battery systems," *Journal of The Electrochemical Society*, vol. 147, no. 8, pp. 2910–2922, 2000.
- [86] M. Guo, G. Sikha, and R. E. White, "Single-particle model for a lithium-ion cell: Thermal behavior," *Journal of The Electrochemical Society*, vol. 158, no. 2, pp. A122–A132, 2011.
- [87] L. Gireaud, S. Grugéon, S. Laruelle, B. Yrieix, and J.-M. Tarascon, "Lithium metal stripping/plating mechanisms studies: A metallurgical approach," *Electrochemistry Communications*, vol. 8, no. 10, pp. 1639 – 1649, 2006.
- [88] M. C. Smart and B. V. Ratnakumar, "Effects of electrolyte composition on lithium plating in lithium-ion cells," *Journal of The Electrochemical Society*, vol. 158, no. 4, pp. A379–A389, 2011.
- [89] J. L. Barton and J. O. Bockris, "The electrolytic growth of dendrites from ionic solutions," *Proceedings of the Royal Society of London A: Mathematical, Physical and Engineering Sciences*, vol. 268, no. 1335, pp. 485–505, 1962.
- [90] D. Aurbach, E. Zinigrad, Y. Cohen, and H. Teller, "A short review of failure mechanisms of lithium metal and lithiated graphite anodes in liquid electrolyte solutions," *Solid State Ionics*, vol. 148, no. 3–4, pp. 405 – 416, 2002. Proceedings of the Symposium on Materials for Advanced Batteries and Fuel Cells. Organised in conjunction with the International Conference on Materials for Advanced Technologies (ICMAT 2001).
- [91] I. W. Seong, C. H. Hong, B. K. Kim, and W. Y. Yoon, "The effects of current density and amount of discharge on dendrite formation in the lithium powder anode electrode," *Journal of Power Sources*, vol. 178, no. 2, pp. 769 – 773, 2008. Selected Papers Presented at the 3rd International Conference on Polymer Batteries Fuel Cells (PBFC 2007) on the occasion of Professor Bruno Scrosati's 70th birthday.

- [92] T. I. N. Laboratory, *Battery Test Manual for Electric Vehicles*. U.S. Department of Energy Vehicle Technologies Program, 3 ed., 2015.
- [93] Y. Kobayashi, T. Kobayashi, K. Shono, Y. Ohno, Y. Mita, and H. Miyashiro, “Decrease in capacity in mn-basedgraphite commercial lithium-ion batteries i. imbalance proof of electrode operation capacities by cell disassembly,” *Journal of The Electrochemical Society*, vol. 160, no. 8, pp. A1181–A1186, 2013.
- [94] R. G. Jungst, G. Nagasubramanian, C. C. Crafts, D. Ingersoll, and D. H. Doughty, “Analysis of lithium-ion battery degradation during thermal aging,” in *198th Meeting of the Electrochemical Society, Phoenix, AZ (US)*, pp. 23–27, 2000.
- [95] A. Kulka, A. Braun, T.-W. Huang, A. Wolska, M. T. Klepka, A. Szewczyk, D. Baster, W. Zajac, K. Świerczek, and J. Molenda, “Evidence for al doping in lithium sublattice of lifepo₄,” *Solid State Ionics*, vol. 270, pp. 33–38, 2015.
- [96] D. W. Dees, S. Kawauchi, D. P. Abraham, and J. Prakash, “Analysis of the galvanostatic intermittent titration technique (gitt) as applied to a lithium-ion porous electrode,” *Journal of Power Sources*, vol. 189, no. 1, pp. 263 – 268, 2009. Selected Papers presented at the 14th Internation Meeting on Lithium Batteries (IMLB-2008).
- [97] T. I. N. Laboratory, *Battery Calendar Life Estimator Manual*. U.S. Department of Energy Vehicle Technologies Program, 1 ed., 2012.